UNIVERSITY OF CALIFORNIA

Los Angeles

Magnetism in van der Waals Heterostructures: Graphene/CrSe and WTe_2/Fe_3GeTe_2

A dissertation submitted in partial satisfaction of the

requirements for the degree Doctor of Philosophy

in Electrical and Computer Engineering

by

Yingying Wu

2020

© Copyright by

Yingying Wu

2020

ABSTRACT OF THE DISSERTATION

Magnetism in van der Waals Heterostructures: Graphene/CrSe and WTe_2/Fe_3GeTe_2

by

Yingying Wu

Doctor of Philosophy in Electrical and Computer Engineering

University of California, Los Angeles, 2020

Professor Kang Lung Wang, Chair

Two-dimensional materials provide a new platform for discovery of exotic physics and phenomena. They possess rich electronic properties, susceptibility to electric control, dangling-bond-free interfaces, and readily controlled thicknesses. These properties make them accessible, engineerable, and integrable into emergent heterostructures for previously unachievable properties and applications like atomically-thin magnetoelectric devices for ultracompact spintronics. Although layered materials like graphene are not inherently spin-polarized, magnetic proximity effect-induced spin splitting has been identified as an effective way to realize spin transport in graphene. Except the magnetic proximity effect, recently discovered long-range intrinsic magnetic orders in the van der Waals materials rise fundamental research interests. This dissertation includes the experimental realization of monolayer graphene magnetized by an underlying

antiferromagnet. By coupling graphene to an antiferromagnetic thin film, exchange splitting energy as large as 134 meV at 2 K. This exchange splitting energy can be modulated through field coolings, which is reflected through the shifted quantum Hall plateau and quantum oscillations in graphene. Further, magneto-optic Kerr measurement supports magnetism in the graphene at low temperatures. This work establishes a key functionality for future graphene-based spin logic and memory devices. Different from the induced magnetism into graphene, the interface-induced Dzyaloshinskii-Moriya interaction and Néel-type skyrmion lattice in an intrinsic van der Waals ferromagnetic material Fe_3GeTe_2 have also been discussed. By coupling Fe_3GeTe_2 to 1T'-WTe_2, a large interfacial Dzyaloshinskii-Moriya interaction can be induced at the interface probably due to the inversion symmetry breaking. Transport measurements have shown the topological Hall effect in this heterostructure for temperatures below 100 K. Furthermore, Lorentz transmission electron microscopy is used to directly image Néel-type skyrmions along with aligned and stripe-like domain structures. This interfacial coupling induced Dzyaloshinskii-Moriya interaction is estimated to have a large energy of 1.0 mJ/m^2, which is much larger than the critical value required to stabilize the Néel-type skyrmions. This work paves a path towards the skyrmionic devices based on van der Waals layered heterostructure. Based on either induced or intrinsic magnetism in van der Waals materials, possible quantum anomalous Hall insulators and van der Waals heterostructure are listed and proposed.

The dissertation of Yingying Wu is approved.

Chee Wei Wong

Dwight C. Streit

Stuart Brown

Kang Lung Wang, Committee Chair

University of California, Los Angeles

2020

This dissertation is dedicated to my husband, parents and daughter, for their unconditional love, encouragement and support.

TABLE OF CONTENTS

Title Page i

Abstract ii

Table of Contents vi

List of Figures viii

List of Tables xix

Acknowledgments xx

vita xxiii

Chapter 1 Introduction to van der Waals magnetic materials 1

1.1 2D electronic systems 1

1.1.1 Induced magnetism in graphene 2

1.1.2 Transition metal dichalcogenides 6

1.2 Intrinsic 2D magnetic materials 8

1.2.1 Fe-based vdW magnets 9

1.2.2 Mn-based vdW magnets 10

1.3 2D magnetism 12

1.4 Detection of 2D magnetism 15

1.5 Magnetic heterostructure based on 2D materials 18

1.6 Sample assembly using pick-up transfer technique 19

1.7 Outline 22

Chapter 2 Magnetism in graphene coupled to an antiferromagnet 23

2.1 Crystal and magnetic structure of CrSe film 24

2.1.1 Crystal structure from TEM and XRD 25

2.1.2 Spin texture from neutron diffraction 26

2.1.3 Transport properties of CrSe film 27

2.2 Magnetized graphene from transport and MOKE measurements 29
2.2.1 Field cooling dependence of graphene/CrSe heterostructure 30
2.2.2 Super-paramagnetism from MOKE measurements 36
2.3 Landau level fitting using machine learning 40
2.3.1 Landau level considering the spin-splitting term 41
2.3.2 Slope of the Landau fan diagram 43
2.3.3 Extraction of spin-splitting energy using the machine learning 44
2.3.4 Discussion of the fitting results 50
2.4 Summary of Chapter 2 53

Chapter 3 Néel-type skyrmions in WTe_2/Fe_3GeTe_2 heterostructures 54
3.1 Transport properties of FGT 54
3.2 Transport properties of WTe_2 films 59
3.3 Topological Hall effect in WTe_2/FGT heterostructure 60
3.4 Néel-type skyrmions under Lorentz transmission electron microscopy 68
3.4.1 Principles of Lorentz electron transmission microscopy 68
3.4.2 Enhanced DMI in FGT with WTe_2 71
3.4.3 Néel-type nature of the skyrmions 78
3.4.4 Stability of the existence of skyrmions 82
3.4.5 Interface coupling in heterostructure with varied FGT thicknesses 85
3.5 Micromagnetic simulation: a finite penetration depth 85
3.6 Comparison of skyrmion size between transport and Lorentz transmission electron microscopy measurements 88

Chapter 4 Summary and Outlook 92
4.1 Conclusion 92
4.2 Future work 94
4.2.1 New intrinsic quantum anomalous Hall insulators 95
4.2.2 Van der Waals heterostructure 97

References 99

LIST OF FIGURES

1.1 Material library for layered vdW nonmagnetic materials, including graphene, black phosphorus, transition metal dichalcogenides, and III-VI family. 3

1.2 Haldane model for quantum Hall effect without Landau levels in graphene. Two inequivalent sites A, B belonging to the same unit cell are labelled. Dashed lines indicate the next nearest neighbor hopping and solid lines with arrows indicate the next nearest neighbor hopping direction. 4

1.3 The crystal structure of WTe_2 with a unit cell. The graph was drawn with a software called CrystalMaker. Left graph shows the front 3D view and the right graph shows the front 2D view with lattice parameters $a = 3.49\mathring{A}$, $b = 6.27\mathring{A}$ and $c = 14.04\mathring{A}$. 7

1.4 The crystal structure of FGT with a unit cell. The graph is drawn with a software called CrystalMaker. The left and right graph show the front 3D and 2D views. The lattice parameters are: $a = 3.99\mathring{A}$ and $c = 16.34\mathring{A}$. 9

1.5 The schematic two septuple layers of $Mn_1Bi_2Te_4$ with the antiferromagnetic coupling between layers. The yellow, green and purple spheres are for Te, Bi and Mn atoms, respectively. The red arrows indicate the spin polarization directions for Mn atoms. 11

1.6 Thermal fluctuation effects on the spin dimensionality. **a**, Ising model with spin aligning in a line. Spin dimension of one. **b**, XY model with spin residing in a plane. Spin dimension of two. **c**, Heisenberg model with spin in all directions. Spin dimension of three. 14

1.7 Schematic illustration of the sample assembly. There are two sample planes under the microscope. One is on slide glass and the other one is on the substrate as indicated. The heater is used to apply heat with DC current during pick-up and transfer procedure. 20

1.8 Homemade sample assembly facility using pick-up transfer technique. The top white part is the microscope with objective lens. The left white part is the heater. Slide gas is attached to a XY aligner and sample on the substrate is attached to the heater which is on a XY stage. 21

1.9 Black phosphorus/graphene heterostructure assembly using pick-up transfer technique. PDMS/PPC is used to pick up black phosphorus exfoliated onto the SiO_2/Si substrate first. After pick-up, PDMS/PPC/black phosphorus is used to pick up graphene. After transferring PDMS/PPC/black phosphorus/graphene onto any desired substrate and dipping in acetone, heterostructures can be formed. 21

2.1 NiAs-phase CrSe with alternating layers of Cr and Se atoms and labelled axis for the unit cell. The lattice parameters for the unit cell are: $a_1 = a_2 = 3.60\,\mathring{A}$ and $a_3 = 5.81\,\mathring{A}$. 25

2.2 Transmission electron microscopy for side view of CrSe/GaAs heterostructure indicates the good quality of CrSe. 26

2.3 X-ray diffraction shows that CrSe has a NiAs-type crystal structure. 26

2.4 Neutron diffractions of $(200)_{\text{Mag}}$ and $(201)_{\text{Mag}}$ Bragg peaks indicate the Néel temperature for our AFM thin films is close to the reported values in bulk. The dots are the measured data and the lines are the fitting curves. Error bars represent a single standard deviation. The inset shows the reflection high-energy electron diffraction during molecular beam epitaxy growth of CrSe on GaAs. 28

2.5 Temperature dependent resistivity of 30 nm-thick and 60 nm-thick CrSe films. 60 nm-thick CrSe is metallic while 30 nm-thick CrSe is semiconducting. 28

2.6 Raman spectroscopy of monolayer graphene indicates the monolayer graphene with a high 2D peak and a low level of disorder with a negligible D peak. The inset shows the microscopic image of graphene/CrSe before (top graph) and after (bottom graph) doing photolithography. The nearby thick flake on the left side of the graph serves as a locator when doing photolithography. 30

2.7 Magnetoresistivity in the blue curve and Hall resistivity in the red curve for graphene on 30 nm-thick CrSe with no external magnetic field when cooling down. Quantum oscillations of longitudinal resistivity and dips of Hall resistivity were observed. 31

2.8 Schematic graph for graphene/CrSe under field coolings. The black arrow indicates the applied magnetic field direction. The hexagonal lattice is graphene. The green and purple cuboids are CrSe and GaAs layers, respectively. 32

2.9 Magnetoresistivity of monolayer graphene/CrSe sample under different field coolings. The same dip as denoted by the dashed are shifted by the field coolings, where the positive field cooling shifts the quantum oscillations rightwards and negative one shifts the oscillations leftwards. 33

2.10 Hall resistivity of monolayer graphene/CrSe sample under different field coolings. The quantum Hall plateau is shifted with respect to the field cooling. 34

2.11 Hall resistivity and magnetoresistivity of 30 nm-thick CrSe/GaAs at 2K show little dependence on field coolings. This helps exclude the possibility that the shift of the quantum oscillations in the heterostructure is from CrSe. 34

2.12 For the quantum oscillations dip indicated by the arrow in Fig. 2.9 and quantum Hall plateau indicated by the dashed arrow in Fig. 2.10, which have the same Laudau level index, the red filled circles are for the magnetic fields at the middle of the quantum Hall plateaus and the blue squares are for the magnetic fields at the dips of the quantum oscillations. 35

2.13 Magnetic phase transition revealed by the kink around 265K (which is 8K lower than the Néel temperature) both at 2T FC cool down followed by the 0T warm up. 36

2.14 The experimental set-up for the magneto-optic Kerr effect measurement. The system begins with a He-Ne CW laser centered at 633 nm. The laser beam is then intensity-modulated at $\sim$ 100 KHz using a photo-elastic modulator and polarized linearly. 38

2.15 MOKE measurements of the graphene-on-CrSe sample and a control sample. The Kerr rotation of graphene-on-CrSe shows the magnetized graphene at 12 K and no magnetic signal at room temperature. The graph below shows the Kerr signal for CrSe on the same substrate. The arrows indicate the magnetic field sweeping direction. 39

2.16 Comparison between MOKE data at 12 K and transport data at 2 K for graphene/CrSe heterostructure. It shows a good consistency between MOKE and transport data. 40

2.17 The schematic view for graphene coupled to antiferromagnetic CrSe thin films. The red and blue lines represent the linear dispersion near the Dirac points corresponding to the up and down electron spins, respectively. The negative (- B_{FC}) and positive (+ B_{FC}) field coolings decrease and increase the exchange splitting energy Δ, respectively. The blue arrows in the lower panels represent the remanence magnetization induced at the interface. 45

2.18 The dependence of longitudinal resistivity on the inverse of magnetic fields shows the equally spaced periods of the oscillations under different field coolings. Quantum oscillations are shifted by the field cooling. 46

2.19 The slope of the Landau fan diagram dependence on the field coolings from the experiment and fitting using machine learning. It shows a perfect match between the experimental and model values. 47

2.20 The stability check for the learning algorithm. Either one of the four parameters converges into a constant when the steps are large enough. 48

2.21 The spin splitting energy dependence on the field coolings from experiment and fitting using machine learning. It shows a perfect match between experimental and model values. 49

2.22 Landau level indices extracted in the Landau fan diagram for different field coolings, where the dots are the experimental values and the lines are from calculations using parameters given by machine learning. 50

2.23 Assigning the Landau-level indices by letting $n \rightarrow n-1$ (a) and $n \rightarrow n+1$ (b). The expected fan diagrams are shown by the lines in both panels. These two fittings do not match the data. 51

2.24 Same activation energy for 30 nm-thick CrSe extracted from R-T curves. Solid lines are experimental values and dashed lines are the linear fitting curves. Inset shows the zoom-in fitting at high temperature region. 51

3.1 Schematic side view of the atomic lattice of monolayer FGT with a scale bar of 2 Å. Pink, blue and yellow atoms are for Te, Fe, and Ge atoms, respectively. 55

3.2 Atomic force microscopy for determining the thickness. **a**, Microscopic image of exfoliated Fe_3GeTe_2 thin films. Scale bar: 10 μm. **b**, Cross-sectional profile of the Fe_3GeTe_2 flakes along the black line shown in **a**. 56

3.3 Temperature dependence of Hall resistivity for **a**, 60L and **b**, 30L Fe_3GeTe_2 flakes showing that the Curie temperature is $\sim$ 200 K for Fe_3GeTe_2 thick layers. Insets show the devices for the measurements separately and the scale bar in the inset: 10 μm. Resistivity is shifted for clarity. The vertical scale bars are 10 Ω. 57

3.4 Temperature dependence of Hall resistivity for **a**, 7L and **b**, 4L Fe_3GeTe_2 flakes showing that the Curie temperature decreases when Fe_3GeTe_2 becomes thinner. Insets show the devices for the measurements and the scale bar in the inset: 10 μm. Resistivity is shifted for clarity. The vertical scale bars are 10 Ω for **a** and 100 Ω for **b**. 58

3.5 Schematic side view of the atomic lattice of WTe_2 with a scale bar of 2 Å. The pink and green atoms are for Te and W atoms, respectively. 60

3.6 Hall resistivity of a monolayer WTe_2 on bottom electrodes at 2 K close to a linear relation, which helps exclude the possibility that the dips and peaks in the Hall resistivity of WTe_2/FGT are from WTe_2 film. 60

3.7 Temperature dependence of longitudinal resistivity of monolayer WTe_2 shows an insulating behavior. Thus in the WTe_2/FGT heterostructure, the current mainly goes through FGT since FGT is more electrically conductive. 61

3.8 Magnetic texture of skyrmions[89]. **a**, Néel-type and **b** Bloch-type skyrmions with magnetization rotating from the down direction at the center to the up direction of the edge. 62

3.9 Schematic graph for monolayer WTe_2 on monolayer FGT. The van der Waals gap between this two materials is set as $\sim$3 $\mathring{A}$. This graph is drawn with a software called CrystalMaker. 63

3.10 Transport properties of sample A. **a**, Microscopic image of sample A with 1L WTe_2/4L Fe_3GeTe_2 transferred onto the bottom electrodes. **b**, Longitudinal resistivity dependence on the temperature shows an increasing resistivity with decreasing temperature. 64

3.11 Longitudinal resistivity dependence on the temperature for sample B shows a metallic behavior. The resistivity is close to that of FGT as the resistivity of monolayer WTe_2 is two orders of magnitude larger. The inset shows the device configuration of h-BN/WTe_2/FGT on the bottom electrodes. 65

3.12 Longitudinal resistivity dependence on the temperature for 3L FGT with WTe_2 shows an increasing resistivity with decreasing temperature. 65

3.13 Topological Hall effect in sample A. The magnetic field is applied in an out-of-plane direction. The dips and peaks appear near the magnetic phase transition at temperatures lower than 100 K, which signify the presence of THE. 66

3.14 Step-like magnetic transitions in sample B at temperatures from 180 K to 200 K, which is related to the formation of multi domains. The magnetic field is applied in an out-of-plane direction. 67

3.15 Schematic diagram of a Néel-type skyrmion on a tilt sample for Lorentz transmission electron microscopy imaging. The red and blue circles are for positive and negative magnetizations along z direction, respectively. Brown arrows indicate the in-plane magnetization component while grey arrows indicate the Lorentz force. 70

3.16 Schematic of ray diagrams indicating the paths of electrons passing through a magnetic specimen under the Fresnel or defocus mode of Lorentz transmission electron microscopy[95] for **a** in-focus, **b**, over-focus and **c** under-focus cases. 71

3.17 Sample for comparing the domain difference in 30L FGT with and without bilayer WTe_2. The white dashed line region is for FGT with WTe_2 while other regions inside the black dashed line is for FGT only. 72

3.18 Typical labyrinth domain in 30L FGT thin flakes in region as shown in Fig. 3.17 at a 0T magnetic field. This sample has the same FGT thickness as that of sample B (h-BN/2L WTe_2/30L FGT) for studying transport properties. 73

3.19 Much smaller domain width observed in WTe_2/30L FGT heterostructure. The contrast changing with the tilt angle α and disappearing when $\alpha = 0°$, which indicates the Néel-type nature of the magnetic domains. From the aligned and stripe-like domain structures of the WTe_2/FGT, a Dzyaloshinskii-Moriya interaction energy is estimated to be ~ 1.0 mJ/m^2. 73

3.20 Representative image used to obtain the averaged domain width of 2L WTe_2/30L FGT sample. Four line cuts are taken and the magnetic strip domain width is taken as the averaged value, determined to be 290$\pm$10 nm. 74

3.21 Hall resistivity shifted for clarity of 2L WTe_2/30 L FGT heterostructure at 5 K and 94 K. The magnetization ratio is estimated from the ratio of the anomalous Hall resistivity value. 76

3.22 L-TEM images of magnetic domains for 35L FGT with and without 8L WTe_2 at 195 K with a tilting angle 30° and a varied field. The dashed pink line region is the Fe_3GeTe_2 with WTe_2. With magnetic fields in z-direction (as defined in Fig. 3.15) are -450 Oe, 0 Oe and 480 Oe, magnetic domain widths are smaller in WTe_2/FGT region compared to that in FGT region. Magnetic skyrmions appear at a magnetic field of 660 Oe. We have zoomed in and indicated the skyrmions with purple dashed circles. 77

3.23 Magnetic domain difference for 35L Fe_3GeTe_2 with and without 8L WTe_2 at 195 K with a tilting angle 30° and the detailed field dependence between 480 Oe and 630 Oe. FGT region enters into the single uniform magnetic domain when the magnetic field is large enough ($\sim$ 660 Oe), while FGT with WTe_2 shows emerging skyrmions. 79

3.24 Defocus images of skyrmion lattice for WTe_2/40L FGT sample at a field of 510 Oe at 180 K. When the focus is changed from de-focus (-2.00 mm, -1.50 mm, -1.01 mm) to over-focus (1.02 mm, 1.50 mm, 2.00 mm, 2.50 mm), the skyrmion contrasts change from dark in the bottom and bright on the top to bright in the bottom and dark on the top. 80

3.25 The dependence of the skyrmion contrast on the magnetic field at 197 K with a tilt angle of 30° for WTe_2/40L FGT sample. The skyrmions appear at -600 Oe and 630 Oe. The contrast is adjusted for clarity. 80

3.26 Lorentz transmission electron microscopy observation of a Néel-type skyrmion at T=94 K, α=21.86° and H=540 Oe, 600 Oe, where α is the angle between the sample plane and xy plane. The yellow arrow points to a skyrmion. The skyrmion size is estimated to be $\sim$150 nm. 81

3.27 Line profile for the image of skyrmions observed in 2L WTe_2/30L FGT samples. The skyrmion size is determined from the point intensity along blue lines as shown in the insets. It is estimated to be $\sim$150 nm at 94 K with magnetic fields of 540 Oe and 600 Oe shown in the upper panel and $\sim$80 nm at 198 K with a magnetic field of 390 Oe shown in the bottom panel. 82

3.28 Skyrmion image dependence on the tilt angle at 180 K with a field of 510 Oe for WTe_2/40L FGT sample. When the tilt angle is close to 0° ($\alpha = 2.5°$ and $0°$), the magnetic skyrmions disappear, which is consistent with its Néel-type nature. The contrast becomes most pronounced at $\alpha = 30°$. 83

3.29 Skyrmions at different sample positions for the 2L WTe_2/40L FGT sample when the magnetic field is cycled through ,at 195 K with an angle of 30° and at the field of 780 Oe. The skyrmions show up at random instead of fixed positions. 83

3.30 Skyrmions contrast measured at the same sample position for 9 times within totally 2 minutes at 195 K with a field of 780 Oe for WTe_2/40L FGT. The dashed circles mark two skyrmions with their relative positions changing through time. Contrast was adjusted by post processing. By comparing the distance between two nearby skyrmions as indicated by the purple and pink circles, a very small variation between the position of these two skyrmions are obtained. 84

3.31 Difference of magnetic domains for the FGT and WTe_2/FGT samples. **a**, For 35L FGT, the region with WTe_2 shows narrower domain width. **b**, For 65L FGT, there is no difference of the magnetic domains. The region with dashed lines is for the FGT with WTe_2. 86

3.32 3D view of the simulation of the skyrmions in WTe_2/FGT. **a**, DMI exists at the interface between the WTe_2 and FGT and decays when away from the interface. **b**, Spin polarization at the interface of WTe_2 and FGT. **c**, Spin polarizations for the side of FGT close to SiN substrate. **d**, Spin polarization at yz plane with a fixed x=10. 88

3.33 Topological Hall effect for 1L WTe_2/3L FGT, 1L WTe_2/4L FGT and 2L WTe_2/5L FGT samples. The dips and peaks near the magnetic phase transition have been observed for FGT thickness ranging from 3L to 5L. 90

3.34 Extracted skyrmion size from transport and Lorentz transmission electron microscopy as a dependence on FGT thickness at 100 K and 195 K. The points in a circular shape are the skyrmion sizes from topological Hall effect and in a square shape are those from Lorentz transmission electron microscopy. Points in magenta color are taken at 100 K and points in blue color are taken at 195 K. 91

4.1 Transport properties of thick $Mn_1Bi_4Te_7$ close to bulk. **a**, Side view of crystal structure. **b**, Temperature dependence of longitudinal resistance indicating a magnetic phase transition around 10 K. Magnetoresistance **c** and Hall resistance **d** at temperatures of 2 K, 5 K, 10 K and 20 K. 96

4.2 Transport properties of thick $Mn_1Bi_8Te_{13}$ close to bulk. **a**, Side view of crystal structure. **b**, Temperature dependence of longitudinal resistance indicating a magnetic phase transition around 10 K. **c**, Magnetoresistance at 10 K and Hall resistance at temperatures of 2 K, 5 K, 12 K 14 K, 15 K and 20 K. 97

LIST OF TABLES

1.1 Representative van der Waals magnets, including ferromagnets and antiferromagnets. 8

4.1 Possible van der Waals quantum anomalous Hall insulators, including $Mn_1Bi_{2+2n}Te_{4+3n}$ family and LaCl. 95

ACKNOWLEDGMENTS

It has been a great journey since I joined the DRL lab. During these four years, I have received numerous help from many people here. Most importantly, I would like to express my sincere gratitude and respect to Prof. Kang L. Wang for the continuous support and guidance through my Ph.D. study. I have learnt a lot about how to be a good researcher and an excellent advisor from him. He led me into the world of topological quantum material, guided me to overcome the various difficulties in my projects, challenged me for the new ideas, showed me how to maintain successful active cooperations, and taught me how to organize the lab. Apart from the help in the academic part, Prof. and Mrs. Wang are my friends in daily life. They are willing to hear my stories and share their experience.

I would also like to acknowledge Prof. Stuart Brown, Prof. Dwight C. Streit and Prof. Chee Wei Wong for serving as my doctoral committee members and giving me insightful guidance during my Ph.D. study.

Besides, I am deeply grateful to my outstanding collaborators for their indispensable support and contribution to my research work. In particular, I want to express my gratitude to Dr. Alexander Grutter from National Institute of Standards and Technology, Dr. Senfu Zhang, Dr. Junwei Zhang and Prof. Xixiang Zhang from King Abdullah University of Science and Technology for their excellent work on Lorentz transmission electron microscopy, Dr. Wei Wang from Nanjing Tech University for his growth of the bulk materials, Dr. Yang Lin Zhu, Dr. Jin Hu, and Prof. Zhiqiang Mao from Pennsylvania State University for their growth of van der Waals crystals, Dr.

Chi Fang, Prof. Caihua Wan, and Prof. Xiufeng Han from Chinese Academy of Sciences for their help with the e-beam lithography, and Dr. Ang Li and Prof. Xiaodong Han from Beijing University of Technology for carrying out transmission electron microscopy measurements. I would also like to thank Prof. Ni Ni from UCLA, Jiadong Zang from University of New Hampshire, Dr. Eun Sang Choi from National High Magnetic Lab and Prof. Ning Wang from the Hong Kong University of Science and Technology for their helpful discussions or technical support.

Moreover, It is a wonderful opportunity for me to work with talented students and postdocs in DRL at UCLA. In particular, I want to thank Dr. Gen Yin for the collaborative work on the large exchange splitting in graphene/antiferromagnet heterostructure. I want to thank Dr. Lei Pan for growing the CrSe thin films. I want to thank Quanjun Pan for carrying out the optical measurements. I want to thank Dr. Kin Wong for material characterizations. I also want to thank Dr. Shin Hung Tsai and Ms. Gaili Wang for help in fabricating the devices. I would like to acknowledge Dr. Chao-Yao Yang, Dr. Qiming Shao and Dr. Yabin Fan for helpful discussions. Furthermore, I would like to thank Mr. Peng Zhang, Dr. Peng Deng, Dr. Hao Wu, Dr. Xiaoyu Che, Mr. Yuxiang Liu, Dr. Guoqiang Yu, Dr. Chiristopher Eckberg, Dr. Qinging He, Dr. Xufeng Kou, Dr. Tianxiao Nie, Dr. Hussamaldeen Saif Qasem, Dr. Sukong Chong, Dr. Gang Qiu and Mr. Lixuan Tai for their help in theory and in experiment.

I also gratefully acknowledge sources of financial support for this work. Studies in Chapter 2 & 3 are supported by ARO program under contract W911NF-15-1-10561, and Spins and Heat in Nanoscale Electronic Systems (SHINES), an Energy Frontier Research Center funded by the US Department of Energy (DOE), Office of Science, Basic Energy Sciences (BES) under award

#SC0012670. The studies in Chapter 2 are also supported by National Science Foundation (DMR-1411085 and DMR-1810163). Studies in Chapter 3 are partially supported by US Department of Energy under grand DE-SC0019068, National Science Foundation with award Nos. 1935362, 1909416 and DMR-1411085.

Last but not least, I thank my parents and especially my husband Baoyi Chen, for their unconditional support and encouragement. My husband and I started our own family during our PhD years. Our newborn girl came at the end of July, 2020. These four years witness a lot of significant steps forward of us.

VITA

Education

2016-2020	*Graduate Student Researcher* in **Electrical and Computer Engineering**
	University of California, Los Angeles, USA
2014-2016	*MPhil* in **Physics**
	The Hong Kong University of Science and Technology, China
2010-2014	*B.S.* in **Physics**, Kuang Yaming Honors School
	Nanjing University, Jiangsu, China

Selected Publications

[1] **Y. Wu**, G. Yin, L. Pan, A. J. Grutter, Q. Pan, A. Lee, D. A. Gilbert, J. A. Borchers, W. Ratcliff II, A. Li, X. Han, and K. L. Wang. Large Exchange Splitting in Monolayer Graphene Magnetized by an Antiferromagnet. ***Nature Electronics***: 1-8, 2020.

[2] **Y. Wu**, S. Zhang, J. Zhang, W. Wang, Y. L. Zhu, J. Hu, G. Yin, K. Wong, C. Fang, C. Wan, X. Han, Q. Shao, T. Taniguchi, K. Watanabe, J. Zang, Z. Mao, X. Zhang, and K. L. Wang. Néel-type Skyrmion in WTe_2/Fe_3GeTe_2 van der Waals heterostructure, ***Nature Communications***, **11**, 3860, 2020.

[3] K. L. Wang, **Y. Wu**, C. Eckberg, G. Yin, and Q. Pan. Topological Quantum Materials, ***MRS Bulletin***, 45(5), 373-379, 2020.

[4] C. Yang, L. Pan, L. Pan, A. J. Grutter, H. Wang, X. Che, Q. L. He, **Y. Wu**, D. A. Gilbert, P. Shafer, E. Arenholz, H. Wu, G. Yin, P. Deng, J. A. Borchers, W. Ratcliff II, and K. L. Wang. Termination Switching of Antiferromagnetic Proximity Effect in Topological Insulator, ***Science Advances*** 6.33: eaaz8463, 2020.

[5] L. Pan, A. Grutter, P. Zhang, X. Che, T. Nozaki, A. Stern, M. Street, B. Zhang, B. Casas, Q. L. He, E. S. Choi, S. M. Disseler, D. A. Gilbert, G. Yin, Q. Shao, P. Deng, **Y. Wu**, X. Liu, X. Kou, S. Masashi, X. Han, C. Binek, S. Chambers, J. Xia, and Kang L. Wang. Observation of Quantum Anomalous Hall Effect and Exchange Interaction in Topological Insulator/Antiferromagnet Heterostructure, ***Advanced Materials***, 32(34), 2001460, 2020.

[6] **Y. Wu**, J. J. He, T. Han, S. Xu, Z. Wu, J. Lin, T. Zhang, Y. He, and N. Wang. Induced Ising Spin-orbit Interaction in Metallic Thin Films on Monolayer WSe_2, ***Physical Review B***, **99**, 121406, 2019.

[7] Q. L. He, G. Yin, A. J. Grutter, L. Pan, X. Che, G. Yu, D. A. Gilbert, S. M. Disseler, Y. Liu, P. Shafer, B. Zhang, **Y. Wu**, B. J. Kirby, E. Arenholz, R. K. Lake, X. Han and Kang L. Wang. Exchange-biasing Topological Charges by Antiferromagnetism. ***Nature Communications***, **9**, 2767, 2018.

[8] T. Han, J. Shen, F. Yuan, J. Lin, Z. Wu, **Y. Wu**, S. Xu, L. An, G. Long, Y. Wang. R. Lortz, and N. Wang. Investigation of the Two-gap Superconductivity in a Few-Layer $NbSe_2$-graphene heterojunction, ***Physical Review B***, v. 97, (6), 2018.

[9] S. Xu, J. Shen, G. Long, Z. Wu, Z. Bao, C. Liu, X. Xiao, T. Han, J. Lin, **Y. Wu**, H. Lu, J. Hou, L. An, Y. Wang, Y. Cai, K. M. Ho, Y. He, R. Lortz, F. Zhang, and N. Wang, Odd-Integer Quantum Hall States and Giant Spin Susceptibility in p-Type Few-Layer WSe_2, ***Physical Review Letters***, 118, 067702, 2017.

[10] **Y. Wu**, X. Chen, Z. Wu, S. Xu, T. Han, J. Lin, B. Skinner, Y. Cai, Y. He, C. Cheng, and N. Wang. Negative compressibility in graphene-terminated black phosphorus heterostructures. ***Physical Review B***, **93**(5): 035455, 2016.

[11] Z. Wu, S. Xu, H. Lu, A. Khamoshi, G. Liu, T. Han, **Y. Wu**, J. Lin, G. Long, Y. He, Y. Cai, Y. Yao, F. Zhang, and N. Wang. Even-odd Layer-dependent Magnetotransport of High-mobility Q-valley Electrons in Transition Metal Disulfides, ***Nature Communications*** **7**, 12955, 2016

[12] X. Chen, L. Wang, **Y. Wu**, H. Gao, Y. Wu, G. Qin, Z. Wu, Y. Han, S. Xu, T. Han, W. Ye, J. Lin, G. Long, Y. He, Y. Cai, W. Ren and N. Wang. Probing the Electronic States and Impurity Effects in Black Phosphorus Vertical Heterostructures. ***2D Materials***, 3(1): 015012, 2016.

[13] Z. Wu, S. Xu, H. Lu, A. Khamoshi, G. Liu, T. Han, **Y. Wu**, J. Lin, G. Long, Y. He, Y. Cai, Y. Yao, F. Zhang, and N. Wang. Observation of Valley Zeeman and Quantum Hall Effects at Q valley of Few-layer Transition Metal Disulfides. ***Nature Communications*** **7**(1), 1-8, 2016.

[14] X. Chen[†], **Y. Wu**[†], Z. Wu, Y. Han, S. Xu, L. Wang, W. Ye, T. Han, Y. He, Y. Cai and Ning Wang. High-quality Sandwiched Black Phosphorus Heterostructure and its Quantum Oscillations. ***Nature Communications***, **6**, 2015. ([†]: equal first authors)

Chapter 1

Introduction to van der Waals magnetic materials

Two dimensional (2D) materials have attracted extensive attention due to their huge potential for applications in electronic and optoelectronic devices. Numerous studies have been carried out on conventional van der Waals materials like graphene[1, 2, 3], black phosphorus[4, 5], hexagonal boron nitride (h-BN)[6], transition metal dichalcogenides (TMDs)[7] and other materials since the discovery of the mechanical exfoliation with scotch tape. In this part, starting from conventional van der Waals materials discovered ten more years ago, the recently recognized van der Waals magnetic materials, including their heterostructures, are discussed.

1.1 2D electronic systems

Layered materials are characterized by a planar structure held together with the strong in-plane covalent bonds and vertical stacking by the weak van der Waals (vdW) force. They have been expanded over the years and now are a large family as listed in Fig. 1.1, enabling the discovery of new physics and phenomena. The first material discovered using the mechanical exfoliation was graphene, a semimetal with no band overlap. Later, the 2D family included the semiconductors like some TMDs, metals like superconducting $NbSe_2$, and insulators like h-BN. Most few layers of these materials (with a thickness of several nanometers) are unstable under the air conditions

with water and oxygen, and usually h-BN is served as a protection layer to isolate the materials from the ambient conditions.

Interestingly, the properties of such 2D materials are always sharply different from those in the bulk case. For example, graphene is a zero gap semiconductor while graphite is a semimetal with a band overlap and monolayer TMDs have direct band gaps while their few-layer or bulk forms have indirect ones. Moreover, much more unknowns raise when it comes to the combination of these layered materials into a heterostructure. Such heterostructure is held together by a vdW force, the same force that holds the materials stacking vertically. It not only allows a great number of combinations which have a much more sharper interface than that from any traditional growth method, but also enables the new physics arising from the stacking parameters like the relative orientation which can be controlled and altered. Taking advantage of the proximity effect in these heterostructures, the neighboring thin films can have charge redistribution in the first-order approximation. They can also induce structural changes in each other and these alternations can be controlled by adjusting the relative orientation between the individual layers.

1.1.1 Induced magnetism in graphene

Unique features of graphene electronic properties arise from its gapless, massless and chiral Dirac spectrum. Combined with the exceptionally high carrier mobilities, graphene is one of the most alluring and widely studied 2D materials. Quantum Hall effect at low temperature[3] and even at room temperature[1] was soon observed in graphene after obtaining it from mechanical exfoliation.

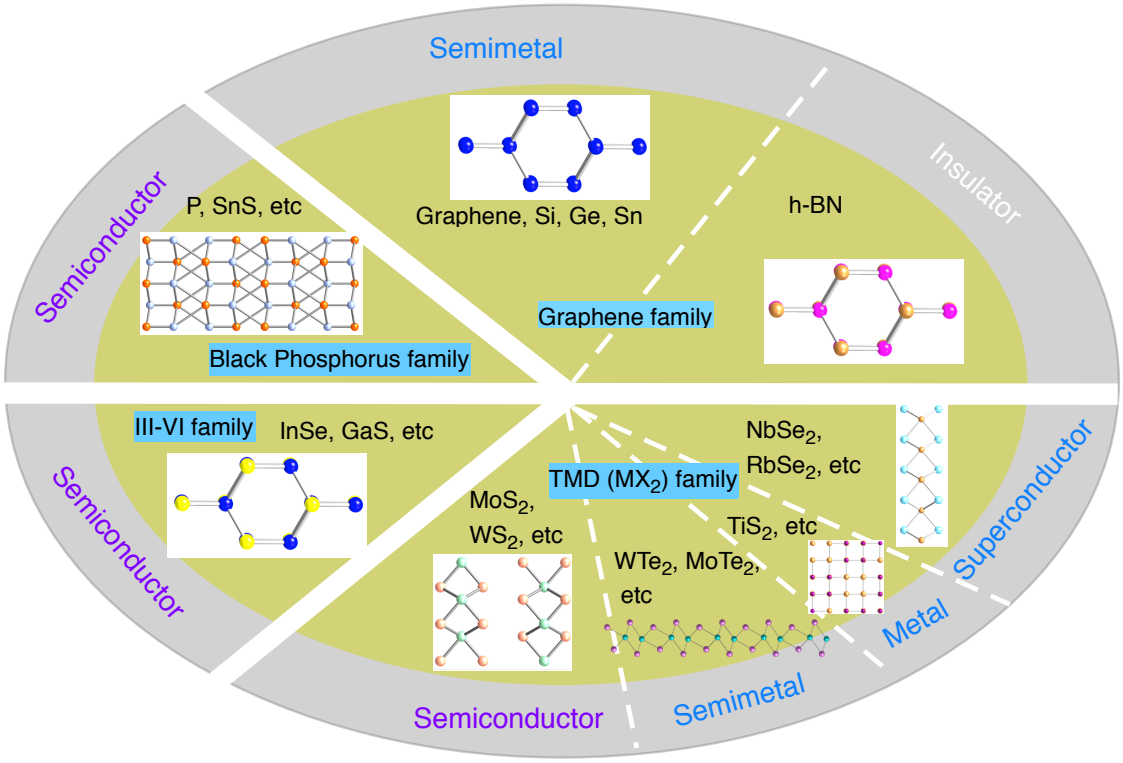


Figure 1.1. Material library for layered vdW nonmagnetic materials, including graphene, black phosphorus, transition metal dichalcogenides, and III-VI family.

Even before the advent of monolayer graphene, Haldane has proposed the quantum Hall effect without Landau levels which is quantum anomalous Hall effect in '2D graphite'. Applying a toy model with nearest and next nearest neighbor hopping in graphene as shown in Fig.1.2, closed paths of next nearest neighbor hopping enclose nonzero magnetic flux. As a result, particles taken through this trajectory will accumulate a nonzero phase, which is emblematic of a nonzero Berry curvature in this system. Thus a gapped state, hosting a zero-field quantized Hall conductivity, was proposed by Haldane[8]. However, this has not been experimentally proved in monolayer graphene so far. Instead, the quantum anomalous Hall effect has been observed in twisted bilayer graphene and graphene/h-BN systems[9, 10].

Recently, to realize the quantum anomalous Hall effect, attempts to create ferromagnetism in

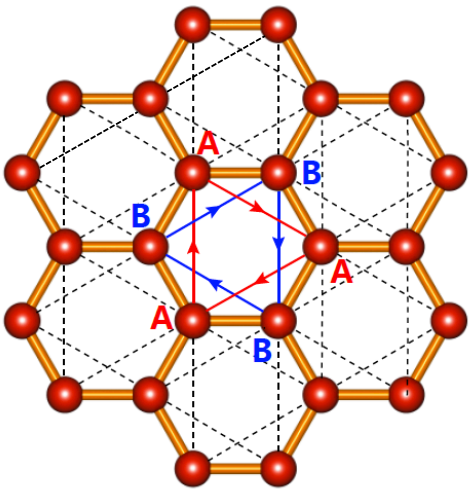


Figure 1.2. Haldane model for quantum Hall effect without Landau levels in graphene. Two inequivalent sites A, B belonging to the same unit cell are labelled. Dashed lines indicate the next nearest neighbor hopping and solid lines with arrows indicate the next nearest neighbor hopping direction.

nonmagnetic 2D materials like graphene emerge[9, 10]. One of the mostly adopted strategies is using vacancies or adding adatoms such as hydrogen and fluorine[11, 12, 13]. The local magnetic moments from unpaired electrons ware produced in graphene through such methods taking advantage of the defect engineering. However, ordering these moments in a long range is still very challenging during the material preparation. There are still some disputes over the feasibility of these approaches to form the long-range magnetic orders in graphene[14, 15]. The second way to realize the ferromagnetism in graphene is through the structure engineering instead of the structural imperfections[10, 16, 9]. By controlling the relative orientation between graphene or graphene/hBN layers, 2D ferromagnetism from originally nonmagnetic 2D materials is created and even the quantum anomalous Hall effect has been observed. For example, in bilayer graphene with electrical fields applied perpendicular to the basal plane, the two layers of graphene will experience different electrostatic potential and hence a gap can be induced. This gap is proved to be nontrivial and quantum anomalous Hall effect has been reported experimentally[16]. Nevertheless,

it is still challenging to precisely control and reproduce this kind of intrinsic magnetic properties of ultrathin film since these traditional thin films easily suffer from various perturbations including interfacial hybridization, electronic redistribution, atomic interdiffusion, strain, crystalline reconstruction, irregular shapes and so on. The third approach is from the magnetic proximity effect. This method makes nonmagnetic 2D material magnetic by borrowing properties from adjacent magnetic layers. Experiments were carried out by putting graphene onto ferromagnets. Examples like graphene/yttrium ion garnet (YIG)[17] and graphene/EuS [18] are experimentally shown that graphene becomes magnetic by showing the anomalous Hall effect or extracting the magnetic exchange field from nonlocal transport measurements. However, this anomalous Hall effect in graphene/YIG samples cannot be a direct evidence for the ferromagnetism in graphene since this effect in the transport measurements might comes from spin-dependent interfacial scattering or ferromagnetic impurities[19]. Proving the ferromagnetism in graphene through the quantification of the magnetic exchange field and observation of quantum Hall effect at a lower field in graphene/EuS is more convincing for the interfacial exchange coupling. Unlike ferromagnets, antiferromagnets (AFMs) are magnetically ordered with a net zero magnetization, which means that they produce no stray field and are always free of the external magnetic field perturbations. These properties make them promising for the reliable future spintronic devices. Theoretical calculations have shown the exchange coupling with a high energy of $\sim$70 meV and quantum anomalous Hall effect can be induced at graphene/$BiFeO_3$ structures. However, for this approach, the strong interfacial coupling cannot be easily obtained and it strongly depends on the physical properties of the materials themselves.

1.1.2 Transition metal dichalcogenides

TMDs have the form of MX_2, where M is a transition metal like W and Mo and X is a chalcogen like Te and Se. They offer a broad range of electronic properties ranging from insulating or semiconducting to metallic or semimetallic or superconductors. These different conductive properties result from the progressive filling of the nonbonding d bands by the transition metal electrons. All these TMDs have a hexagonal structure with a layer of metal atom sandwiched between two chalcogen layers. They also have a strong covalent bond for the atomic bonding within the layers and a weak vdW force between the layers. The presence of two constituent chemical species results in a predominant semiconducting nature, placing TMDs in a favorable perspective for electronic and spintronic applications. Besides, their metal-semiconductor crossover as a function of thickness and magnetic response of the semimetallic character give rise to a lot of interest over the years.

Among all the TMDs, 1T' WTe_2 is a special member of the TMD family and has been studied extensively in the past few decades due to its wide range of physical, chemical, electronic and optical properties. For the electronic properties, it can be a type-II Weyl semimetal[20, 21], quantum spin Hall insulator[22] and a superconductor[23] under different physical conditions. The crystal structure of 1T' WTe_2 is shown in Fig. 1.3, which is orthorhombic with space group $Pmn2_1$ and lattice parameters $a = 3.49\mathring{A}$, $b = 6.27\mathring{A}$, $c = 14.04\mathring{A}$. It is nonmagnetic and non-centrosymmetric. Both the transport measurements[24] and angle-resolved photoemission spectroscopy[25] show it has multiband semimetal nature.

Many physical properties of WTe_2 are related to the strong spin-orbit coupling inside this ma-

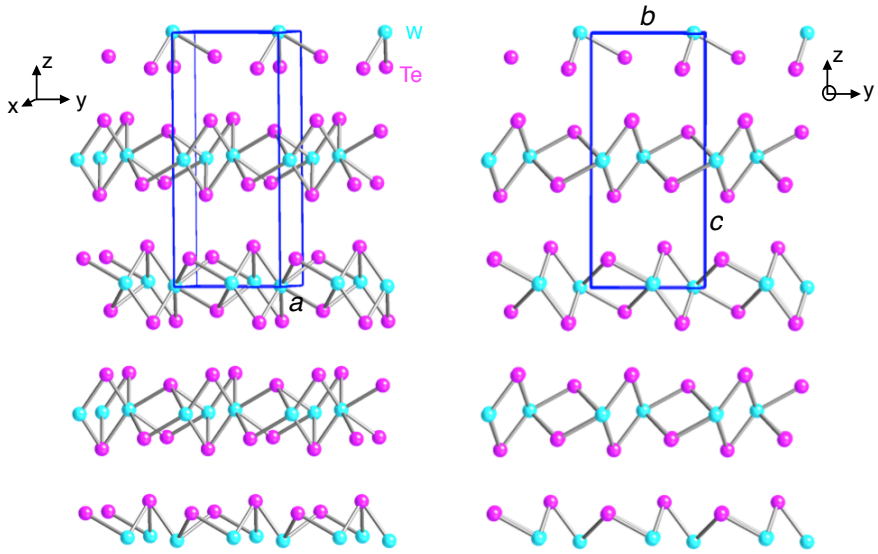


Figure 1.3. The crystal structure of WTe_2 with a unit cell. The graph was drawn with a software called CrystalMaker. Left graph shows the front 3D view and the right graph shows the front 2D view with lattice parameters $a = 3.49\mathring{A}$, $b = 6.27\mathring{A}$ and $c = 14.04\mathring{A}$.

terial, like the quantum spin Hall effect and large nonsaturating magnetoresistance. Spin-orbit coupling recently shows its potential applications in novel spintronic devices. It enables the flow of angular momentum between the spin angular momentum of the electronic system and the mechanical angular momentum of the lattice[26], which provides the opportunity for more energy efficient electrical manipulation of the magnetic order. Systems for investigating such spin-orbit effects are typically heavy metal/ferromagnet bilayers based on the spin-orbit torques. These spintronic devices can also utilize unique properties of quantum materials such as 2D TMDs. Materials like WTe_2 are adopted to study the spin-orbit torques[27]. In this dissertation, the strong spin-orbit coupling in WTe_2 is used to form an interface between a 2D ferromagnet, which would be explained in Chapter 3.

Ferromagnets	T_C (K)	Antiferromagnets	T_N (K)
$Cr_2Ge_2Te_6$	60[33]	$FePSe_3$	106[34]
$Cr_2Si_2Te_6$	32[33]	$FePS_3$	116[35]
CrI_3	45 [36]	$CrCl_3$	17[37]
Fe_3GeTe_2	220[38]	$Mn_1Bi_2Te_4$	25[31]
Others		VSe_2, $MnPS_3$, $MnPSe_3$, $FeCl_3$, α-$RuCl_3$, etc	

Table 1.1. Representative van der Waals magnets, including ferromagnets and antiferromagnets.

1.2 Intrinsic 2D magnetic materials

A list of the vdW magnets is shown in Table 1.1. The first reported 2D magnetic crystals are $Cr_2Ge_2Te_6$[28]. Later ferromagnetism and antiferromagnetism have been reported in CrI_3[29] with a layer number dependence. $Cr_2Ge_2Te_6$ is a 2D Heisenberg ferromagnet with small magnetic anisotropy with spin moments oriented toward all directions and CrI_3 is probably a 2D Ising A-type antiferromagnet with spin moments oriented normal to the basal plane. Thus CrI_3 has intralayer ferromagnetism and interlayer antiferromagnetism. Similar to $Cr_2Ge_2Te_6$, $Cr_2Si_2Te_6$ is also a ferromagnet. And the magnetic properties of $CrCl_3$ is similar to CrI_3. Later, 2D magnetic family is joint by a ferromagnet with a high Curie temperature (critical temperature for the transition from a paramagnet to a ferromagnet), Fe_3GeTe_2 (FGT). Different from those four Cr-based magnetic vdW materials which are relatively electrically insulating with a large gap, FGT is metallic. Fe-based magnetic family is further enlarged by including Ising antiferromagnets like $FePS_3$ and $FePSe_3$. Similar to these materials, $MnPS_3$ and $MnPSe_3$ are also antiferromagnets with a Néel temperature (critical temperature for the transition from a paramagnet to an antiferromagnet) close to that of $FePS_3$ and $FePSe_3$. In addition to these materials, room-temperature ferromagnetism has been reported in molecular beam epitaxy grown monolayer VSe_2[30]. Until recently, $Mn_1Bi_2Te_4$ is proved to be a vdW antiferromagnet, a quantum anomalous Hall insulator and an axion insulator[31, 32].

1.2.1 Fe-based vdW magnets

FGT is a metallic ferromagnet with a high Curie temperature. In each layer, three of the quintuple sublayers are iron, the top and bottom sublayers are tellurium, and the central one partly is germanium as shown in Fig. 1.4. Intrinsic magnetocrystalline anisotropy in FGT monolayers counteracts thermal fluctuations and preserves the 2D long-range ferromagnetic order, and this is precluded in an isotropic magnetic system according to the Mermin-Wagner theorem[39](this statement is based on three assumptions). The Curie temperature varies between 150 K and 220 K, which is largely dependent on the Fe concentration[40]. It has a strong perpendicular magnetic anisotropy with an energy of $\sim 10^7$ erg/cm^3, which is almost two orders of magnitude larger than that of $Cr_2Ge_2Te_6$ (10^5 erg/cm^3). For bulk and a few-layer FGT, magnetization characterization, electrical transport[38], scanning tunneling microscopy [41], and magnetic force microscopy[42] are adopted to investigate the magnetic phase.

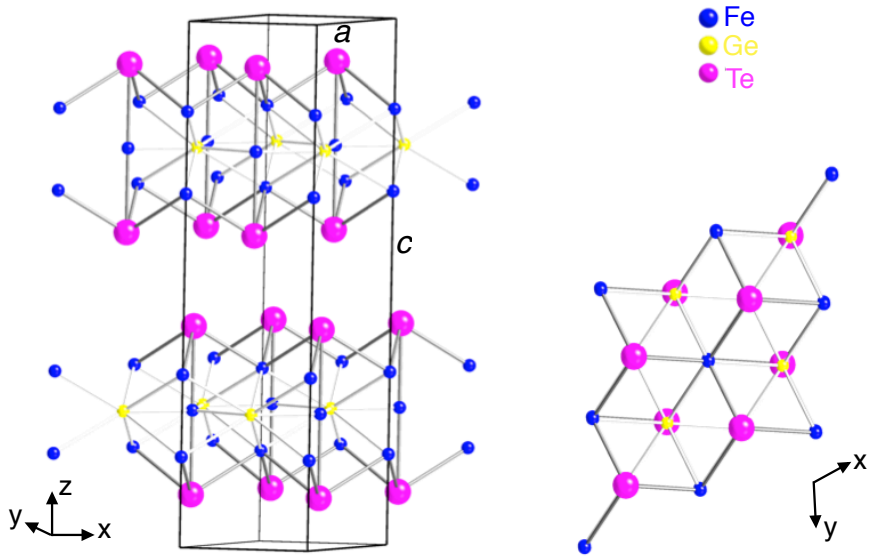


Figure 1.4. The crystal structure of FGT with a unit cell. The graph is drawn with a software called CrystalMaker. The left and right graph show the front 3D and 2D views. The lattice parameters are: $a = 3.99\mathring{A}$ and $c = 16.34\mathring{A}$.

In FGT, the interplay of both spin and charge degrees of freedom can be well investigated from its conductivity. Intriguing properties like large anomalous Hall current driven by topological nodal lines[43], with the spin degree of freedom quenched by the robust ferromagnetic polarization and line degeneracy protected by crystalline symmetries, demonstrate that orbital-driven nodal line is an effective source of a large AHE in hexagonal vdW ferromagnets and provides some insights for the design of ferromagnetic vdW materials with a large anomalous Hall effect. Besides, it is found that the itinerant ferromagnetism in FGT can persist in monolayer form with an out-of-plane magnetocrystalline anisotropy, and with an ionic liquid gate the Curie temperature of a four-layer FGT can be lifted to the room temperature[38]. Another work[42] found out that FGT transforms from 3D to 2D Ising ferromagnetism at a thickness around five layers, with a fast drop of Curie temperature from 207 K down to 130 K. For thick FGT more than $\sim$ 15 nm, the magnetic transition in FGT under a magnetic field showing no square hysteresis is related to the formation of labyrinthine domain structures.

1.2.2 Mn-based vdW magnets

Mn-based vdW magnets includes ferromagnets like $MnSe_x$[44] and antiferromagnets like $MnPS_3$[45] and $Mn_1Bi_2Te_4$. Among all the vdW magnets, $Mn_1Bi_2Te_4$ is experimentally proved to be an intrinsic magnetic topological insulator. Before discovery of the few-layer $Mn_1Bi_2Te_4$, magnetic topological insulator has only been realized by doping nonmagnetic topological insulators with $3d$ transition metals, which leads to strongly inhomogeneous magnetic and electronic properties of these materials and limits the observation of quantum effects at low temperatures. $Mn_1Bi_2Te_4$ is a layered ternary tetradymite compound that consists of Te-Bi-Te-Mn-Te-Bi-Te septuble layers.

This materials can be viewed as layered Bi_2Te_3 with a Mn-Te bilayer inserting between each of its Te-Bi bonds as shown in Fig. 1.5. The magnetism in this material originates from the Mn^{2+} ions in the crystal, which has a spin of S=5/2 and a large magnetic moment of $\sim 5\mu_B$, where μ_B is the Bohr magneton. The magnetic coupling between the septuble layers is antiferromagnetic with ferromagnetic ordering in adjacent septuble layers. The bulk $Mn_1Bi_2Te_4$ is an antiferromagnet with a Néel temperature of $T_N = 25$ K.

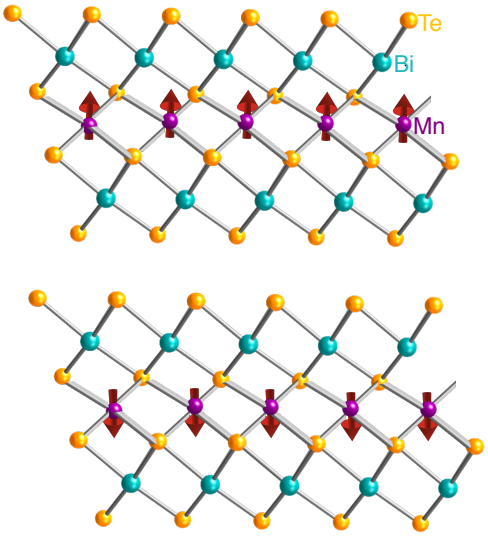


Figure 1.5. The schematic two septuple layers of $Mn_1Bi_2Te_4$ with the antiferromagnetic coupling between layers. The yellow, green and purple spheres are for Te, Bi and Mn atoms, respectively. The red arrows indicate the spin polarization directions for Mn atoms.

First principle calculations[46] show the fundamental gap value for the bulk is around 220 meV. And at certain parameter range, a non-zero nontrivial topology of $Mn_1Bi_2Te_4$ can be generated. It is classified as an antiferromagnetic topological insulator[46]. For the experimental parts, the odd-layer $Mn_1Bi_2Te_4$ is reported to be a quantum anomalous Hall insulator at 1.4 K and with a large external magnetic field the quantization temperature can be raised up to 6.5 K[31]. Due to the antiferromagnetic coupling between layers, the odd-layer $Mn_1Bi_2Te_4$ is a ferromagnet and even-layer $Mn_1Bi_2Te_4$ is a antiferromagnet. Thus the ferromagnetism in odd-layer $Mn_1Bi_2Te_4$ breaks

the time reversal symmetry and turns it into a quantum anomalous Hall insulator, also a Chern insulator. In even-layer $Mn_1Bi_2Te_4$, for example a six septuble-layer device, a large longitudinal resistance and zero Hall plateau have been observed[32], suggesting an axion insulator state in zero magnetic field over a wide magnetic field range and at relatively high temperatures. When a large enough magnetic field is applied, it becomes a quantum anomalous Hall insulator with a quantized Hall resistance of h/e^2, where h is Planck's constant and e is electron charge. Later, Chern insulating states with different quantization values of $h/\nu e$ (ν is an integer) have also been discovered in this material system[47].

1.3 2D magnetism

Driven by the exchange coupling with interaction between the neighboring spins, spin orientations favor specific relative directions between them. Thus an ordered arrangement of magnetic moments over macroscopic length scales exists, resulting in a spontaneous time-reversal symmetry breaking. Theoretically at zero temperature, this local order can extend to large scales. However, the increasing temperature will always lead to thermal fluctuations and misalign the moments. In three-dimensional case, a magnetic phase transition always happens at a finite temperature while in one-dimensional case a long-range order only occurs at a zero temperature[48]. Whether or not a system undergoes a phase transition across a finite temperature in 2D case is decided by the effectiveness of thermal fluctuations on the spin textures, which is related to its presence and the strength of magnetic anisotropy as shown in Fig. 1.6. When the spins are aligned in a line (2D Ising model) as shown in Fig. 1.6a, Onsager[49] provided an exact solution and showed a

magnetic phase transition at $T_C > 0$. In this case, the anisotropy of the system results in a gap opening in the spin-wave spectrum and suppresses the effect from the thermal fluctuations. Based on the finite-range exchange interactions, Mermin and Wagner[39] proposed an isotropic Heisenberg model which concluded that thermal fluctuations could destroy long-range magnetic order in 2D system at any finite temperature with the spins arranged in all directions (Fig. 1.6c). This theory is based on the idea that the excitation of spin waves can destroy the magnetic order, with the magnetization at a temperature T expressed as:

$$M(\mathrm{T}) = M(\mathrm{T}=0) - \Delta M(\mathrm{T}). \tag{1.1}$$

The reduction term $\Delta M(\mathrm{T})$ is due to the thermal excited spin waves. This term is related to the dimensionality of the system and probability for the thermal occupation with the form of $\Delta M(\mathrm{T}) \sim \int_0^\infty N(E)[1/(e^{E/k_\mathrm{B}T}-1)]dE$, where $N(E)$ is the density of states of the excitations depending on the system dimensionality. In a general case where excitations has a dispersion of $E \sim k^n$ and a volume of $k^{d-1}dk$ in a d-dimensional k space, the density of states can be approximated as $N(E) \sim E^{(d-n)/n}$. For the dispersion of spin-waves in a ferromagnet with the Heisenberg Hamiltonian $n = 2$ and two dimensions $d = 2$, the density of states is a constant. Thus the reduction term $\Delta M(\mathrm{T})$ diverges for finite T, indicating the breakdown of the magnetic order. They conclude at finite temperatures the spin waves are infinitely easy to excite and can destroy magnetic orders. However, this theory is based on the assumptions of isotropic interactions, short-range interactions and the dimension of two or smaller. All three assumptions can be false since magnetic orders can be stabilized by anisotropy, longer-range interaction or a slightly

higher dimension. It has been recently proved that even a small uniaxial magnetic anisotropy can open up a large excitation gap and lift the restrictions imposed by the Mermin-Wagner theorem. As a result, 2D magnets can survive at a finite temperature. For the case of spins orienting in a plane as shown in Fig. 1.6b, referred to as the XY model, there is no magnetic transitions conventionally. Berezinskii[50], Kosterlitz and Thouless[51] point out there are an algebraic decay of spin correlations and the bond of the pairs of vortex and antivortex arrangements of spins in this system. And they conclude below the Kosterlitz-Thouless temperature T_{KT} that a quasi-long-range magnetic order can be established in this system, where in the margin of the system a finite order parameter is suppressed. Before thinning down the vdW materials into 2D region, this theory has been validated in magnetic thin films grown on a substrate[52] and 3D layered transition metal compounds[53] over the past several decades.

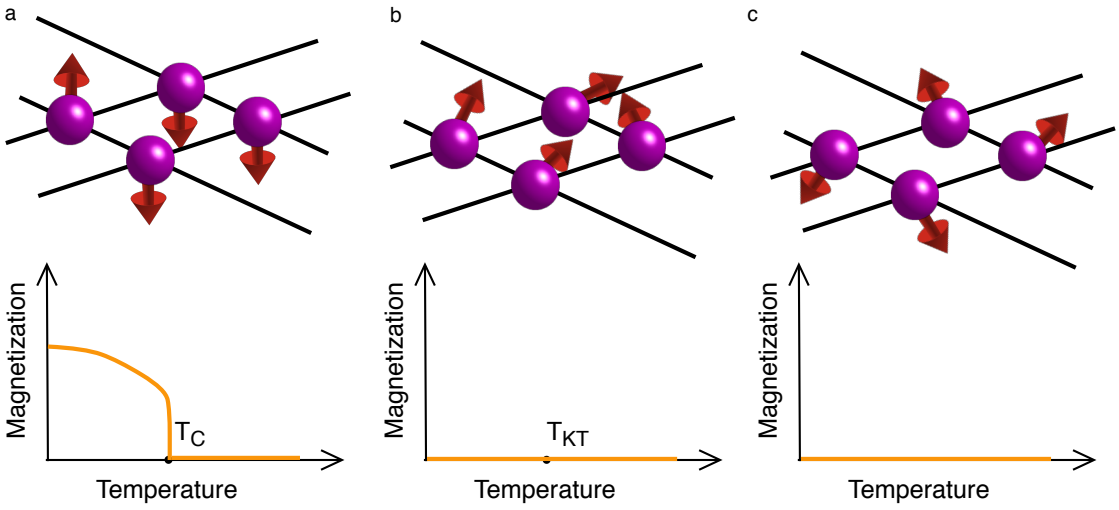


Figure 1.6. Thermal fluctuation effects on the spin dimensionality. **a**, Ising model with spin aligning in a line. Spin dimension of one. **b**, XY model with spin residing in a plane. Spin dimension of two. **c**, Heisenberg model with spin in all directions. Spin dimension of three.

A generalized Heisenberg spin Hamiltonian can be used to describe the 2D magnetism[54]:

$$H = -\frac{1}{2}\sum_{<i,j>}(J\mathbf{S}_i \cdot \mathbf{S}_j + \Lambda S_i^z S_j^z) - \sum_i A(S_i^z)^2, \tag{1.2}$$

where J is the exchange coupling between spins $\mathbf{S}_i$ and $\mathbf{S}_j$ on neighboring sites with $J > 0$ for ferromagnetic order and $J < 0$ for antiferromagnetic order. And A and Λ are the on-site and inter-site exchange magnetic anisotropies, respectively. The Ising model and XY model correspond to $A \to +\infty$ and $\to -\infty$, respectively. The isotropic Heisenberg model representing the spins in all directions corresponds to the absence of magnetic anisotropy, that is $A \sim 0$ and $\Lambda \sim 0$. This Hamiltonian also considers the dipole-dipole interactions, but is not applicable to systems including neighboring magnetic coupling or any other couplings.

1.4 Detection of 2D magnetism

Methods to detect the 2D magnetism in a small scale with a size of several square micrometers (the size of mostly exfoliated monolayer or few-layer vdW magnets) are rather limited. Currently, mostly adopted measurements are based on microscopy, optics and electronic probes.

Microscopy measurements for 2D magnets include Lorentz transmission microscopy (L-TEM), single-spin microscopy and photoemission electron microscopy. These techniques help map either morphology or structure of the materials based on behaviors of the ions, electrons, photons or physical cantilevel probes. Informations about spin arrangement and magnetic domain in the real space can be collected under external fields. L-TEM can provide the information about magnetic domains in the real-space with a resolution under 5 nm and the skyrmion lattice images under mag-

netic fields and different temperatures. Its principle is based on the Lorentz force which electrons experience under a magnetic field. Meanwhile, single-spin microscopy provides high spatial resolution at the nanoscale and can detect a single atomic spin by taking advantages of the exceptional properties of a defect in diamond called a nitrogen-vacancy center. A diamond nanocrystal with a nitrogen-vacancy center is embedded in the tip of an atomic force microscopy probe. When the tip approaches the material surface, the local magnetic field of the materials causes the Zeeman splitting in the energy level of the nitrogen-vacancy center. The resulting fluorescene intensity depends on the position of the atomic force microscopy tip, which corresponds to the magnetic distribution of the material. One example of applying this method is the study of the magnetic properties of CrI_3 with the magnetization of monolayers determined to be $\sim$ 16 Bohr magnetons per square nanometer[55]. Another technique is photoemission electron microscopy, a powerful surface imaging technique with an ultrahigh resolution through the detection of electrons from a sample surface. This method has been applied to investigate the magnetic domain in FGT and it is reported that the ferromagnetism can persist up to room temperature induced by the patterning[56]

.

Optical probes function through light-matter interaction with the advantages of simple operations and high sensitivity. Optical characterizations like Raman scattering, photoluminescence and magneto-optic Kerr effect (MOKE) have been used to investigate the magnetization of 2D magnets. However, they are not as efficient as the microscopy methods in providing the mapped magnetic domains of the thin film. Raman is a conventional way to identify the structural information and optical properties based on the spin-phonon interaction and lattice dynamics. Three phase transition temperatures of $MnPS_3$ have been reported using the polarized Raman spectroscopy[57]. Unlike

Raman, photoluminescence probes the photoexcitation process light absorption. With spontaneous circular polarization photoluminescence, the helicity can be determined by the magnetization direction in the case monolayer CrI_3[58]. MOKE detects the change of the polarization of an incident light when reflected or transmitted by a magnet. It is widely adopted for the measurement of physical properties of magnetic thin films, like magnetic domain, spin density of states and magnetic phase transition. As examples, the discovery of the ferromagnetism in CrI_3[59] and $Cr_2Ge_2Te_6$[28] was using MOKE.

Since the electronic properties of 2D magnets are significantly affected by their magnetic orders, electronic transport studies of longitudinal resistance and Hall resistance can also provide some information about the magnetizations. Magnonics or magnon-based spintronics of 2D magnets combine the magnetization and spin waves in the nanoscale materials. Such magnon-modified transport behaviors of a 2D antiferromagnet $MnPS_3$ have been observed by the longitudinal resistance measurements[60], with magnon propagation over several micrometers. The Hall effect, especially the anomalous Hall effect and quantum anomalous Hall effect, can be used to determine the ferromagnetism and estimate the Curie temperature of the materials.

The extraordinary properties of 2D magnets make them a promising candidate for the future spintronic and electronic applications. Exploring the intrinsic properties of these materials not only helps understand the physical mechanism of low-dimensional films, but also exists in developing the next-generation devices down to the atomic scales with an ultra-compact configuration.

1.5 Magnetic heterostructure based on 2D materials

The use of 2D materials as part of the heterostructures not only expands the functionality of the heterostructure for the future applications, but also enables the phenomena from proximity effect to study the magnetic properties of the materials. Through the interface engineering of 2D magnets, charge transfer occurs first, which effectively changes the carrier concentration and orbital occupation in the materials. Second, the interface dipole or built-in electric field can modify the electronic properties of the 2D magnets. Third, interfacial orbital hybridization may affect the magnetic properties of the 2D materials, which is the case of induced magnetism in our graphene/CrSe heterostructures which will be discussed later in Chapter 2. Fourth, lattice strain may exist at the interface of the heterostructure, resulting in the properties change in the materials. Fifth, there are exchange interactions between the materials. Sixth, a brand new lattice may form when a 2D magnet interfaces with a material with a similar lattice constant, which is the case of twisting bilayer graphene or band renormalization in graphene on h-BN. Seventh, the dielectric screening of electron-electron interaction exists at the interface[61]. Last but not least, spin-orbit proximity effect can play an important role when 2D magnets are coupled to heavy elements, which is the case of emergent skyrmions in our FGT/WTe_2 heterostructure which will be discussed later in Chapter 3.

With strong covalent bonds formed between atoms within the plane, the layers are connected with the vdW interaction, which is a great advantage when stacking these materials together. The seamless integration and interplay of vdW heterostructure can produce a large interfacial exchange interaction. For example, CrI_3/WSe_2 heterostructure has a large interfacial exchange energy mea-

sured through circularly polarized photoluminescence, which is equivalent to the effect of a 13 T magnetic field. This is explained due to the lifted valley degeneracy of WSe_2 via flipping the magnetization of CrI_3[62]. Apart from combing 2D magnets with 2D materials, a Pt/FGT heterostructure has also been investigated. The spin current generated in Pt can switch the magnetization of the FGT layer by exerting a damping-like spin orbital torque from Pt[63].

1.6 Sample assembly using pick-up transfer technique

Although some few-layer 2D materials like graphene can be synthesized by chemical vapor deposition or molecular beam epitaxy method with good control and uniformity, the quality (like carrier mobility) of materials obtained from these methods are still not as good as the exfoliated ones from the bulk. The exfoliation method usually produces flakes with different sizes and thicknesses randomly distributed over the substrate, which includes a few atomically thin flakes. Thus optical identification like microscopy is engaged to find atomically thin crystals with a relatively large size from a crowd of thick bulky flakes.

However, the combination of mechanical exfoliation and microscopy only still cannot directly provide more complex system like heterostructures, which is formed by stacking different material thin films and requires an accurate alignment under a microscope. To fabricate such system, a pick-up transfer technique is needed as schematically shown in Fig. 1.7. In this method, two sample planes are required to hold the samples, where one is attached to the slide glass and the other one is placed onto the heater. While tuning the focus of the microscope, two sample planes can be clearly seen under the microscope and thus the relative positions of two sample can be accurately

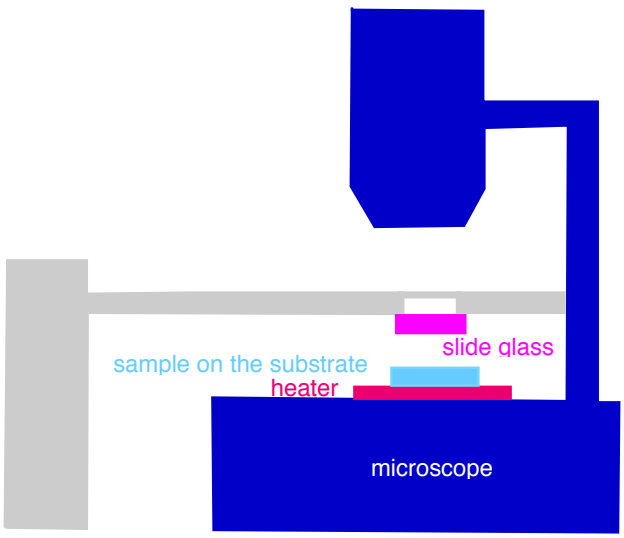


Figure 1.7. Schematic illustration of the sample assembly. There are two sample planes under the microscope. One is on slide glass and the other one is on the substrate as indicated. The heater is used to apply heat with DC current during pick-up and transfer procedure.

aligned. When putting the two samples together, a heater is switched on to help the sample on the slide glass fall onto the other sample on the substrate. Our homemade pick-up transfer stage is shown in Fig. 1.8, which uses one microscope with long-distance objective lens, one xyz stage, one xy stage, one rotation stage, one CCD, one heater, and one DC power supply. The images are obtained through the CCD which is linked to a computer. To protect the few-layer sample from air conditions, the pick-up transfer process is done inside a glove box filled with inertia gas of N_2 gas.

One example of using the pick-up transfer technique to fabricate black phosphorus/graphene heterostructure is shown in Fig. 1.9. Before doing the transfer, thin films of polydimethylsiloxane (PDMS)/Polypropylene carbonate (PPC) are coated on the slide glass. Then these layers are used to pick up the black phosphorus exfoliated on the 300 nm-thick SiO_2/Si substrate. When PDMS/PPC is attached to the black phosphorus, the heater is on for 10 minutes and the temperature is raised to $\sim$ 50°C. After turning the heater off, the slide glass is detached from the substrate and black phosphorus is sticked to the PPC. Then PDMS/PPC/black phosphorus on the slide glass is used to

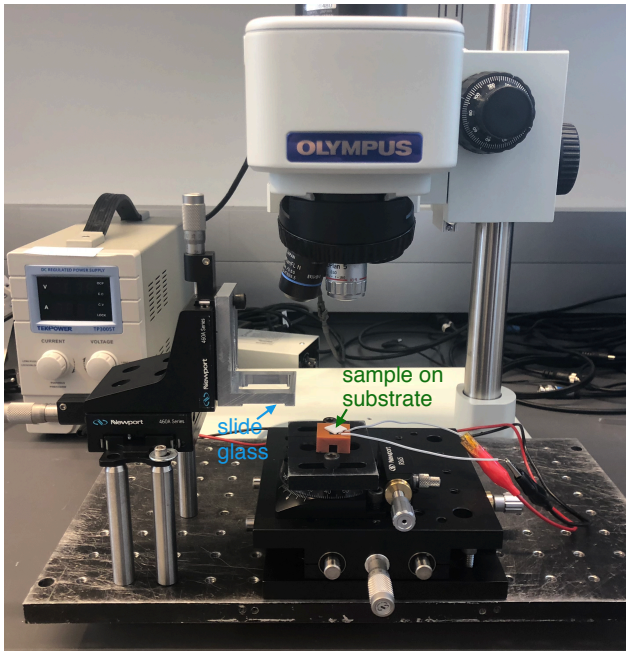


Figure 1.8. Homemade sample assembly facility using pick-up transfer technique. The top white part is the microscope with objective lens. The left white part is the heater. Slide gas is attached to a XY aligner and sample on the substrate is attached to the heater which is on a XY stage.

pick up graphene on the substrate using the similar heating process. After that, PDMS/PPC/black phosphorus/graphene layers can be put onto any desired substrate by heating up to $\sim 70^{\circ}$C. Since the PPC can be dissolved in acetone, the black phosphorus/graphene/any substrate sample is ready after being taken out from acetone.

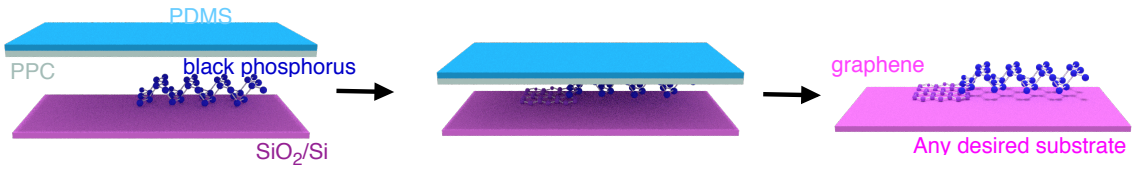


Figure 1.9. Black phosphorus/graphene heterostructure assembly using pick-up transfer technique. PDMS/PPC is used to pick up black phosphorus exfoliated onto the SiO_2/Si substrate first. After pick-up, PDMS/PPC/black phosphorus is used to pick up graphene. After transferring PDMS/PPC/black phosphorus/graphene onto any desired substrate and dipping in acetone, heterostructures can be formed.

1.7 Outline

In this dissertation, we summarize our work on the proximity effect of graphene/antiferromagnet and WTe_2/FGT heterostructures. The contents are arranged as the following. In Chapter 2, crystal and magnetic structure of CrSe thin film, magnetized graphene from transport and MOKE measurements and Landau level fitting using machine learning are shown in details. In Chapter 3, transport properties of FGT, transport properties of WTe_2, topological Hall effect in the heterostructure, Néel-type skyrmions under L-TEM, micromagnetic simulations and comparison between the transport and L-TEM results are discussed.

Chapter 2

Magnetism in graphene coupled to an antiferromagnet

To realize the quantum anomalous Hall effect in graphene, one way is to induce local magnetic moments, like doping atoms with unfilled d or f shells[64]. Different from doping, proximity coupling does not bring unnecessary disorder to graphene. It is reported that ferromagnetism in graphene has been observed in graphene/YIG heterostructure[17] where YIG is a ferromagnet with a high Curie temperature of 560 K. The hybridization between the π orbitals in graphene and nearby spin-polarized d orbitals in magnetic insulators gives rise to the exchange interaction required for long-range ferromagnetic ordering. Like ferromagnets, antiferromagnets (AFMs) are magnetically ordered.

In this part, quantum oscillations in monolayer graphene interfaced with CrSe thin film, an AFM, have been observed. A sizable exchange coupling was detected from the π bond formed by the p orbitals of carbon and Cr atoms in the CrSe layer. When the field-cooling was applied, changes in the interfacial antiferromagnetic order significantly modify the exchange splitting of graphene, making the quantum oscillations shifted to a larger or smaller magnetic field strength according to the cooling-field strength and direction. The magnetism induced into graphene from the proximity effect was also confirmed by the MOKE measurements. This spin-splitting energy

is estimated to be $\sim$ 134 meV from fitting Landau level index using the machine learning.

2.1 Crystal and magnetic structure of CrSe film

Bulk $Cr_{1-\delta}Se_{1+\delta}$ is known to have a complex phase diagram. For example, when δ is in the range of $0 \leq \delta \leq 0.05$, this material has more than six stable phases, all of which are pseudo-NiAs phase at room temperature. To confirm this as-grown CrSe film has a NiAs-type crystal structure and antiferromagnetic orders, transmission electron microscopy (TEM), X-ray diffraction (XRD) and neutron diffraction measurements have been carried out. All the results have shown the CrSe thin films used in our experiment is an antiferromagnet with a NiAs-type structure and a Néel temperature of $\sim$ 270 K.

CrSe thin films were grown in an ultra-high vacuum Perkin-Elmer molecular beam epitaxy (MBE) system. Semi-insulating GaAs [111B] (001) substrates were cleaned by acetone with ultrasonic for 10 minutes before being loaded into the growth chamber. To effectively remove the native oxide, Se rich atmosphere was used to do the thermal annealing up to 580°C. During the growth of CrSe, a two-step growth method was adopted, where the first step was to maintain the GaAs substrate at 200°C with the Cr and Se shutters open at the same time and the second one was raising the substrate temperature to 400°C and maintaining at this temperature to finish growth with the same Cr and Se flux. This epitaxial growth was monitored by an *in situ* reflection high-energy electron diffraction technique.

2.1.1 Crystal structure from TEM and XRD

In this study, CrSe thin films were grown on GaAs [111]B substrates by molecular-beam epitaxy method. The NiAs-type CrSe crystal structure is shown in Fig. 2.1, with alternating basal planes of Cr and Se.

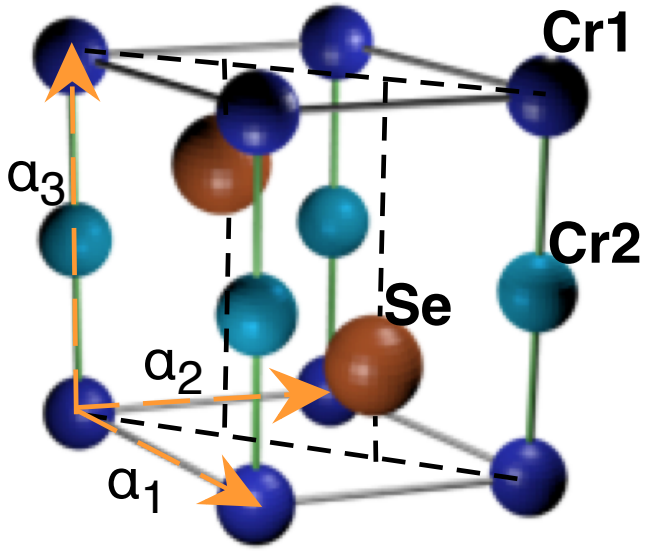


Figure 2.1. NiAs-phase CrSe with alternating layers of Cr and Se atoms and labelled axis for the unit cell. The lattice parameters for the unit cell are: $a_1 = a_2 = 3.60\,\mathring{A}$ and $a_3 = 5.81\,\mathring{A}$.

The cross-section of the high-quality interface via TEM is shown in Fig. 2.2. The line scan indicates a high quality NiAs-type structure with evidence of ordered Cr vacancies as expected, and the Cr vacancies are in the form of dark horizontal stripes. The NiAs-phase is fully developed after one or two seeding layers of CrSe interfacing with GaAs. In the experiment, monolayer graphene was put to the top surface of CrSe, with a well-developed NiAs-phase CrSe thin film shown under TEM.

From the XRD, the lattice parameters can be extracted, with $a_1 = a_2 = 3.60 \pm 0.01\,\mathring{A}$ and $a_3 = 5.81 \pm 0.01\,\mathring{A}$, respectively. These values are close to those reported for NiAs-CrSe and

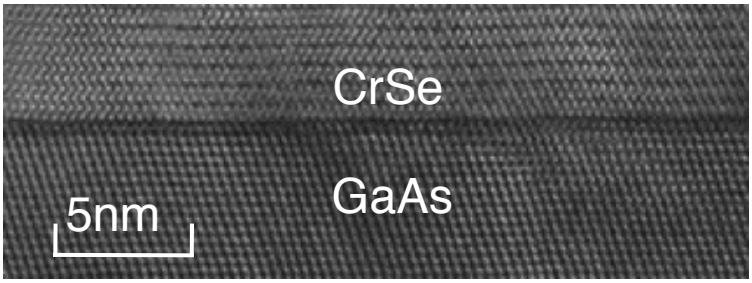


Figure 2.2. Transmission electron microscopy for side view of CrSe/GaAs heterostructure indicates the good quality of CrSe.

Cr_7Se_8 [65, 66]. Considering the deposition temperature of 230°C for the first step and 400°C for the second step and the relative strength of the (001) and (002) diffraction peaks, the thin film was expected to have a composition relatively near the stable window of a mixed phase of CrSe and Cr_7Se_8[66, 67, 68].

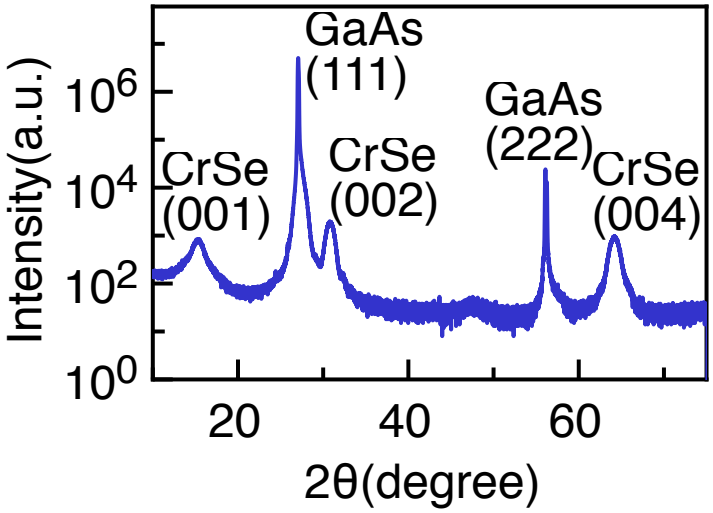


Figure 2.3. X-ray diffraction shows that CrSe has a NiAs-type crystal structure.

2.1.2 Spin texture from neutron diffraction

The TEM and XRD measurements show the thin film grown by MBE method has a crystal structure close to NiAs-phase. More importantly, the antiferromagnetic order in this thin film

should be investigated and confirmed. Thus neutron diffraction was carried out by our collaborators in National Institute of Standards and Technology, which revealed strong temperature dependent $(200)_{\text{Mag}}$ and $(201)_{\text{Mag}}$ Bragg peaks shown in Fig. 2.4. The 'Mag' subscript indicates that the peaks may be indexed using the rotated and expanded unit cell as described in the previous work[65]. The presence of such a large fully in-plane magnetic diffraction peak $(200)_{\text{Mag}}$ requires a large spin component along the growth axis, that is the out-of-plane direction. Further, the in-plane contribution of the $(200)_{\text{Mag}}$ and $(201)_{\text{Mag}}$ peaks can be translated into the structural unit cell, and it indicates a [$\frac{2}{3}$, $\frac{2}{3}$,0] in-plane propagation vector. This suggests a non-collinear antiferromagnetic order in this CrSe thin film.

Fitting the temperature-dependent peak intensity of CrSe films on GaAs using a mean-field Brillouin function gives the Néel temperatures of 273 ± 8 K and 270 ± 7 K, respectively. These results are consistent with the reported Néel temperature for bulk CrSe, which is approximately 280 K[65]. As a result, the high-temperature non-collinear antiferromagnetic ordering with an out-of-plane spin component has been proved in this thin CrSe films.

2.1.3 Transport properties of CrSe film

The Néel temperature in the CrSe thin film matches that in the bulk form, however, the transport properties of this thin film differ from that in the bulk[65]. As has been reported before, the bulk CrSe is metallic[69]. In our case, the 60 nm-thick CrSe film is metallic and shows a decreasing resistivity when the temperature decreases (Fig. 2.5). However, for 30 nm-thick CrSe, which was put next to a monolayer graphene in this experiment, shows an increasing resistivity when

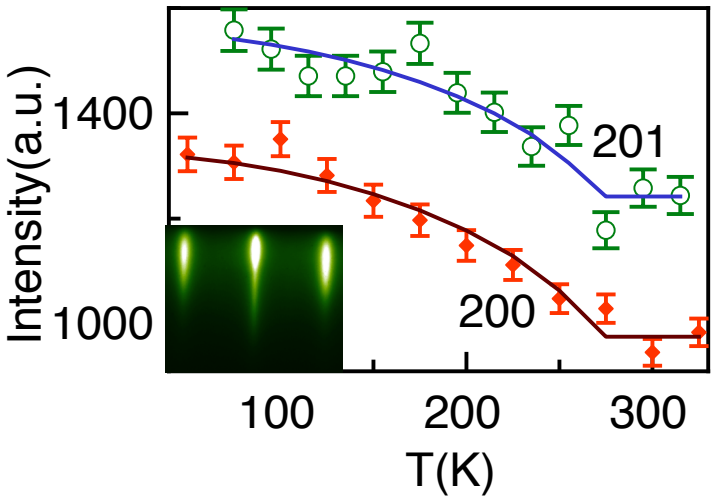


Figure 2.4. Neutron diffractions of $(200)_{Mag}$ and $(201)_{Mag}$ Bragg peaks indicate the Néel temperature for our AFM thin films is close to the reported values in bulk. The dots are the measured data and the lines are the fitting curves. Error bars represent a single standard deviation. The inset shows the reflection high-energy electron diffraction during molecular beam epitaxy growth of CrSe on GaAs.

the temperature decreases. This deviates from the metallic behavior. The origin of this thickness dependent transport behaviour is unclear at the present stage. Possible reasons are vertical quantum confinement in thinner films and band bending due to interfacial electrostatics. Nevertheless, the 30 nm-thick CrSe have been shown to be semiconducting with an out-of-plane antiferromagnetic order.

2.2 Magnetized graphene from transport and MOKE measurements

Monolayer graphene was first mechanically exfoliated onto a 300 nm-thick SiO_2/Si substrate and then transferred onto the the CrSe thin film. To form the heterostructure, the dry transfer method was adopted. First, the PDMS stamp sticked to a glass slide was coated with a

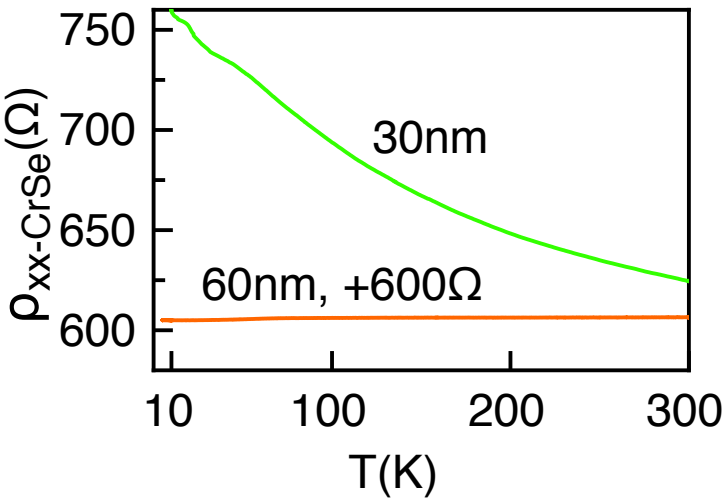


Figure 2.5. Temperature dependent resistivity of 30 nm-thick and 60 nm-thick CrSe films. 60 nm-thick CrSe is metallic while 30 nm-thick CrSe is semiconducting.

thin film of PPC. The monolayer graphene on the 300 nm-thick SiO_2/Si was picked up by the PDMS/PPC on the glass slide by heating up to 50°C. After that, the PDMS/PPC/graphene tri-layer was aligned with the CrSe/GaAs. After heating up to 110°C, PPC detached from PDMS and the PPC/graphene/CrSe/GaAs structure was formed. Then acetone was used to remove the PPC thin layer and graphene/CrSe heterostructure was formed after the removal. Since a monolayer graphene has a low contrast on the CrSe/GaAs substrate, whereas it does have a good contrast on SiO_2, the monolayer graphene pieces which are close to an adjacent multilayer one were always chosen to be the ideal sample. In this case, the multilayer piece could serve as a locator for finding the monolayer graphene on CrSe/GaAs substrate. Hall-bar devices with dimensions of 13 μm$\times$ 6 μm were fabricated using standard photolithography later for the electrical measurements.

Raman spectroscopy are measured with a 20$\times$ objective at 514 nm with a Renishaw micro-Raman spectrometer, having a 1800 grooves/mm grating and spectral resolution of $\sim$3 cm^{-1}. This suggests a monolayer graphene on CrSe/GaAs and the absence of the D peak indicates a low level

of disorder as shown in Fig. 2.6.

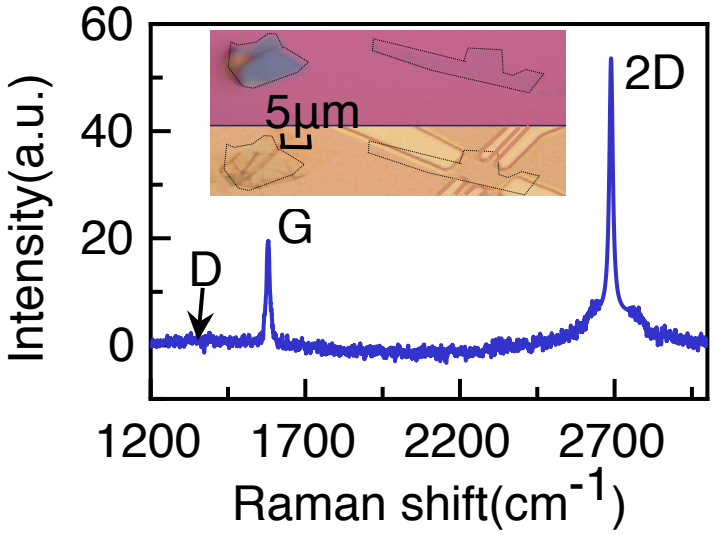


Figure 2.6. Raman spectroscopy of monolayer graphene indicates the monolayer graphene with a high 2D peak and a low level of disorder with a negligible D peak. The inset shows the microscopic image of graphene/CrSe before (top graph) and after (bottom graph) doing photolithography. The nearby thick flake on the left side of the graph serves as a locator when doing photolithography.

2.2.1 Field cooling dependence of graphene/CrSe heterostructure

The transport measurements were carried out with the physical property measurement system (PPMS) with a magnetic field range of ± 9 T and a temperature range from 2 K to 400 K. After cooling down the sample temperature from room temperature to 2 K, the magnetoresistivity of this heterostructure ρ_{xx} was measured, which showed quantum oscillations under an applied out-of-plane magnetic field (Fig. 2.7). Some kinks also appeared in the Hall resistivity at large magnetic fields. As expected, given the antiferromagentic nature of CrSe, no ferromagnetic hysteresis was observed when sweeping the magnetic fields back and forward.

Field cooling is well known as a convenient method to introduce exchange bias in heterostructure formed by a ferromagnet and an antiferromagnet[70, 71, 72, 73]. The field cooling is done by

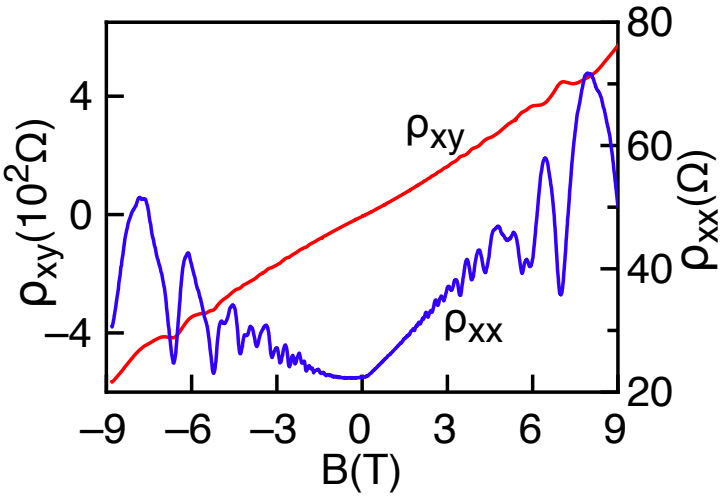


Figure 2.7. Magnetoresistivity in the blue curve and Hall resistivity in the red curve for graphene on 30 nm-thick CrSe with no external magnetic field when cooling down. Quantum oscillations of longitudinal resistivity and dips of Hall resistivity were observed.

applying an external magnetic field above the Néel temperature (T_N) and lowering the temperature to a base temperature which is much lower than T_N as schematically shown in Fig. 2.8. When the temperature reaches the base value, the external magnetic field can be withdrawn. For antiferromagnets alone, it was reported recently that field coolings could manipulate the Néel vector for a certain case of anisotropy [74]. In our case, uncompensated spins are expected to be on the CrSe surface since half of their neighboring antiparallel moments are missing. Thus, the surface moments of CrSe can be pinned at field coolings under an external magnetic field, resulting in a net magnetic moment frozen out of plane. The Cr-d orbitals of these frozen moments overlap with the p orbitals on the adjacent carbon atoms, inducing a spin splitting energy, Δ. And this energy can be modulated through the magnitude and direction of the cooling fields.

For the graphene/CrSe heterostructure, quantum oscillations have been observed in the magnetoresistivity measurements. When applying different field coolings, the quantum oscillations dips and peaks are shifted according to the field coolings as shown in Fig. 2.9. The same dip as denoted

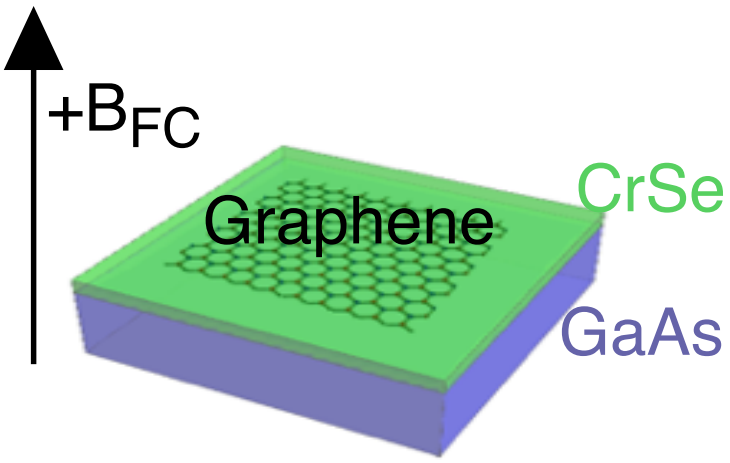


Figure 2.8. Schematic graph for graphene/CrSe under field coolings. The black arrow indicates the applied magnetic field direction. The hexagonal lattice is graphene. The green and purple cuboids are CrSe and GaAs layers, respectively.

by the dashed in Fig. 2.9 are shifted by the field coolings, where the positive field cooling shifts the quantum oscillations rightwards and negative one shifts the oscillations leftwards.

The same pattern occurs for the Hall channel as well (Fig.2.10). As indicated by the dashed arrow, the kink is moved to a larger magnetic field when the field cools down with a positive magnetic field.

To exclude the possibility that the oscillations and shifts are from CrSe layer since it also contributes to one conducting channel in this heterostructure, the transport properties of pristine CrSe thin layers grown on GaAs substrates (Fig. 2.11) have been investigated. The longitudinal resistivity of CrSe of the control sample $\rho_{xx-\mathrm{CrSe}}$ is only greater than longitudinal resistivity of the heterostructure ρ_{xx} by about one order of magnitude. The quantum oscillations are completely suppressed in the control pristine CrSe, and thus definitely attributing the quantum oscillations observed in the heterostructure to the the Landau levels in the graphene layer. Since the carriers of CrSe are also involved in the transport measurements and the Hall resistivity of CrSe film $\rho_{\mathrm{xy\text{-}CrSe}}$

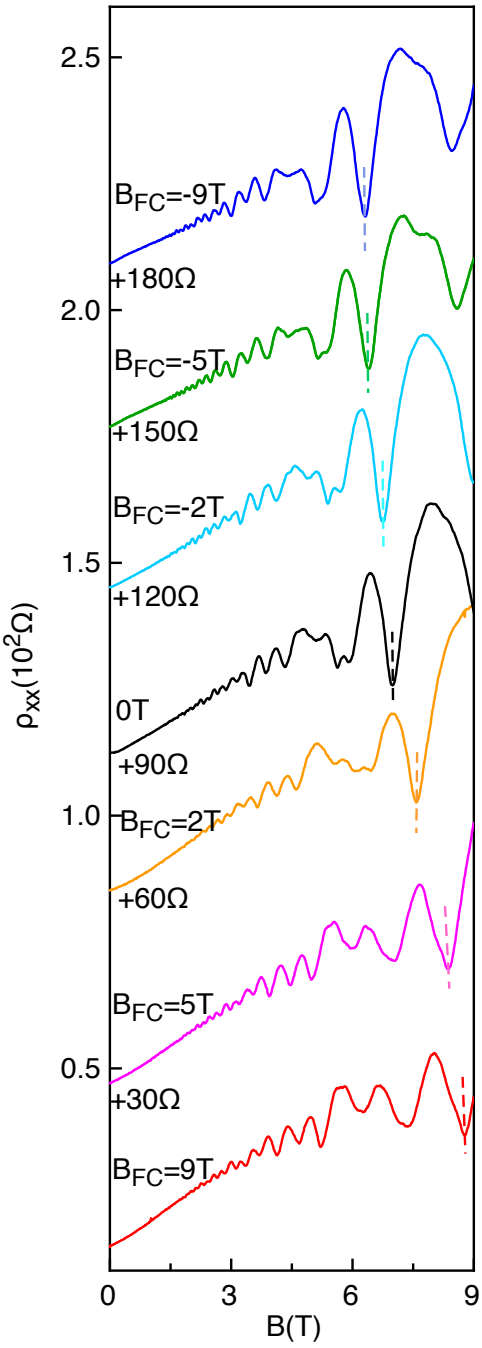


Figure 2.9. Magnetoresistivity of monolayer graphene/CrSe sample under different field coolings. The same dip as denoted by the dashed are shifted by the field coolings, where the positive field cooling shifts the quantum oscillations rightwards and negative one shifts the oscillations leftwards.

is comparable to the Hall resistivity of the heterostructure ρ_{xy}, the Landau level index is difficult to be extracted by directly treating two conductive channels in parallel: one resistivity is from CrSe

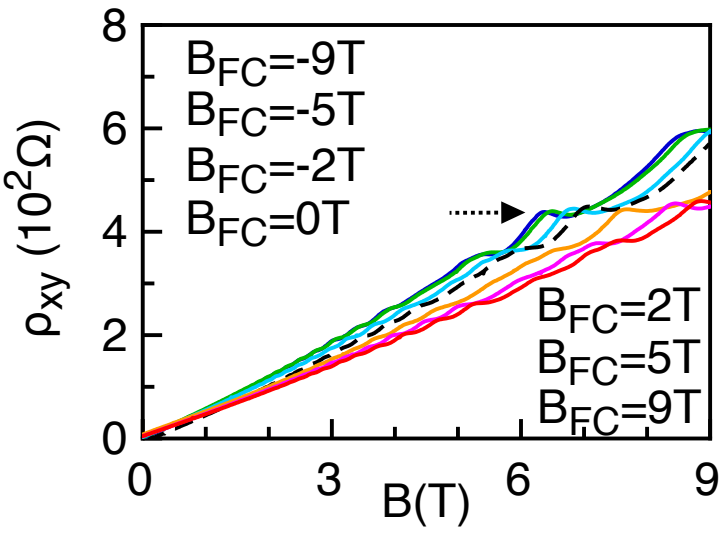


Figure 2.10. Hall resistivity of monolayer graphene/CrSe sample under different field coolings. The quantum Hall plateau is shifted with respect to the field cooling.

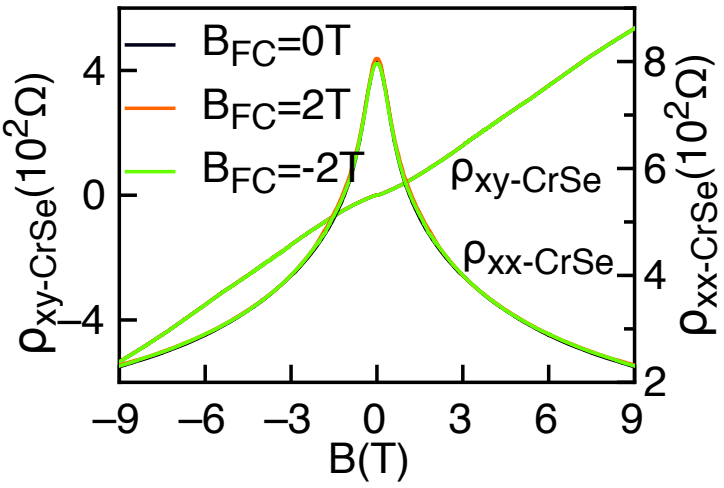


Figure 2.11. Hall resistivity and magnetoresistivity of 30 nm-thick CrSe/GaAs at 2K show little dependence on field coolings. This helps exclude the possibility that the shift of the quantum oscillations in the heterostructure is from CrSe.

and the other one is from graphene since direct subtractions yield divergent values sometimes. The quantum Hall plateaus of the graphene layer are thereby buried in the background associated with the CrSe layer, resulting in a set of 'kinks', significantly deviated from the expected multiples of $\frac{h}{e^2}$. Later, a novel way to determine the Landau level index through the quantum oscillations by machine learning will be discussed.

As mentioned before, the negative field coolings shift the quantum oscillations to a smaller magnetic field direction while the positive ones shift to the opposite direction. In Fig. 2.10, the Hall signal can be shifted to opposite directions after positive and negative field cooling. That is, each quantum-Hall 'kink' also shifts its position but keeping at the same height for all Hall measurements after different field coolings. The shifts in the SdH minima in ρ_{xx} as shown in Fig. 2.9 are precisely synchronised with the corresponding shifts in the kink locations of as shown in Fig. 2.10. The field-cooling dependent positions of the ρ_{xx} minima identified by the dashed line in Fig. 2.9 and the kink identified by the arrow in Fig. 2.10 are plotted together in Fig. 2.12 to highlight the similar trend.

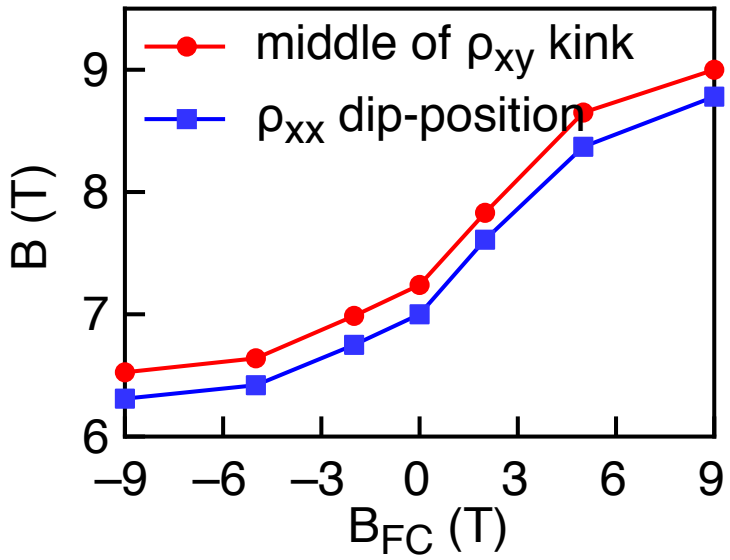


Figure 2.12. For the quantum oscillations dip indicated by the arrow in Fig. 2.9 and quantum Hall plateau indicated by the dashed arrow in Fig. 2.10, which have the same Laudau level index, the red filled circles are for the magnetic fields at the middle of the quantum Hall plateaus and the blue squares are for the magnetic fields at the dips of the quantum oscillations.

Another signature observed under the field coolings is the phase transition occurred in the temperature dependent of ρ_{xx}. Fig. 2.13 shows the longitudinal resistivity ρ_{xx} during a cooling-warm cycle for the graphene/CrSe heterostructure within a temperature range of 10 K to 300 K

(from above to far below the Néel temperature). First an out-of-plane field of 2 T was applied during the cooling down from 300 K to 2 K and then no magnetic field was applied during the temperature warming up. The longitudinal resistivity ρ_{xx} shows a peak and a dip for the cooling and warming processes, respectively. These two signatures both present at approximately 265 K which is about 8 K lower than the Néel temperature from the neutron diffraction measurements. This indicates the carrier transport in the heterostructure is indeed affected by the magnetic orders.

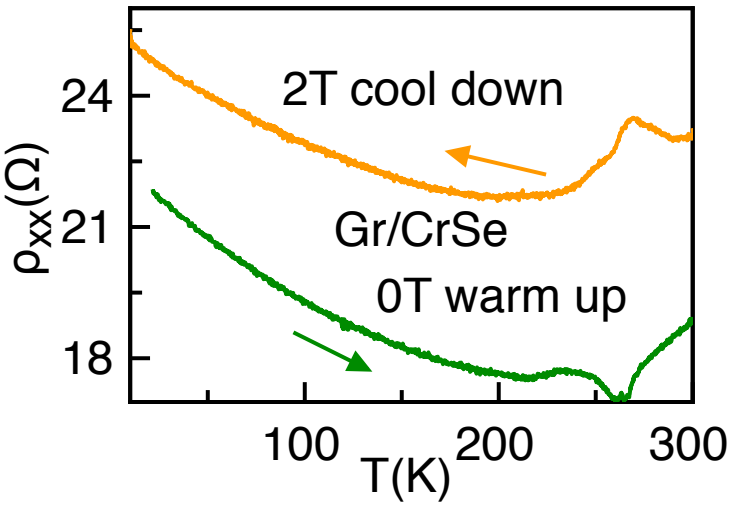


Figure 2.13. Magnetic phase transition revealed by the kink around 265K (which is 8K lower than the Néel temperature) both at 2T FC cool down followed by the 0T warm up.

2.2.2 Super-paramagnetism from MOKE measurements

The field cooling can help pin the surface magnetic moments of CrSe with the external magnetic field, and this results in a net magnetic moment frozen out of plane. The Cr-d orbitals of these frozen moments overlap with the p orbitals on the adjacent carbon atoms, inducing a spin splitting energy Δ. As shown in the transport measurements, this spin splitting energy Δ can be modulated through the field coolings. In this case, the proximity effect induced orbital hybridizations can

help magnetize the graphene layer. Thus MOKE measurements were used to directly investigate the magnetism in this heterostructure since CrSe alone, as an antiferromagnet, will not contribute any net magnetization theoretically.

The MOKE set-up[75] is schematically shown in Fig. 2.14. The system begins with a He-Ne CW laser centered at 633 nm as its light source as shown in the right part. The laser beam is then intensity-modulated at $\sim$ 100 KHz using a photo-elastic modulator (PEM) and polarized linearly. The following half-wave plate (HWP1) is used to adjust the polarization plane with respect to the sample orientation, with half of the laser power sending into a power meter by a 50/50 beam splitter. Then the laser passes through a second half-wave plate (HWP2) of which the principal axis is carefully aligned with the polarization plane of the laser. The polarization plane shown in the upper part of the reflected light is therefore rotated by $-\theta_K$ away from the initial polarization plane after passing through HWP2 the second time. An objective with an amplification of 20X is used to focus the laser beam into the a micrometer-size spot on the sample surface and carefully aligned to ensure the normal incidence. For the low temperature measurements, the sample is mounted in a JANIS ST-100 optical cryostat for cooling. The reflected beam is sequentially passed through a half-wave plane (HWP3) and a Wollaston prism. The Wollaston prism is used to separate the s-component and p-component of the laser, and HWP3 is used to initially set these two components equal when no magnetic surface is presented. Consequently, the resultant non-zero θ_K is reflected in the difference between the s-component and p-component for a magnetic sample, which can be captured by the balanced photodetector. Due to the intensity modulation of the laser, the output voltage from the photodetector is fed into a lock-in amplifier with the reference frequency locked to the PEM at 100 KHz to extract the relative value of Kerr rotation θ_K.

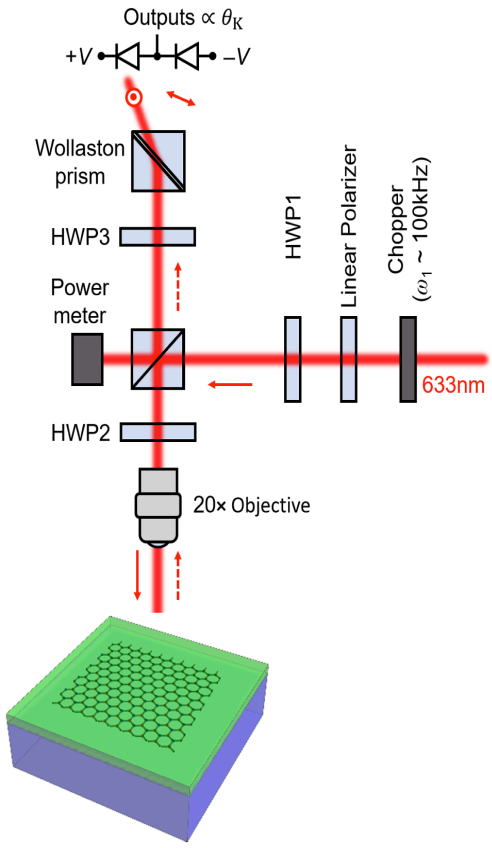


Figure 2.14. The experimental set-up for the magneto-optic Kerr effect measurement. The system begins with a He-Ne CW laser centered at 633 nm. The laser beam is then intensity-modulated at $\sim$ 100 KHz using a photo-elastic modulator and polarized linearly.

In our case, a beam of the linearly polarized laser consisting of 633 nm HeNe with a power of 50 mW was incident along the surface normal of the graphene/CrSe heterostructure. During a scan of the out-of-plane magnetic field, any magnetization pinned by the fields should result in a detectable Kerr rotation of the polarization direction. This experiment was carried out at temperatures both above and far below the Néel temperature of CrSe (300 K and 12 K).

The Kerr rotation for the heterostructure and a control sample consisting of pristine CrSe are shown in Fig. 2.15 in the up and low panels, respectively. At 12 K, a sizeable Kerr rotation was detected as a function of the external magnetic field. The rotation angle indicates a super-paramagnetic behavior for the graphene/CrSe heterostructure, suggesting a detected out-of-plane

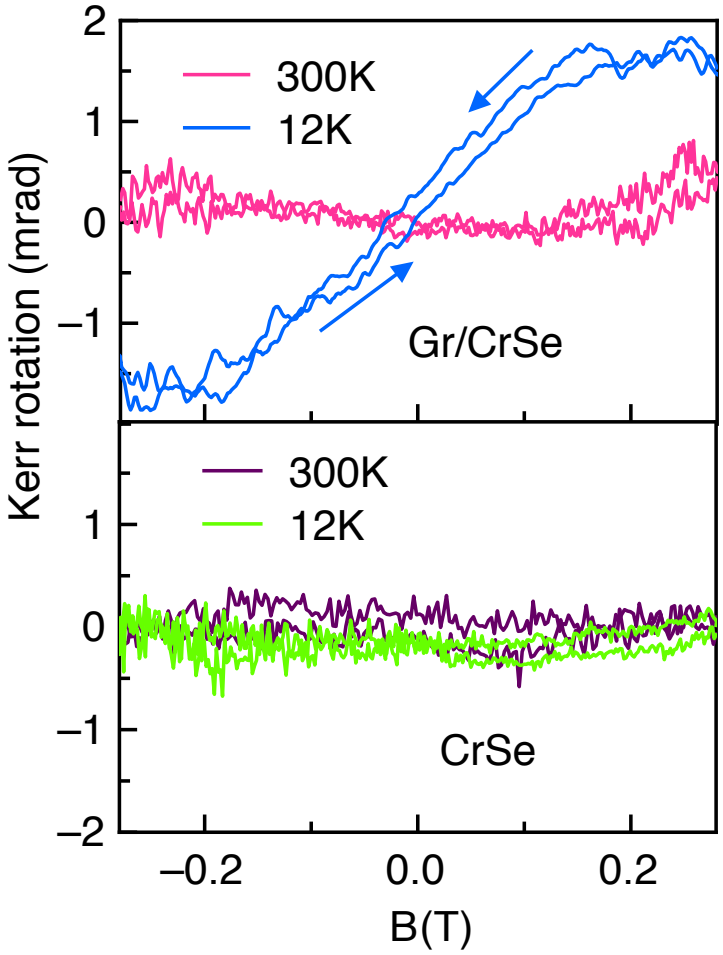


Figure 2.15. MOKE measurements of the graphene-on-CrSe sample and a control sample. The Kerr rotation of graphene-on-CrSe shows the magnetized graphene at 12 K and no magnetic signal at room temperature. The graph below shows the Kerr signal for CrSe on the same substrate. The arrows indicate the magnetic field sweeping direction.

component of the magnetization when an out-of-plane field is applied. This is absent in the control sample at the sample temperature. When the temperature is raised up to 300 K, no detectable Kerr rotation has been observed in both samples since the Néel order in CrSe is destroyed by the thermal fluctuations.

Further, the comparison between the anomalous Hal effect at 2 K after -5 T field cooling and the low-temperature MOKE data is shown in Fig. 2.16. The Kerr rotation angle saturates at $\sim \pm 0.25$ T, this is consistent with the Hall resistivity curve. Both curves suggest a net magnetization induced

into the heterostructure from the orbital hybridization at the graphene/CrSe interface.

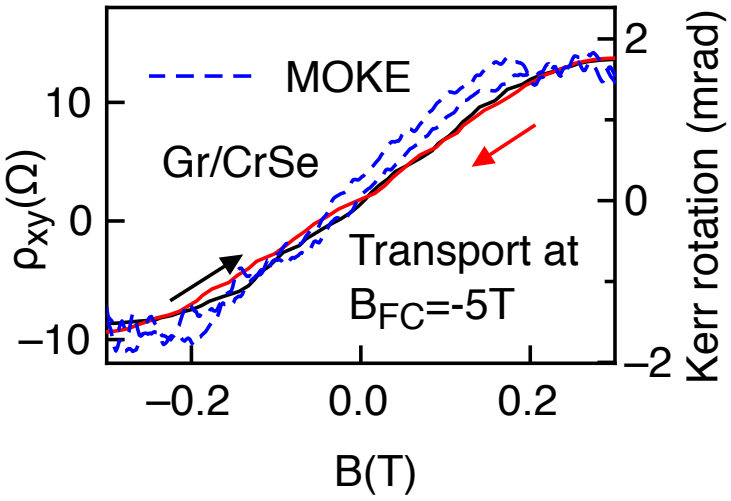


Figure 2.16. Comparison between MOKE data at 12 K and transport data at 2 K for graphene/CrSe heterostructure. It shows a good consistency between MOKE and transport data.

2.3 Landau level fitting using machine learning

As mentioned before, the transport signal from the heterostructure consists of two channels: one is from the CrSe thin film and the other one is from the graphene. Due to the comparable scale of the Hall resistivity for the control pristine CrSe and the graphene/CrSe heterostructure, it is impossible to get the precise values of graphene resistivity when simply treating the system as a parallel circuit. Thus, for the first time, a precise way was reported to determine the Landau level index in graphene by taking advantage of the emergent new field: machine learning. Simply speaking, the determination of Landau level index is done by optimally fitting the Landau fan diagram.

2.3.1 Landau level considering the spin-splitting term

Here the exchange splitting induces a rigid shift in the Landau-level spectrum. Starting with the low-excitation Hamiltonian, the spin splitting is included as:

$$\mathbf{H} = v_F \mathbf{p} \cdot \boldsymbol{\sigma} + \frac{\Delta}{2} \boldsymbol{s}_z. \tag{2.1}$$

Note that $\boldsymbol{\sigma}$ denotes the Pauli matrices for pseudospin, and $\mathbf{s}$ are the Pauli matrices for electron spin. In the case that the CrSe surface is not atomically sharp although the valley symmetry should be broken locally, and such asymmetry should be averaged out globally. Therefore the valley degree of freedom is ignored. Using the Peierls substitution, the wave vector is replaced by the gauge-invariant kinetic momentum, $\mathbf{p} \rightarrow \frac{\mathbf{\Pi}}{\hbar} = -i\nabla + \frac{e}{\hbar}\mathbf{A}(\mathbf{r})$, where $\mathbf{A}(\mathbf{r})$ is the vector potential: $B\mathbf{e}_z = \nabla \times \mathbf{A}$. Using commutation relation $[x_\mu, p_\nu] = i\hbar\delta_{\mu\nu}$ and $p_\mu = -i\hbar\frac{\partial}{\partial x_\mu}$ $(\mu, \nu = x, y)$, it leads to

$$[\Pi_x, \Pi_y] = -i\frac{\hbar^2}{l_B^2} \tag{2.2}$$

where $l_B = \sqrt{\frac{\hbar}{eB}}$ is the characteristic magnetic length. Using ladder operators

$$a = \frac{l_B}{\sqrt{2}\hbar}(\Pi_x - i\Pi_y) \tag{2.3}$$

$$a^\dagger = \frac{l_B}{\sqrt{2}\hbar}(\Pi_x + i\Pi_y) \tag{2.4}$$

The Hamiltonian now becomes

$$H = \begin{bmatrix} h_\uparrow & 0 \\ 0 & h_\downarrow \end{bmatrix} \tag{2.5}$$

where

$$h_{\uparrow,\downarrow} = \frac{\sqrt{2}\hbar v_F}{l_B} \begin{bmatrix} 0 & a \\ a^\dagger & 0 \end{bmatrix} + \begin{bmatrix} \pm\frac{\Delta}{2} & 0 \\ 0 & \pm\frac{\Delta}{2} \end{bmatrix}. \tag{2.6}$$

Here $\uparrow$ and $\downarrow$ correspond to $+$ and $-$, respectively. Denoting the wave function by $\Psi = (\Psi_\uparrow, \Psi_\downarrow)^T = (\Psi_A^\uparrow, \Psi_B^\uparrow, \Psi_A^\downarrow, \Psi_B^\downarrow)^T$, one can solve the Schrödinger equation for each spin: $h_{\uparrow,\downarrow}\Psi_{\uparrow,\downarrow} = \epsilon\Psi_{\uparrow,\downarrow}$:

$$\frac{\sqrt{2}\hbar v_F}{l_B} \begin{bmatrix} 0 & a \\ a^\dagger & 0 \end{bmatrix} \begin{bmatrix} \Psi_A^{\uparrow,\downarrow} \\ \Psi_B^{\uparrow,\downarrow} \end{bmatrix} = \left(\epsilon \mp \frac{\Delta}{2}\right) \begin{pmatrix} \Psi_A^{\uparrow,\downarrow} \\ \Psi_B^{\uparrow,\downarrow} \end{pmatrix} \tag{2.7}$$

Writing out the two rows in Eq. 2.7, it leads to

$$\begin{cases} \frac{\sqrt{2}\hbar v_F}{l_B} a\Psi_B^{\uparrow,\downarrow} & = \left(\epsilon \mp \frac{\Delta}{2}\right) \Psi_A^{\uparrow,\downarrow} \\ \frac{\sqrt{2}\hbar v_F}{l_B} a^\dagger\Psi_A^{\uparrow,\downarrow} & = \left(\epsilon \mp \frac{\Delta}{2}\right) \Psi_B^{\uparrow,\downarrow} \end{cases}. \tag{2.8}$$

Substituting Ψ_A in the second row of Eq. 2.8 using the first row, it leads to

$$a^\dagger a\Psi_B^{\uparrow,\downarrow} = \left(l_B \frac{\epsilon \mp \frac{\Delta}{2}}{\sqrt{2}\hbar v_F}\right)^2 \Psi_B^{\uparrow,\downarrow}. \tag{2.9}$$

This suggests that the squared term on the right side of Eq. 2.9 is the eigenvalue of the number operator: $a^\dagger a \left|n\right\rangle = n \left|n\right\rangle$. Therefore the Landau levels are:

$$\epsilon_n^{\uparrow,\downarrow} = \frac{\hbar v_F}{l_B}\sqrt{2\left|n\right|} \pm \frac{\Delta}{2}. \tag{2.10}$$

Here $n = 0, \pm1, \pm2, \pm3\cdots$, and $\frac{\Delta}{2}$ is a rigid shift of the spectrum.

2.3.2 Slope of the Landau fan diagram

The position of the Fermi level ϵ_{F} and the spin-splitting energy Δ can be quantitatively extracted using the Landau fan diagram. In the quantum oscillations, each dip of the ρ_{xx} corresponds to a crossing between one Landau level and ϵ_{F}. These dips thus result in a set of filling factors $\{\nu\}$, which satisfy $\sigma_{xy} = \nu\frac{e^2}{h}$. Here, $\nu = \pm 4(n \pm \frac{1}{2})$ for $\epsilon_F \gtrless 0$, respectively[3, 76]. Each quantized σ_{xy} and the corresponding quantum oscillations dip can be identified with one integer value of $n = 0, 1, 2, \cdots$, which counts the Landau levels that can intersect ϵ_F due to the band-bending. Particularly, the floor (ceiling) function $\lfloor \cdots \rfloor$ ($\lceil \cdots \rceil$) is adopted to take the integer value of the n: $n = \lfloor \frac{\epsilon_F^2}{\alpha}\frac{1}{B} \rfloor$ for $\epsilon_F > 0$ and $n = \lceil \frac{\epsilon_F^2}{\alpha}\frac{1}{B} \rceil$ for $\epsilon_F < 0$ with $\alpha = 2e\hbar v_F^2$. Here the floor function chooses the greatest integer that is less than or equal to the $\frac{\epsilon_F^2}{\alpha}\frac{1}{B}$ and the ceiling function chooses the least integer that is greater than or equal to the $\frac{\epsilon_F^2}{\alpha}\frac{1}{B}$. By taking the integer values of n, a linear relation between n and $\frac{1}{B}$ can be obtained. As proved experimentally before[3], the discrete set of $\{n\}$ precisely aligns linearly on a fan of lines $n = \pm\frac{\epsilon_F^2}{\alpha B} \pm \frac{1}{2}$, with the slopes $\beta = \frac{\epsilon_F^2}{\alpha}$ dependent on the position of the Fermi level ϵ_F. In this case, $\pm\frac{1}{2}$ term originates from the 0th Landau level, where only 2 out of 4 degenerate states can intersect ϵ_F.

When graphene is magnetized by a sizeable spin-splitting energy, the low-energy Hamiltonian of graphene includes an additional spin-splitting term and becomes $H = \hbar v_F \mathbf{k} \cdot \boldsymbol{\sigma} + \frac{\Delta}{2}\mathbf{s}_z$. The valley degree of freedom is not resolved here since the atomic alignment at the interface cannot be precisely controlled and the valley splitting should be easily averaged out. Considering the spin splitting, the originally degenerate Landau levels now split into two sets, $n^{\uparrow}$ and $n^{\downarrow}$. The filling factor now is $\nu = 2(n^{\uparrow} + n^{\downarrow})$ for $-|\frac{\Delta}{2}| \leq \epsilon_F \leq |\frac{\Delta}{2}|$, where $n^{\uparrow} = \lceil -(\epsilon_F - |\frac{\Delta}{2}|)^2\frac{1}{\alpha B} \rceil$ and

$n^{\downarrow} = \lfloor (\epsilon_F + |\frac{\Delta}{2}|)^2 \frac{1}{\alpha B} \rfloor$. When the Fermi level is outside the spin-splitting region ($\epsilon_F \gtrless \pm|\frac{\Delta}{2}|$), the filling factor becomes $\nu = \pm 2(n^{\uparrow} + n^{\downarrow} \pm 1)$, respectively. Here, ± 1 inside the bracket is due to the 0th Landau level, $n^{\uparrow,\downarrow} = \lceil -(\epsilon_F \pm |\frac{\Delta}{2}|)^2 \frac{1}{\alpha B} \rceil$ for $\epsilon_F < -|\frac{\Delta}{2}|$ and $n^{\uparrow,\downarrow} = \lfloor (\epsilon_F \mp |\frac{\Delta}{2}|)^2 \frac{1}{\alpha B} \rfloor$ for $\epsilon_F > |\frac{\Delta}{2}|$. Similar to the spin-degenerate case, one can approximate the slope of the Landau fan diagram using a smooth function when removing the floor and ceiling brackets:

$$\beta = \begin{cases} -\frac{2}{\alpha}\left(\epsilon_F^2 + \frac{\Delta^2}{4}\right), & \epsilon_F < -\left|\frac{\Delta}{2}\right| \\ \frac{2|\Delta|\epsilon_F}{\alpha}, & |\epsilon_F| \leqslant \left|\frac{\Delta}{2}\right| \\ \frac{2}{\alpha}\left(\epsilon_F^2 + \frac{\Delta^2}{4}\right), & \epsilon_F > \left|\frac{\Delta}{2}\right| \end{cases} . \tag{2.11}$$

After removing the floor and ceiling brackets, the value of β now becomes continuous rather than discrete. In this approximation, the total slope of the Landau fan diagram is considered as a simple sum of the up-spin and down-spin slopes and ignores the sudden changes of the total filling factor due to the Landau-level crossing between the down- and up-spin states.

2.3.3 Extraction of spin-splitting energy using the machine learning

This spin-splitting energy Δ can be modulated by the field cooling in the graphene/CrSe heterostructure. Phenomenologically, one can assume Δ will saturate at large enough cooling fields,

$$\Delta(B_{FC}) = \Delta_0 + \Delta_1 \tanh(\xi B_{FC}), \tag{2.12}$$

where Δ_0 is the spin-splitting energy at zero cooling field ($B_{FC} = 0$), Δ_1 shows the magnitude of the modulation and ξ is the fitting parameter. With an odd function $\tanh x$, the positive and negative

field cooling can shift the up- and down-spin bands in opposite directions as schematically shown in Fig. 2.17. Accordingly, the slope of the Landau fan diagram is modified based on Equation 2.11.

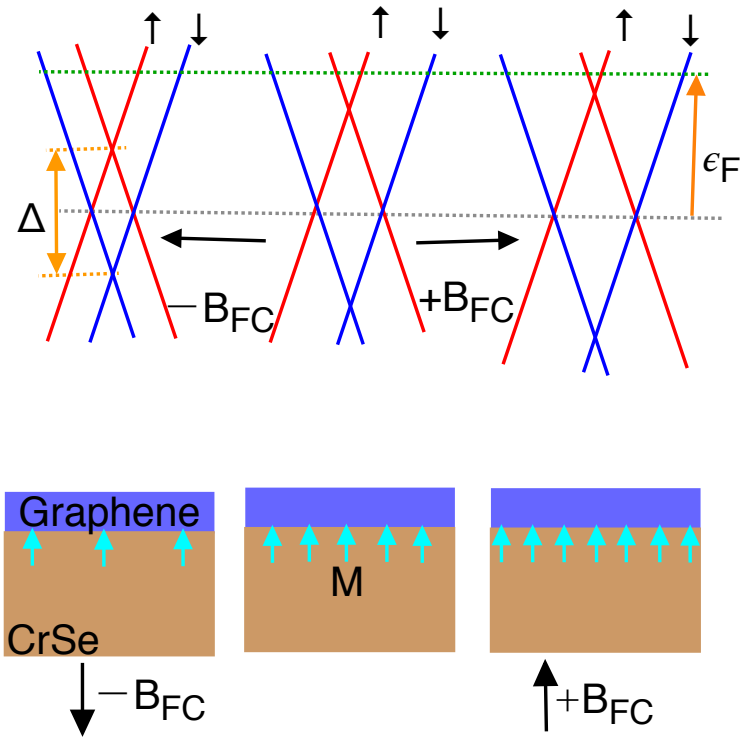


Figure 2.17. The schematic view for graphene coupled to antiferromagnetic CrSe thin films. The red and blue lines represent the linear dispersion near the Dirac points corresponding to the up and down electron spins, respectively. The negative (- B_{FC}) and positive (+ B_{FC}) field coolings decrease and increase the exchange splitting energy Δ, respectively. The blue arrows in the lower panels represent the remanence magnetization induced at the interface.

To accurately determine the slope of the Landau fan diagram, re-plot Fig. 2.9 and changes of the x-axis to the coordinate of $\frac{1}{B}$ were shown in Fig. 2.18. The dips in the quantum oscillations are equally distributed, similar to the spectrum of graphene.

Each dip of the magnetoresistivity ρ_{xx} corresponds to an integer change in $n = n^{\uparrow} + n^{\downarrow}$, thus the slopes of the Landau fan can be obtained by the period of the quantum oscillation dips. These experimentally determined slopes are shown by the data points in Fig. 2.19, which are

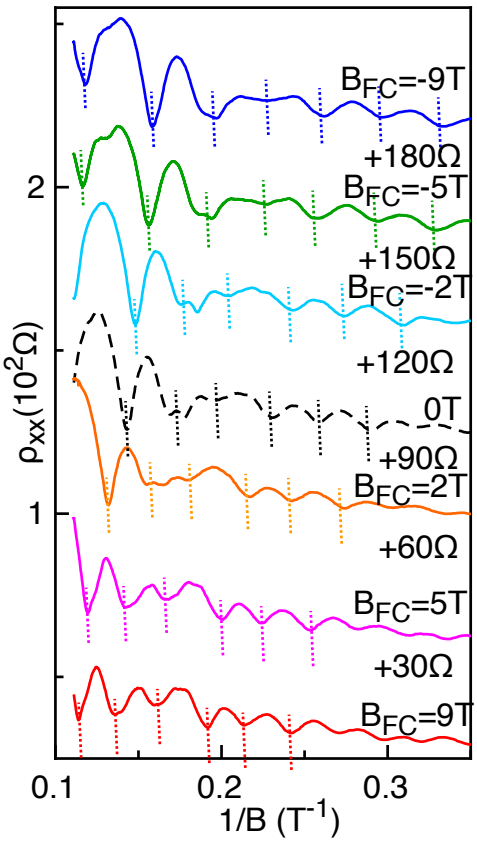


Figure 2.18. The dependence of longitudinal resistivity on the inverse of magnetic fields shows the equally spaced periods of the oscillations under different field coolings. Quantum oscillations are shifted by the field cooling.

corresponding to different field coolings ranging from -9 T to 9 T.

With these values, the parameter set $\mathbf{X} = \{\epsilon_F, \Delta_0, \Delta_1, \xi\}^T$ living in $\mathbb{R}^4$ becomes over-determined and therefore be extracted by searching for the optimal $\mathbf{X}$ than can minimize the overall fitting error. This can be achieved by solving a standard machine learning problem. The average error of the fitting is defined as:

$$\phi(\mathbf{X}) = \frac{\Sigma_i[\beta(B^i_{FC}, \mathbf{X}) - \hat{\beta}(B^i_{FC})]^2}{\Sigma_i \hat{\beta}^2(B^i_{FC})}, \tag{2.13}$$

where $\beta(B^i_{FC}, \mathbf{X})$ is the theoretical Landau fan slope given a parameter set of $\mathbf{X}$. The hat in $\hat{\beta}(B^i_{FC})$ denotes the experimental values. The machine learning process is the search for the parameter set

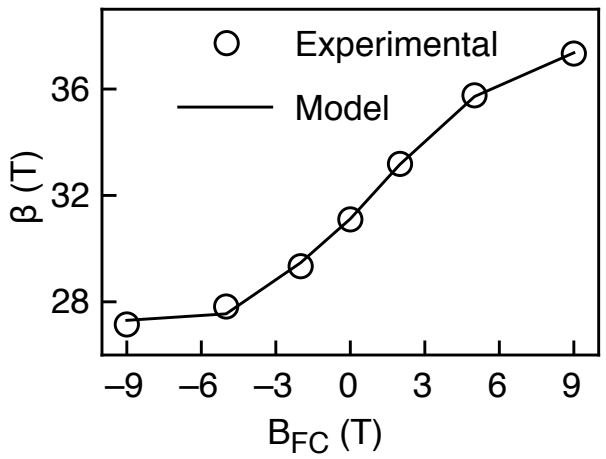


Figure 2.19. The slope of the Landau fan diagram dependence on the field coolings from the experiment and fitting using machine learning. It shows a perfect match between the experimental and model values.

$\mathbf{X}$ in $\mathbb{R}^4$ that can minimize $\phi(\mathbf{X})$, i.e. $\mathbf{X}_0 := \arg\min_{\mathbf{X}}\phi(\mathbf{X})$. The searching direction of step $i+1$ is given by conjugate gradient regression:

$$\mathbf{d}_{i+1} := -\nabla\phi_{i+1} + \alpha_i \mathbf{d}_i, \tag{2.14}$$

here

$$\alpha_i := \frac{\nabla\phi_{i+1}\cdot(\nabla\phi_{i+1} - \nabla\phi_i)}{\mathbf{d}_i\cdot(\nabla\phi_{i+1} - \nabla\phi_i)}. \tag{2.15}$$

After getting values of $\mathbf{d}_{i+1}$, a one-dimensional golden section line search is carried out to find $\mathbf{X}_{i+1}$:

$$\mathbf{X}_{i+1} := \mathbf{X}_i + \gamma_i \mathbf{d}_{i+1}, \tag{2.16}$$

here

$$\gamma_i := \arg\min_{\gamma}\phi(\mathbf{X}_i + \gamma\mathbf{d}_{i+1}). \tag{2.17}$$

Equation 2.15 is known as the Polak-Ribière method established in 1969[77]. The gold-sectional

line search was originally introduced by Kiefer in 1953[78]. This learning algorithm eventually gave a stable local minimal of ϕ, which is smaller than 2×10^{-5}. The extracted parameters are: $\epsilon_F = 142.4$meV, $\Delta_0 = 134.4$meV, $\Delta_1 = 65.03$meV and $\xi = 0.1834\text{T}^{-1}$.

This learning result is over-determined because perturbing the initial points of $\mathbf{X}$ does not change the converged value of $\mathbf{X}_0$ as shown in Fig. 2.20. All four panels show the convergence route of each parameter when they start from different initial points. This learning algorithm converges all of them to the same value in $\mathbf{X}_0$ as denoted by the dashed lines.

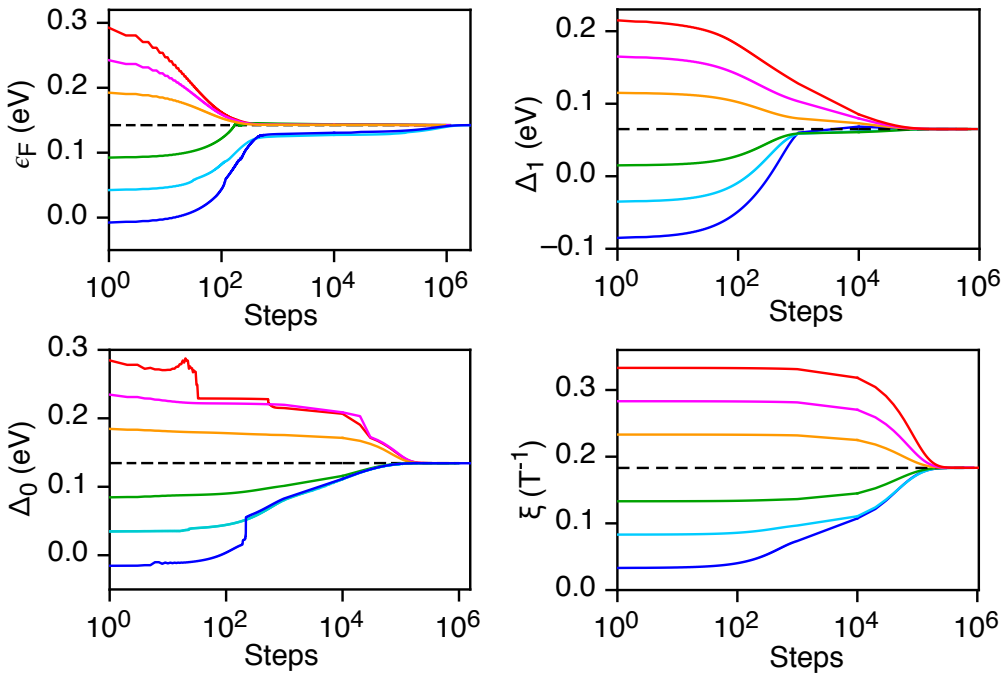


Figure 2.20. The stability check for the learning algorithm. Either one of the four parameters converges into a constant when the steps are large enough.

The position of Fermi level ϵ_F suggests an unintentional doping with a carrier density around 10^{12} cm^{-2}, which is likely induced by the work-function misalignment at the interface. Such level of doping is shown in monolayer graphene exfoliated on SiO_2/Si substrate before[79]. Once ϵ_F is determined, the values of the spin splitting energy $\Delta(B_{FC})$ can be obtained using Equation 2.11

using the experimental values of the slope $\beta(B_{FC})$, called experimental values as shown in the Fig. 2.21. Another set of the spin splitting energy can be obtained using the phenomenological model based on the Equation 2.12 as indicated by the circles. These two sets of the spin splitting energy shows perfect self-consistency.

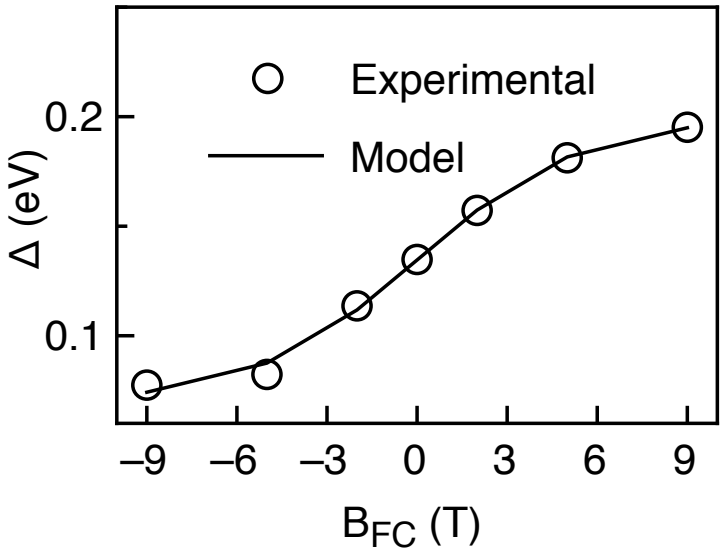


Figure 2.21. The spin splitting energy dependence on the field coolings from experiment and fitting using machine learning. It shows a perfect match between experimental and model values.

Next, the parameters determined by the machine learning ware used to show they perfectly fit the Landau fan diagram through determining the Landau level indices corresponding to each dip in the quantum oscillations. After getting the Landau fan slopes from the quantum oscillation dips, the Landau level indices were extracted by assigning consecutive integers to each quantum oscillation dip. These values could be checked whether to follow the expected straight lines in the $n - \frac{1}{B}$ plot. Since $n = 0$ has to be satisfied at $\frac{1}{B} \to 0$, there is only one way to assign the integer values of $n = n^{\uparrow} + n^{\downarrow}$ to the quantum oscillation dips. By letting $n = 3$ at $B = 9$ T, the fitting demonstrates a perfect match as shown in Fig. 2.22. With these values, the experimental Landau

fan then can be compared to the one given by the model. The modulations of the Landau fan slope by the field coolings are clear.

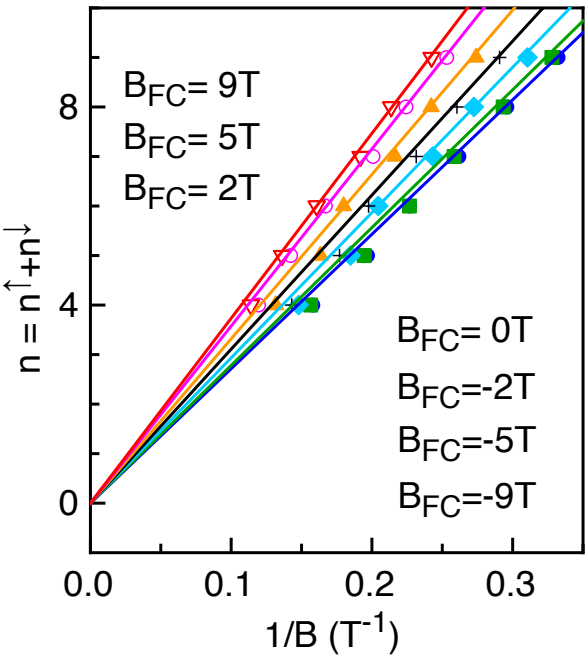


Figure 2.22. Landau level indices extracted in the Landau fan diagram for different field coolings, where the dots are the experimental values and the lines are from calculations using parameters given by machine learning.

To illustrate the uniqueness of the fitting for the Landau fan diagram, the same fitting by changing $n \rightarrow n \pm 1$ has been shown in Fig. 2.23. Obviously, these sets of indices fail to coincide with the calculated n dependence on $\frac{1}{B}$ since the experimental points deviate from the linear fitting lines for different field coolings.

2.3.4 Discussion of the fitting results

The above analysis attributes the slope modulation in the Landau fan diagram to the spin splitting energy Δ only, while assuming the Fermi level ϵ_F to be fixed during the field coolings. The position of ϵ_F is usually a result of the work-function misalignment at the interface. To evaluate

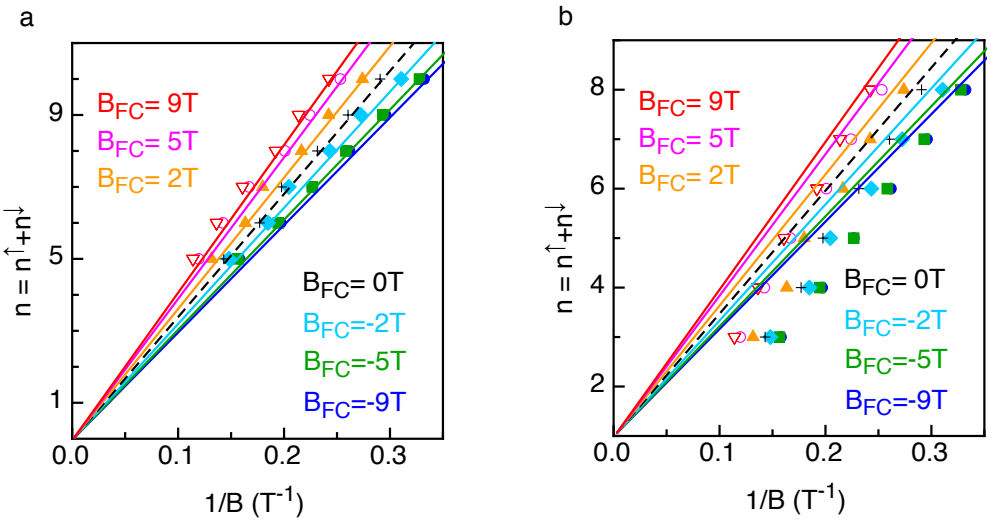


Figure 2.23. Assigning the Landau-level indices by letting $n \to n-1$ (a) and $n \to n+1$ (b). The expected fan diagrams are shown by the lines in both panels. These two fittings do not match the data.

how the ϵ_F is changed during the field coolings, further extraction of the carrier activation energy was done in the control pristine 30 nm-thick CrSe thin film through the $R-T$ relation.

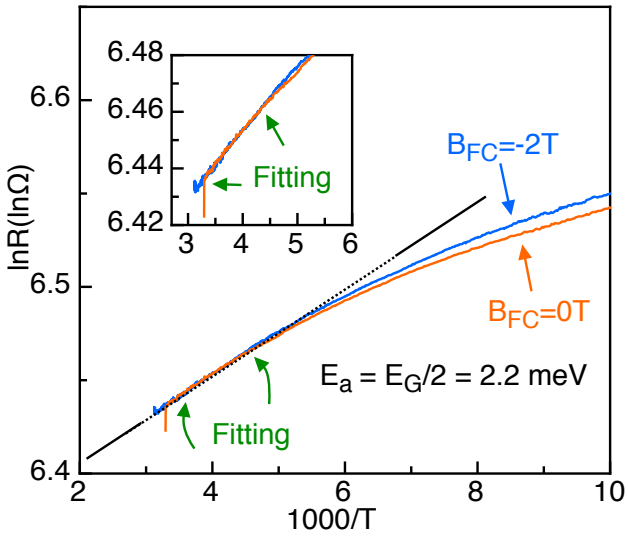


Figure 2.24. Same activation energy for 30 nm-thick CrSe extracted from R-T curves. Solid lines are experimental values and dashed lines are the linear fitting curves. Inset shows the zoom-in fitting at high temperature region.

The change of the ϵ_F should originate from a change in the interfacial band alignment, which can be captured by the carrier activation energy ϵ_a. Using Arrhenius law $R \propto exp(\epsilon_a/k_BT)$ which

has been widely adopted, one can take the x axis as $1000/T$ and y axis as $\ln R$, then the slope of the high-temperature linear $R-T$ curve provides an estimation of ϵ_a. The fitting range is below T_N and above 200 K. By fitting in this range where all carriers are fully excited by a wide enough thermal window while the magnetic order is well preserved, ϵ_a is estimated to be 2.2 meV in Fig. 2.24. The fitting values of ϵ_a is further reduced in the fitting window with lower temperatures. Although the field cooling B_{FC} =-2 T does change the slope at lower temperatures, the extracted values would be much smaller than the estimated Δ, and still cannot dominate to modulate the total carrier density. Therefore, it is reasonable to attribute the field cooling effect only to the Δ term in the Hamiltonian.

The extracted spin splitting energy is $\Delta(B_{\mathrm{FC}}) = 134.4\,\mathrm{meV} + 65.03\,\mathrm{meV}\tanh(0.1834\,\mathrm{T}^{-1}B_{\mathrm{FC}})$, ranging from 69.37 meV to 199.43 meV adjustable due to field cooling. This spin splitting energy is induced by the hybridization between the π orbital of the carbon atoms and the d orbitals in the Cr atoms. Previously, DFT calculations have shown that such energy can be as large as 150 meV in a graphene/CrI_3 heterostructure[80], which is within the same order of magnitude of the spin splitting energy in our experiment.

On the other side, spin-orbit coupling is also known to modify the transport properties. Such spin-orbit coupling has been demonstrated in graphene/TMDs heterostructures by analyzing the transition from weak localization to weak antilocalization[81]. By coupling graphene to TMDs containing heavy elements like tungsten, the spin-orbit coupling energy is extracted by using an explicit theoretical expression for the magnetoconductivity due to weak antilocalization[82] and estimated to be within 15 meV. In our case, Cr atoms are lighter than tunsten atoms, a weaker spin-

orbit coupling is expected in our graphene/CrSe heterostructure. Thus the spin splitting energy greater than the spin-orbit coupling strength by at least one order of magnitude, and therefore spin-orbit coupling is neglected in our analysis.

2.4 Summary of Chapter 2

In this chapter, CrSe is proved to be an antiferromagnet with a NiAs-type crystal structure and a Néel temperature of $\sim$270 K. The non-collinear antiferromagnetic spin texture in CrSe thin films can magnetize monolayer graphene through interface coupling. The spin splitting energy is identified through field-cooling measurements of the graphene/CrSe heterostructure by shifts in the quantum Hall plateau and quantum oscillations. The rigorous deduction of the Landau level considering spin splitting term and the details using machine learning to obtain the parameter sets have been shown in details. This exchange splitting energy is approximately 134 meV with a stable local minimal error smaller than 2×10^{-5}. This energy most likely represents an averaged effect, with atomic details at the interface smeared out.

The resistivity dependence on the temperature and MOKE measurements also suggest induced magnetization of graphene. Compared to the pristine CrSe, which shows zero net magnetization, the graphene/CrSe heterostructure shows super-paramagnetism at low temperature. The modulation of the graphene spectrum is shown to be controllable by the magnetic order at the interface, making it an ideal platform for both exploring quantum interface physics and developing new graphene-based spin current devices.

Chapter 3

Néel-type skyrmions in WTe_2/Fe_3GeTe_2 heterostructures

The previous chapter is about the induced magnetic order into graphene from the proximity effect. This chapter will focus on in the intrinsic magnetic order in new emerging materials, which is mentioned earlier in Section 1.5. According to the Mermin-Wagner theorem[39], in two-dimensional (2D) system, the long-range magnetic order is strongly suppressed by thermal fluctuations. However, magnetic anisotropy can counteract these thermal fluctuations and help establish the long-range magnetic order. Among all pristine vdW materials with a 2D long-range magnetic order, FGT is a robust and relatively stable ferromagnet with a high Curie temperature T_{C} of $\sim$220 K for the bulk. Monolayer FGT was successfully isolated and proved to have an out-of-plane magnetocrystalline anisotropy with a Curie temperature $\sim$ 20 K. With an ionic liquid gating, the Curie temperature for a four-layer FGT can be increased from $\sim$ 100 K to room temperature[38]. This opens up opportunities for potential applications of atomically thin vdW crystals to electronic and spintronic devices.

3.1 Transport properties of FGT

High quality single crystals of FGT were grown with a typical chemical vapor transport (CVT) method for this experiment. The stoichiometric amounts of high purity elements (99.999% Fe,

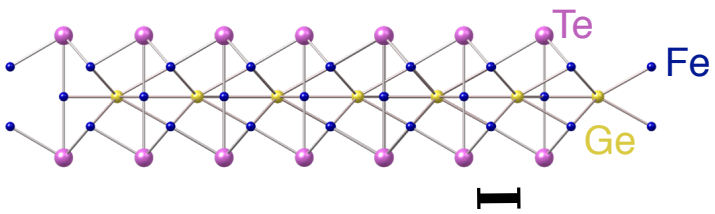


Figure 3.1. Schematic side view of the atomic lattice of monolayer FGT with a scale bar of 2 Å. Pink, blue and yellow atoms are for Te, Fe, and Ge atoms, respectively.

99.999% Ge and 99.999% Te from Alfa Aesar) along with 2 mg/cm^3 iodine as the transport agent were placed in a quartz ampoule and sealed under vacuum. The ampoule was further placed in a horizontal 2-zone furnace over a temperature gradient from 750°C to 750°C and kept at that condition for 2 weeks.

Bulk FGT consists of weakly bonded Fe_3Ge layers that alternate with two Te layers and has a space group $P6_3mmc$. The side view of a monolayer FGT is shown in Fig. 3.1. The itinerant ferromagnetism in bulk FGT results from the partially filed Fe d orbitals, which dominate the band structure around the Fermi level. The vdW gap is 2.95 Å between the adjacent monolayers in the bulk. Because of the weak vdW bonding, FGT flakes peeled from the a bulk crystal have the flake surface parallel to the Fe_3Ge layers. Bulk FGT exhibits a strong magnetocrystalline anisotropy, and this is expected to lift the restriction imposed by the Mermin-Wagner theorem. When the crystal symmetry of the layered structure is reduced, this anisotropy will help stabilize the long-range ferromagnetic order in FGT monolayers.

For FGT, one-layer (1L) thickness is 0.8 nm, which can be used to determine the number of layers for FGT when combined with the atomic force microscopy measurements as shown in Fig. 3.2. Through mechanical exfoliation, we successfully obtained FGT with different layers on 300 nm-thick SiO_2/Si substrate with a clear contrast under the microscope. Then atomic force

microscopy was used to scan the step heights for the layers.

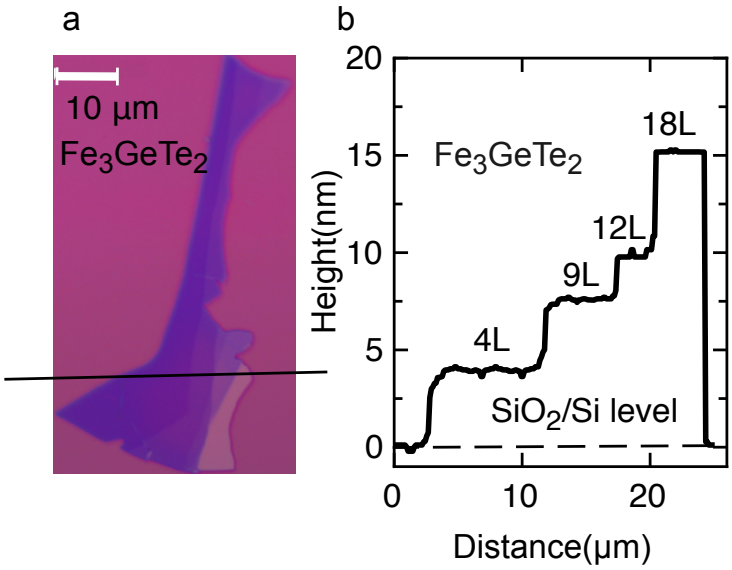


Figure 3.2. Atomic force microscopy for determining the thickness. **a**, Microscopic image of exfoliated Fe_3GeTe_2 thin films. Scale bar: 10 μm. **b**, Cross-sectional profile of the Fe_3GeTe_2 flakes along the black line shown in **a**.

For thick FGT samples, FGT layers were first exfoliated onto the SiO_2/Si substrate and then photolithography was used to make the patterns for the Hall-bar contacts since they are stable even exposed to the air. At last, a 10 nm-thick Cr followed by a 60 nm-thick Au was evaporated to make the metal contacts.

The magnetism in FGT has been probed by the Hall resistivity, ρ_{xy}, under an external magnetic field $\mu_0 H$, applied perpendicularly to the vdW plane. The Hall resistivity of 60L and 30L FGT in Fig. 3.3 has a rectangular hysteresis loops with near-vertical jumps at low temperatures as a function of the applied external magnetic field, with a coercive field reaching over 0.5 T at 5 K. This indicates the domination of the anomalous Hall effect with a single uniform magnetic domain over the entire flake. The remanent ρ_{xy} at zero field is a hallmark of ferromagnetism with strong out-of-plane anisotropy. The remanent ρ_{xy} and coercive field disappear at 220 K, indicating the

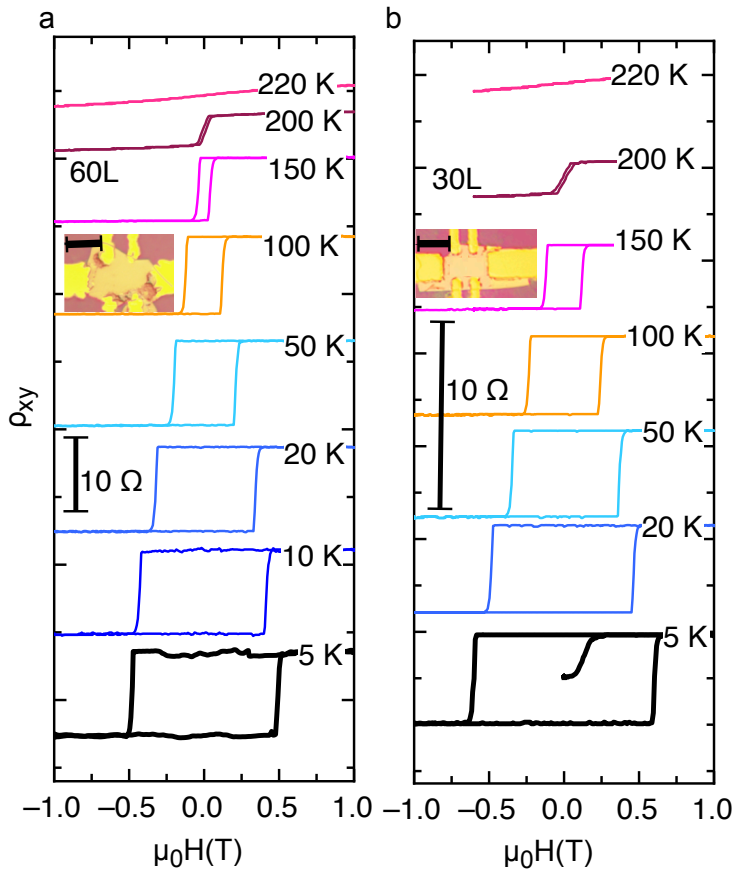


Figure 3.3. Temperature dependence of Hall resistivity for **a**, 60L and **b**, 30L Fe_3GeTe_2 flakes showing that the Curie temperature is $\sim$ 200 K for Fe_3GeTe_2 thick layers. Insets show the devices for the measurements separately and the scale bar in the inset: 10 μm. Resistivity is shifted for clarity. The vertical scale bars are 10 Ω.

Curie temperature is below this value. The Curie temperature in FGT is typically varied from 150 to 220 K, depending on the Fe concentration and deficiency[86]. In the 60L and 30L FGT, the Hall resistivity indicates a T_C of $\sim$ 200 K.

For thin FGT samples, the pick-up transfer method was adopted for the sample assembly inside the glove box, in which H_2O is about 1.2 parts per million (ppm) and O_2 is kept below 50 ppm. The bottom electrodes with a Hall bar geometry were prepared on SiO_2/Si substrates. Then PDMS/PPC was used to pick up the prepared h-BN on another SiO_2/Si substrate. By heating the sample up to 50°, h-BN was picked up to form a stack of PDMS/PPC/h-BN layers. Later, FGT was picked up

using the same approach to form the stack of PDMS/PPC/h-BN/FGT layers and then transferred onto the prepared bottom electrodes with the accurate alignment as observed under the microscope. This helps prevent FGT thin layers from the oxidization in the air conditions and the FGT layers are kept in an inertia N_2 atmosphere all the time. During sample transferring to the transport measurement, h-BN can protect the FGT from effects of the ambient conditions.

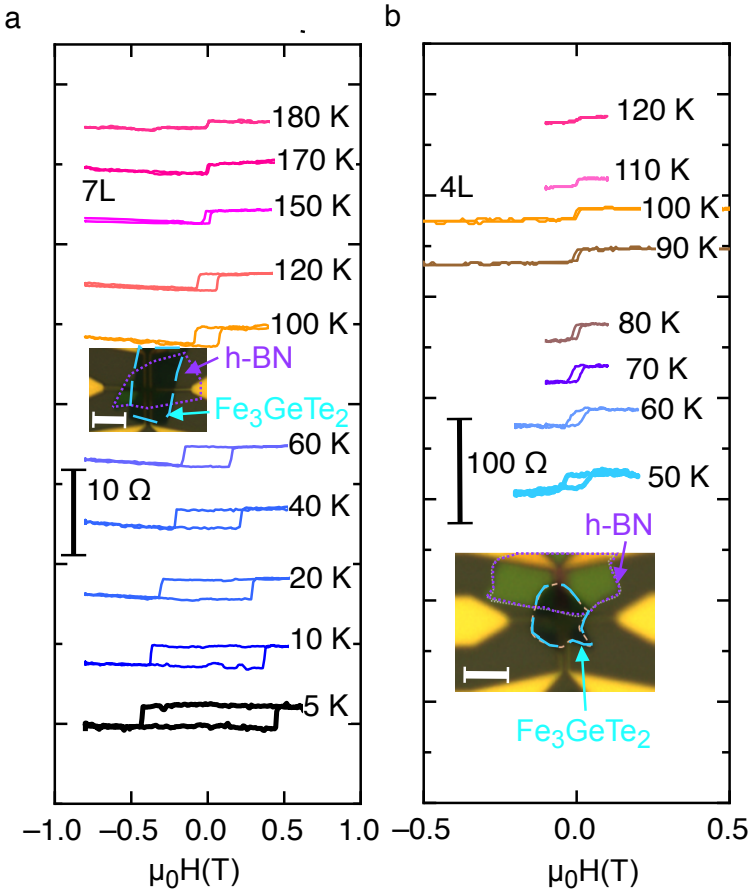


Figure 3.4. Temperature dependence of Hall resistivity for **a**, 7L and **b**, 4L Fe_3GeTe_2 flakes showing that the Curie temperature decreases when Fe_3GeTe_2 becomes thinner. Insets show the devices for the measurements and the scale bar in the inset: 10 μm. Resistivity is shifted for clarity. The vertical scale bars are 10 Ω for **a** and 100 Ω for **b**.

When the thickness of FGT is reduced down to 7L and 4L as shown in Fig. 3.4, T_C is measured to be around 180 K and 100 K, respectively. With the decreased Curie temperature for thinner FGT layers, the coercive fields also decrease under the same temperatures. Apparently, thermal

fluctuations play a more important role for thinner samples, where the perpendicular magnetic anisotropy is relatively weak compared to the bulk crystals.

3.2 Transport properties of WTe_2 films

Fig. 3.5 shows the Td phase of WTe_2 crystal structure, where the a, b plane form a monolayer WTe_2. The tungsten (W) atoms are sandwiched by two tellurium (Te) atomic sheets and the three nearest Te atoms from each sheet form a triangular pyramid with the W atom, with the two resulting opposing pyramids rotated 180° along the c axis from each other. The bulk crystal is formed by WTe_2 monolayer stacks layer by layer along the c axis. The Td phase of the WTe_2 we have used in our experiment has been proved by our collaborators[87]. The WTe_2 single crystals were synthesized through the CVT method described before in Section 3.1. The stoichiometric mixture of W and Te powders were sealed in a quartz tube with iodine used as a transport agent 2 mg/cm^3. The quartz tube was loaded into a double-zone furnace with a temperature gradient from 900°C to 800°C. Plate-like single crystals can be obtained after one-week growth. After growth, the composition and structure of the crystals were checked by an energy-dispersive X-ray spectrometer and an X-ray diffractometer, respectively.

As a control sample, which is used to differentiate from the transport signal in WTe_2/FGT structure, the Hall resistivity of h-BN/monolayer WTe_2 has been shown in Fig. 3.6. It exhibits Hall resistivity close to a linear relation.

The temperature dependence of the longitudinal resistivity shows an insulating behavior where it decreases as the temperature increases. Monolayer WTe_2 has a resistivity on the order of 10^4 Ω

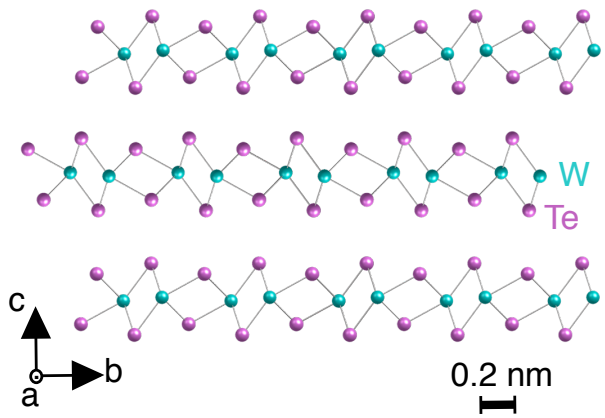


Figure 3.5. Schematic side view of the atomic lattice of WTe_2 with a scale bar of 2 Å. The pink and green atoms are for Te and W atoms, respectively.

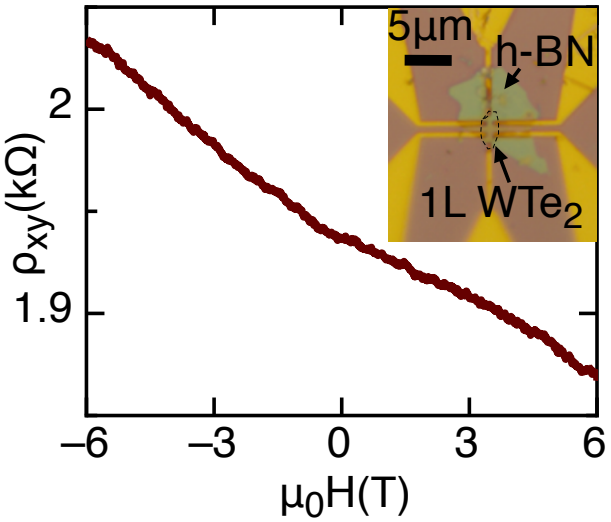


Figure 3.6. Hall resistivity of a monolayer WTe_2 on bottom electrodes at 2 K close to a linear relation, which helps exclude the possibility that the dips and peaks in the Hall resistivity of WTe_2/FGT are from WTe_2 film.

at $\sim$ 10 K, and is relatively more insulating than a few-layer FGT.

3.3 Topological Hall effect in WTe_2/FGT heterostructure

Pristine FGT has a strong perpendicular magnetic anisotropy (PMA) and spin polarizations are always along the out-of-plane direction. However, the spin polarizations in FGT can be signif-

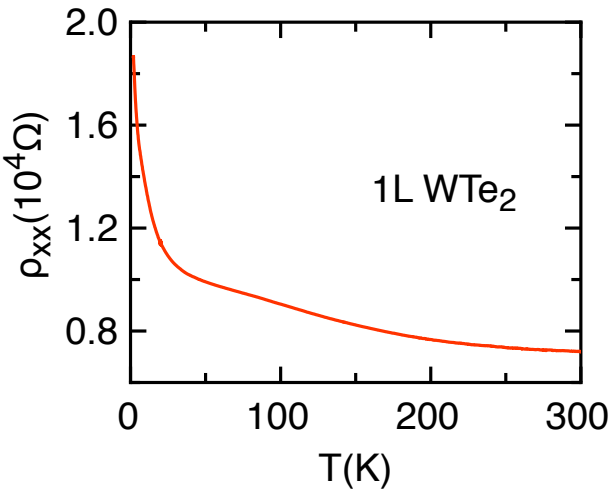


Figure 3.7. Temperature dependence of longitudinal resistivity of monolayer WTe_2 shows an insulating behavior. Thus in the WTe_2/FGT heterostructure, the current mainly goes through FGT since FGT is more electrically conductive.

icantly modified when coupled to a monolayer or a few-layer WTe_2 which as measured before has a large spin-orbit coupling. This leads to rich many physical phenomena, one of which is the topological Hall effect (THE), a signature of the magnetic skyrmions.

Magnetic skyrmions are small swirling topological magnetization texture and the spins inside a skyrmion rotate progressively with a fixed chirality from the up direction at one edge to the down direction at the center and then to the up direction again at the other edge. Their stabilization and dynamics rely on their topological properties. Mostly, skyrmions are induced by chiral exchange interactions, i.e. Dzyaloshinskii-Moriya interaction (DMI), between electron spins[88], associated with atoms in non-centrosymmetric magnetic compounds or in thin films with a broken inversion symmetry. Their sizes can be extremely small, with diameters in the nanometers range. They behave like particles that can be moved, created and annihilated, and thus they are suitable for applications in information storage and logical technologies.

There are two types of skyrmions: Néel-type and Bloch-type skyrmions as shown in Fig. 3.8

(The graphs are adopted from Ref. [89].) These two types of skyrmions have different directions of the rotation, which are related to different symmetries of the interactions between spins. For example, this difference of symmetry may be due to the underlying crystal lattice or to the presence of an interface.

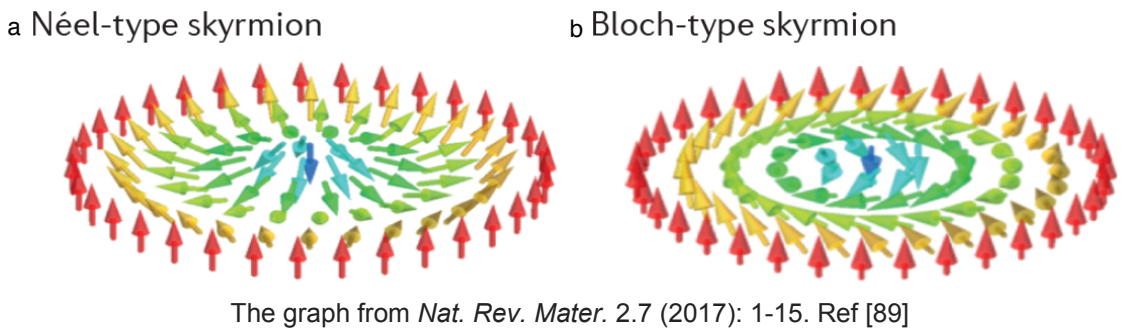


Figure 3.8. Magnetic texture of skyrmions[89]. **a**, Néel-type and **b** Bloch-type skyrmions with magnetization rotating from the down direction at the center to the up direction of the edge.

THE arises from the accumulated Berry phase acquired by conduction electrons in the adiabatic limit as they pass through a skyrmion[88]. The Berry phase is proportional to the skyrmion number and results in an emergent magnetic field produced by the skyrmion. This field can induce a transverse deflection of the electrons and thus a measurable Hall voltage that allows a purely electrical detection of the skyrmions[90, 91, 92]. Stepwise profiles of the topological Hall resistivity were observed in the course of the varying the applied magnetic field in FeGe Hall-bar structures[93]. A distinct additional contribution to the Hall effect in certain temperature and magnetic field ranges of a skyrmion lattice was reported in B20 materials like MnSi[91].

WTe_2 has one of the largest spin-orbit coupling among the transition metal dichalcogenides. At the WTe_2/FGT interface, the terminated atoms in WTe_2 are the same as those in FGT (Fig. 3.9). These two layers of Te atoms can be coupled through the $5p$ orbital and strong spin-orbit interaction

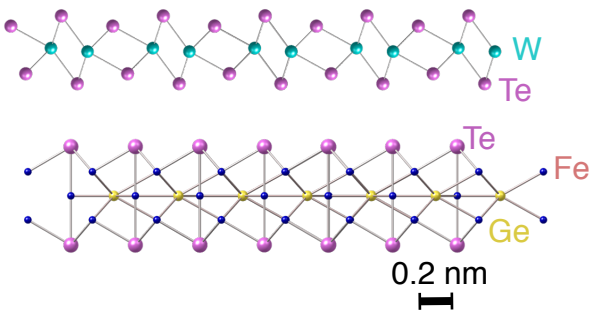


Figure 3.9. Schematic graph for monolayer WTe_2 on monolayer FGT. The van der Waals gap between this two materials is set as ~ 3 $\mathring{A}$. This graph is drawn with a software called CrystalMaker.

in WTe_2 can significantly modify the spin polarizations in FGT. Thus transport measurements were adopted to investigate the spin textures in this WTe_2/FGT heterostructure. We start from sample A (h-BN/1L WTe_2/4L FGT), where hexagonal boron nitride (h-BN) is served as the protection layer and helps prevent the samples from being oxidized in the air.

This device is assembled from the pick-up transfer method. To fabricate the device, the bottom electrodes were patterned first by e-beam lithography. Then 5/30 nm Cr/Au was evaporated to form the bottom electrodes. After that, WTe_2 and FGT from high-quality bulk materials were separately exfoliated onto the 300 nm SiO_2/Si substrates. Then PDMS/PPC on a glass slide was used to pick up the monolayer WTe_2 on the substrate. During the pick-up procedure, the sample stage was heated up to 50°C when the PDMS/PPC was lowered to touch WTe_2 and shut down while detaching the PDMS/PPC from the sample stage. After that, the WTe_2 was attached to the PDMS/PPC. The PDMS/PPC/WTe_2 was then used to pick up FGT thin layers using the similar procedures. The resulted PDMS/PPC/WTe_2/FGT was then transferred and properly aligned onto the prepared bottom metal electrodes under the microscope. After putting the whole structure into acetone, the final WTe_2/FGT heterostructure on the bottom metal electrodes was obtained. To protect the structure from oxidization in air, a h-BN thin flake was transferred onto the surface of

WTe_2. All these procedures were carried out inside the glove box with a good inertia atmosphere condition (filled with N_2 gas).

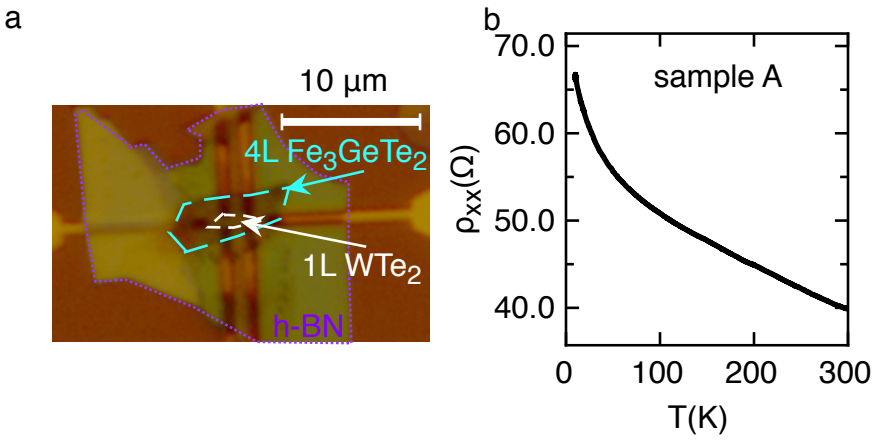


Figure 3.10. Transport properties of sample A. **a**, Microscopic image of sample A with 1L WTe_2/4L Fe_3GeTe_2 transferred onto the bottom electrodes. **b**, Longitudinal resistivity dependence on the temperature shows an increasing resistivity with decreasing temperature.

Fig. 3.10 shows the resistivity dependence on the temperature of sample A (h-BN/1L WTe_2/4L FGT). In the whole temperature range from 10 K to 300 K, the resistivity is in the order of several tens of ohms, which is at least two orders of magnitude smaller than that of the control sample having monolayer of WTe_2 as shown in Fig. 3.7 in Section 3.2. Thus in the sample A, the conductance is mainly contributed from FGT as the monolayer WTe_2 does not contribute significantly in conductance.

In addition, the transport signals in 30L FGT with WTe_2 (sample B) ware investigated. The longitudinal resistivity dependence on the temperature is shown in Fig. 3.11. This structure with a much thicker FGT shows the resistivity on the order of several ohms.

Similar to sample A (h-BN/1L WTe_2/4L FGT), another sample with 3L FGT and WTe_2 also shows an insulating behavior from the longitudinal resistivity dependence on temperature (Fig.

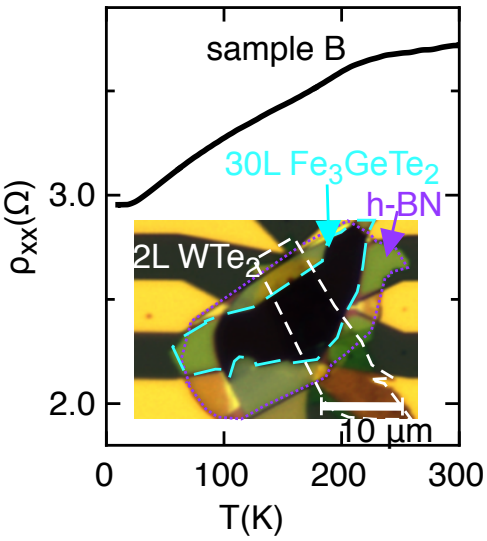


Figure 3.11. Longitudinal resistivity dependence on the temperature for sample B shows a metallic behavior. The resistivity is close to that of FGT as the resistivity of monolayer WTe_2 is two orders of magnitude larger. The inset shows the device configuration of h-BN/WTe_2/FGT on the bottom electrodes.

3.12).

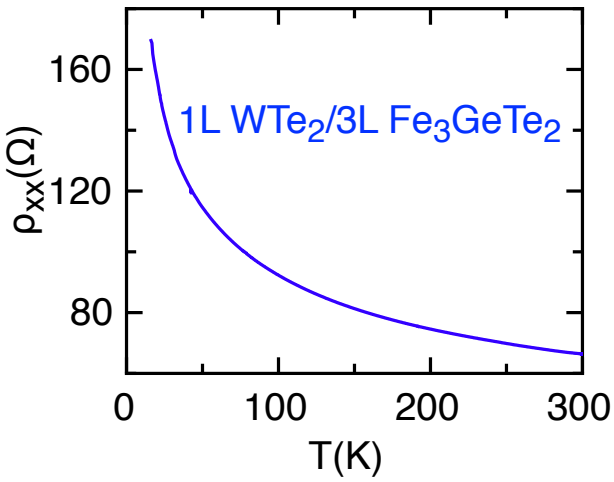


Figure 3.12. Longitudinal resistivity dependence on the temperature for 3L FGT with WTe_2 shows an increasing resistivity with decreasing temperature.

The Hall resistivity dependence on magnetic field at different temperatures for sample A is shown in Fig. 3.13. The Curie temperature for sample A is about 150 K and this is close to that of a pristine 4L FGT. THE was also investigated using transport measurements. In the WTe_2/FGT

structure, dips and peaks near the magnetic phase transition edge are observed at temperatures below 100 K. For example, there are pronounced dips and peaks at an out-of-plane magnetic field strength $\sim \pm 975$ Oe. These dips and peaks signify the presence of THE.

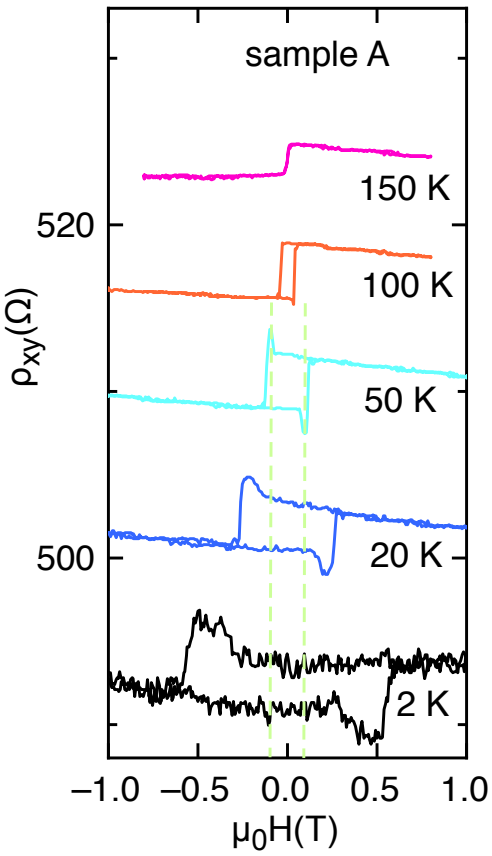


Figure 3.13. Topological Hall effect in sample A. The magnetic field is applied in an out-of-plane direction. The dips and peaks appear near the magnetic phase transition at temperatures lower than 100 K, which signify the presence of THE.

Being different from sample A, sample B (h-BN/2L WTe_2/30L FGT) with a much thicker FGT shows a completely distinct Hall resistivity dependence on magnetic field. For sample B, PMA is well preserved in FGT when the temperature is below 180 K as shown in Fig. 3.14, which is demonstrated by the square shape of the hysteresis loop. However, within an intermediate temperature window ranging from 180 K to 200 K, the hysteresis loops have step-like transitions.

For example, sweeping from positive magnetic field to negative one at 190 K, the Hall resistivity jumps from the high saturation value to an intermediate level and then changes linearly until the low saturation value is achieved. The reverse trace does the opposite as expected. A possible explanation for this magnetic field dependent step-like behavior is due to the formation of multi domains in this sample. This conjecture is supported by the observed labyrinth domain structures in a WTe_2/30L FGT sample with Lorentz transmission electron microscopy (L-TEM) as further explained in Section 3.4.

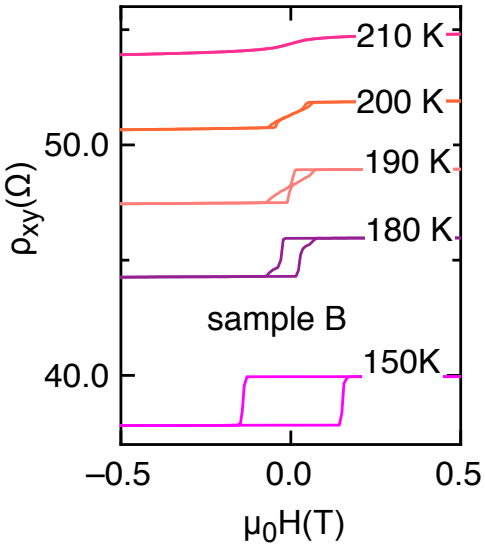


Figure 3.14. Step-like magnetic transitions in sample B at temperatures from 180 K to 200 K, which is related to the formation of multi domains. The magnetic field is applied in an out-of-plane direction.

Compared to sample B (with a thick FGT layer), sample A (with a thin FGT layer) shows a strong interface coupling between FGT and WTe_2, giving rise to the THE. For sample B, no THE peaks and dips were seen since the measured averaged transport signal from WTe_2 and thick FGT. This may lead to the smearing out of the THE from the proximity effect if the THE signal is much weaker than that from anomalous Hall effect.

3.4 Néel-type skyrmions under Lorentz transmission electron microscopy

A key consideration of studying skyrmion systems is the characterization of the physical structure of the samples and particularly the direct observation of the magnetization textures. To date, various methods like magnetic-force microscopy, photoemission electron microscopy, scanning electron microscopy with polarization analysis and L-TEM are designed for these purposes. Among all the techniques, L-TEM is one of the most direct methods to obtain the magnetic domain structures, domain walls and skyrmions with a high spatial resolution, since other techniques based on Kerr microscopy and X-ray are limited by spatial resolution. Besides, the scattering cross-section for electrons in L-TEM is significantly larger than that of X-rays and thus improvements in signal contrast especially for the ultrathin films are achieved in L-TEM. In this section, the observations of magnetic skyrmions by L-TEM will be described.

$In\ situ$ L-TEM imaging was carried out by using a FEI Titan Cs Image TEM in Lorentz mode (the Fresnel imaging mode) at 300 kV. By tilting the sample, an in-plane field can be applied. The ratio of the in-plane and out-of-plane field can be tuned by varying the tilt angle.

3.4.1 Principles of Lorentz electron transmission microscopy

L-TEM is a high resolution method ideally suitable for obtaining quantitative image for chiral magnetic domains and textures. Key length scales such as grain size and chiral variations of the magnetization can be identified and measured when analyzing both planar and cross-sectional samples under L-TEM. The principles of this technique are based on Lorentz force. With the

deflection of electron beam due to an in-plane magnetic field, a contrast at a region of varying magnetization can be formed.

For Néel-type domain boundaries in materials with PMA, no magnetic field contrast is observed when the sample plane is normal to the beam propagation direction. That is, with PMA in the sample the magnetization is along the out-of-plane direction which is parallel to the electron beam propagation direction. Thus this leads to a zero Lorentz force and no contrast. This can also be understood from the following equation. Using the full electron-wave treatment of the electron beam within the small defocus limit[94], the contrast in L-TEM from the magnetic structure can be expressed through the curl of the magnetization along the beam propagation axis (z direction):

$$I(\mathbf{r}, \Delta) = 1 - \frac{\Delta e \mu_0 \lambda t}{h} (\nabla \times \mathbf{M}(\vec{r})) \cdot \mathbf{z}, \tag{3.1}$$

where $I(\mathbf{r}, \Delta)$, Δ, e, μ_0, λ, h, t and $\mathbf{M}(\mathbf{r})$ are the normalized intensity, the defocus, electron charge, vacuum permeability, electron wavelength, Planck's constant, film thickness and film magnetization, respectively. This defocus range is dependent on the microscope specific parameters and valid in the region where the contrast transfer function is linear with defocus. For Néel-type skyrmion, the curl of the magnetization lies completely in the sample plane and thus no sample contrast can be formed for Néel-type skyrmions with a zero sample tilt.

However, by tilting the sample plane with respect to the beam direction, the projection of the magnetization in the sample plane enables the skyrmion contrast as schematically shown in Fig. 3.15. When the sample plane is tilted by an angle α out of the original plane, the projection of the magnetization is nonzero in the sample plane as indicated by the brown arrows. This leads to a

nonzero Lorentz force as indicated by the grey arrows. The electrons from the core and outside of the skyrmions are deflected to the opposite directions, which leads to dark in the bottom and bright on the top or bright (dark-bright) in the bottom and dark on the top (bright-dark) contrasts. The skyrmion size is determined by the distance between the center of the dark-bright or bright-dark contrasts.

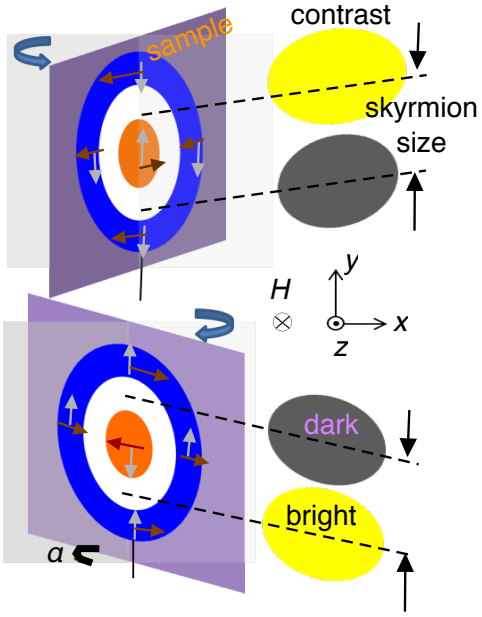
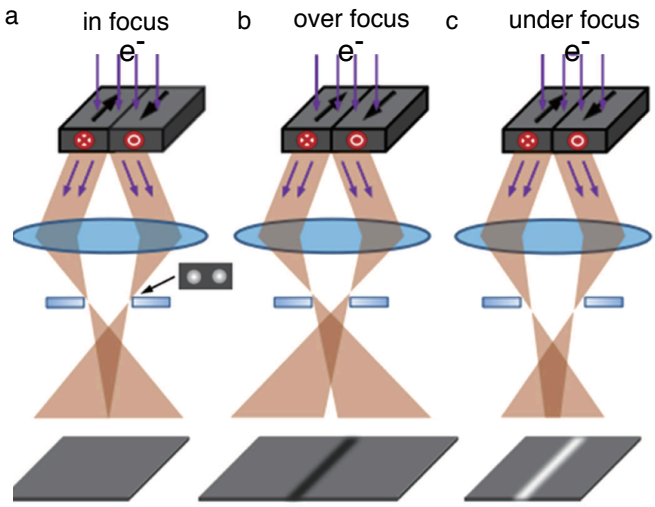


Figure 3.15. Schematic diagram of a Néel-type skyrmion on a tilt sample for Lorentz transmission electron microscopy imaging. The red and blue circles are for positive and negative magnetizations along z direction, respectively. Brown arrows indicate the in-plane magnetization component while grey arrows indicate the Lorentz force.

Among the most common techniques for imaging the magnetic domains in L-TEM are Foucault and Fresnel modes. In our experiment, the Fresnel or defocus mode is adopted for the imaging and contrast can only be obtained in the defocus region as illustrated in Fig. 3.16[95]. For a simple explanation, a sample with antiparallel magnetic domains is adopted. When the parallel electron beam passes through the magnetic domains, the Lorentz force leads to the deflection of electrons and as a result the diffraction spot splits into two, following the right-hand rule. In the in-focus



Graph from *Chin. Phys. B*, 27(2018): 066802. Ref. [95]

Figure 3.16. Schematic of ray diagrams indicating the paths of electrons passing through a magnetic specimen under the Fresnel or defocus mode of Lorentz transmission electron microscopy[95] for **a** in-focus, **b**, over-focus and **c** under-focus cases.

case, the deflecting electrons are focused in the final image plane and no magnetic contrast appears. For the over-focus case, a decreased intensity comes from the deflected electrons away from the domain wall. This leads to dark contrast lines in the domain wall region. Similarly, bright contrast lines appear in under-focus case because of the increase electron intensity from the converged electrons.

3.4.2 Enhanced DMI in FGT with WTe_2

Strong PMA in FGT favors an out-of-plane magnetization and this makes the spin polarizations form the domain in the up or down direction. However, the formation and structure of domain walls are resulted from the competition between three main factors, i.e., exchange interaction, magnetic anisotropy, and dipolar interaction. The exchange interaction includes DMI, a noncollinear exchange interaction which favors a chirally skyrmion of a specific rotational direction. Further the

strong PMA along would lead to a stabilized single domain. The dipolar interaction is dependent on the layer thickness, which decreases with reduced thickness. In our experiment, by comparing the magnetic domains in the WTe_2/30L FGT sample with the nearby pristine 30L FGT regions as shown in Fig. 3.17 using L-TEM, the interfacial coupling between the WTe_2 and FGT thin layers indeed contributes a strong DMI.

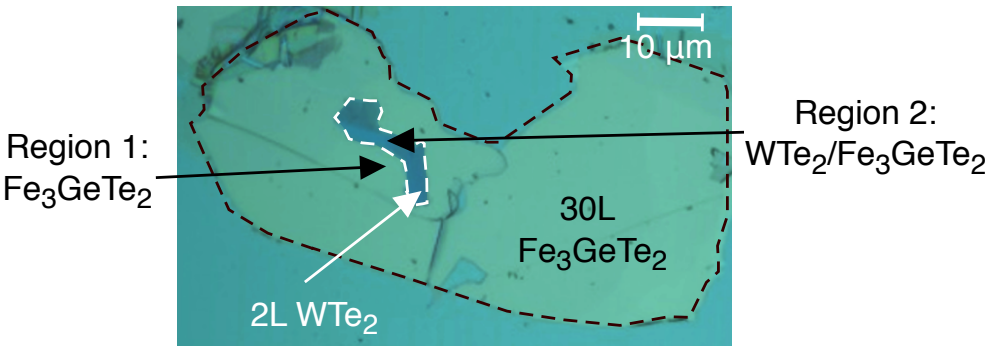


Figure 3.17. Sample for comparing the domain difference in 30L FGT with and without bilayer WTe_2. The white dashed line region is for FGT with WTe_2 while other regions inside the black dashed line is for FGT only.

Fig. 3.18 shows the magnetic domain images for the 30L FGT thin flakes without WTe_2 in region 1 indicated in Fig. 3.17. The film exhibits labyrinth domains at 94 K with 0 T applied magnetic field. This could help explain the step-like magnetic transition observed from the transport study earlier in Fig. 3.14, Section 3.3. When the in-plane field is tuned to the opposite direction with α= -20° and α=21° as shown in Fig. 3.18, the contrast of domain edge completely switches the sign from bright to dark.

For the WTe_2/FGT heterostructure, there is no contrast when α=0° as shown in Fig. 3.19 and this indicates the Néel-type nature of the domain. When $\alpha \neq$0°, aligned and stripe-like domains appear with a certain domain width at 0 T. This domain structures is sharply different from that

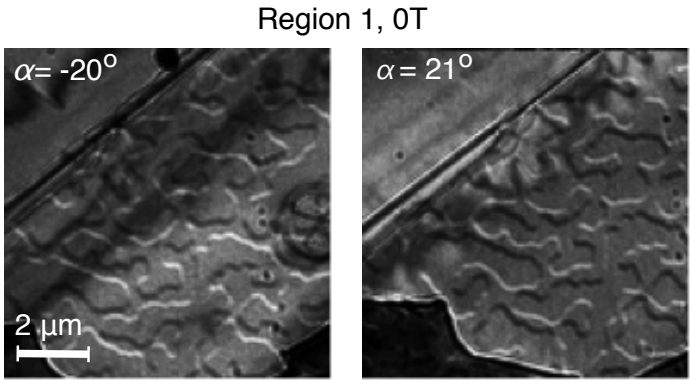


Figure 3.18. Typical labyrinth domain in 30L FGT thin flakes in region as shown in Fig. 3.17 at a 0T magnetic field. This sample has the same FGT thickness as that of sample B (h-BN/2L WTe_2/30L FGT) for studying transport properties.

of FGT thin films in Fig. 3.18 by having a much smaller domain width. Thus the DMI is largely enhanced in this heterostructure from the coupling of the interfacial Te atoms.

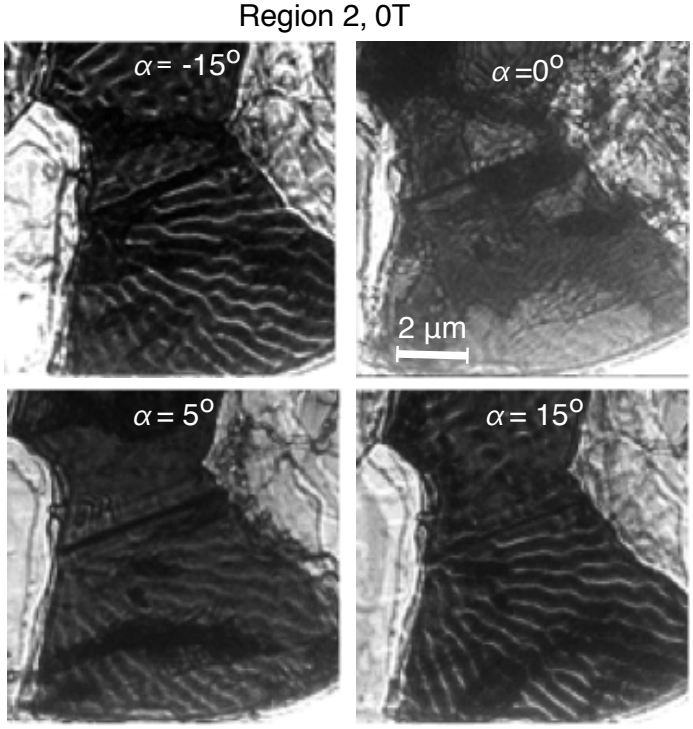


Figure 3.19. Much smaller domain width observed in WTe_2/30L FGT heterostructure. The contrast changing with the tilt angle α and disappearing when $\alpha = 0°$, which indicates the Néel-type nature of the magnetic domains. From the aligned and stripe-like domain structures of the WTe_2/FGT, a Dzyaloshinskii-Moriya interaction energy is estimated to be ~ 1.0 mJ/m^2.

To determine the domain width, a method from Bodenberger and Hubert[96] is adopted, which

appears to be the most universal and commonly applied method[97, 98]. A stereological method[96] is used to define the surface magnetic domain width w of complicated or arbitrary magnetic structure patterns. The domain width w is defined as:

$$w = \frac{2 \times \text{total test line length}}{\pi \times \text{number of intersections}}, \tag{3.2}$$

where the domain width is determined as the ratio of the total test line length to the number of intersections of domain walls. In our experiment, four test straight lines running in random directions are used for evaluation of the total domain width. It is illustrated in Fig. 3.20 with four drawing test lines. As a result, the averaged domain width is estimated to be 290±10 nm.

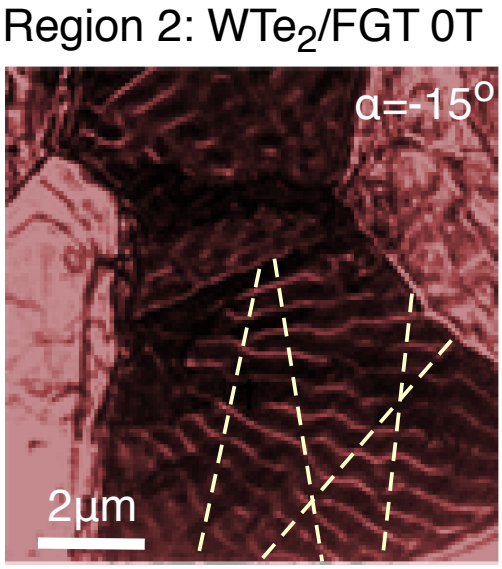


Figure 3.20. Representative image used to obtain the averaged domain width of 2L WTe_2/30L FGT sample. Four line cuts are taken and the magnetic strip domain width is taken as the averaged value, determined to be 290±10 nm.

With the domain width, a DMI energy can be obtained from a phenomenological model, which describes the dependence of the domain width w on the domain wall energy δ_W as in the

following[99]:

$$w = \beta \frac{4\pi\delta_{\mathrm{W}}}{M_s^2}, \tag{3.3}$$

where δ_{W} is the domain wall energy. It is related to exchange stiffness A, uniaxial magnetocrystalline anisotropy constant K_{u} and DMI constant $|D|$ by $\delta_{\mathrm{W}} = 4\sqrt{AK_{\mathrm{u}}} - \pi|D|$[100]. Thus, this domain wall energy is related to the DMI term. Besides, β is a phenomenological fitting parameter and taken to be 0.31 for FGT[99]. With a domain width of 290 nm, a domain wall energy $\delta_{\mathrm{W}} = 0.77\mathrm{mJ/m^2}$ is obtained. This domain wall energy is related to the DMI term. However, for the pristine FGT without considering DMI, the domain wall energy is simply $\delta'_{\mathrm{W}} = 4\sqrt{AK_{\mathrm{u}}}$. By comparing these two domain wall energy values, we can obtain the DMI energy $|D| = 1.0\,\mathrm{mJ/m^2}$ in the WTe_2 and FGT interface. During the estimation, the uniaxial anisotropy constant K_{u} can be derived via[101]:

$$\frac{2K_{\mathrm{u}}}{M_{\mathrm{s}}} = \mu_0 H_{\mathrm{sat}}. \tag{3.4}$$

As shown in Fig. 3.21, the saturation field H_{sat} decreases as the temperature increases. Thus the ratio of the uniaxial anisotropy constant $K_{\text{u-94K}}/K_{\text{u-5K}}$ and the ratio of the saturated magnetization $M_{\text{s-94K}}/M_{\text{s-5K}}$ at 94 K and 5 K can be estimated from the ratio of the saturation fields and saturated anomalous Hall resistivity values at 94 K and 5 K, respectively. Using the parameters for bulk FGT around 5 K[99]: $M_{\text{s-5K}} = 376\,\mathrm{emu/cm}$, $K_{\text{u-5K}} = 1.46 \times 10^7\,\mathrm{erg/cm^3}$, $A = 10^{-7}\,\mathrm{erg/cm^{-1}}$, $K_{\text{u-94K}} \sim 9.7 \times 10^6\,\mathrm{erg/cm^{-3}}$ is obtained. As a result, a domain wall energy for FGT without the DMI term δ'_{W} is $\sim 3.9\,\mathrm{mJ/m^{-2}}$.

The DMI energy is related to the domain wall energy by $|D| = (\delta'_{\mathrm{W}} - \delta_{\mathrm{W}})/\pi$. Thus a DMI energy of $\sim 1.0\,\mathrm{mJ/m^2}$ is extracted in our system. This value is comparable to the reported values

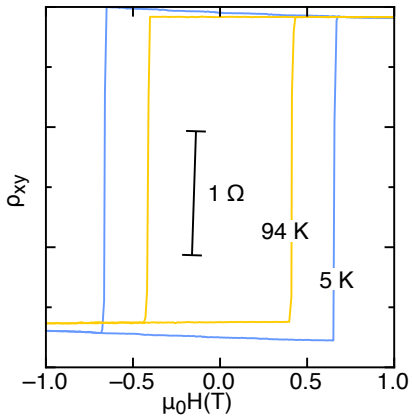


Figure 3.21. Hall resistivity shifted for clarity of 2L WTe_2/30 L FGT heterostructure at 5 K and 94 K. The magnetization ratio is estimated from the ratio of the anomalous Hall resistivity value.

in heavy metal/ferromagnet thin film systems[102]. The critical value $|D_{\mathrm{C}}|$, which is the smallest DMI energy required to stabilize chiral Néel domain wall is expressed as[102, 103]:

$$|D_{\mathrm{C}}| = \frac{4}{\pi}\sqrt{\frac{A}{K_{\mathrm{eff}}}}K_{\mathrm{d}}, \tag{3.5}$$

where $K_{\mathrm{d}} = 2\pi M_{\mathrm{s}}^2$ is the magnetostatic or stray field energy constant and K_{eff} is the effective anisotropy constant. In the FGT system with a strong PMA, the measured value of K_{eff} can be an approximate value of K_{u}. Hence, $|D_{\mathrm{C}}|$ is estimated to be 0.1 mJ/m^2 so that $|D| > |D_{\mathrm{C}}|$ ($|D| \sim 10|D_{\mathrm{C}}|$) and chiral Néel textures are expected.

With a large DMI established at the WTe_2/FGT interface, Néel-type skyrmions are expected in this heterostructure. Here we show the domain difference in 35L FGT with and without 8L WTe_2 and skyrmions are observed in the region of 8L WTe_2/35L FGT (Fig.3.22). For the FGT without WTe_2, the magnetization saturates and enters a ferromagnetic phase when the field is 600 Oe at 195 K while a group of skyrmions shows up in the 35L FGT with WTe_2. The examples of the

observed skyrmions are shown by the purple circles in the zoom-in image at a field of 660 Oe. The DMI at the interface generates the skyrmions and other parts of FGT away from the interface enter uniform ferromagnetic phase, which contributes no contrast. As a result, the image captured for the heterostructure is the skyrmions at the interface.

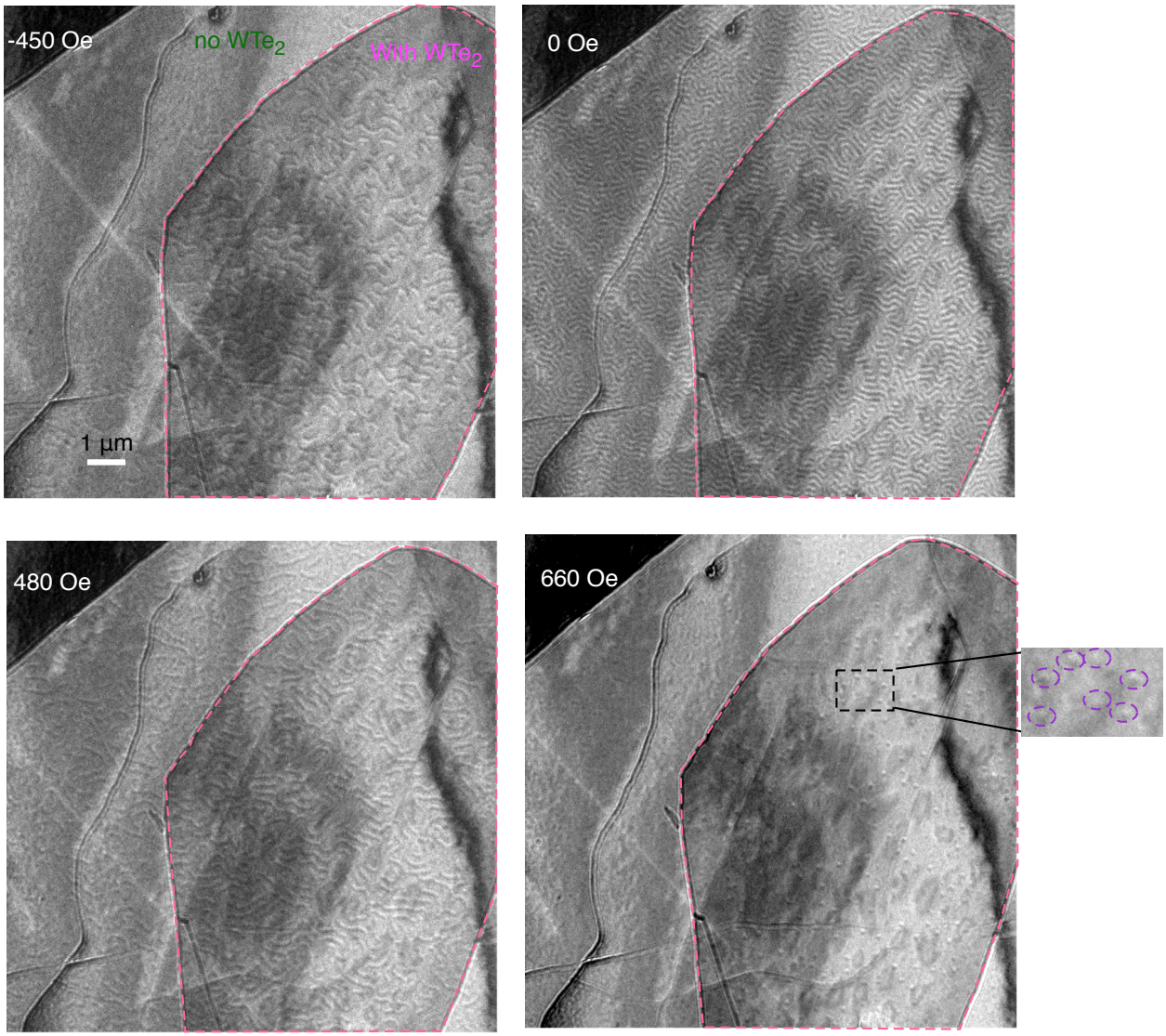


Figure 3.22. L-TEM images of magnetic domains for 35L FGT with and without 8L WTe_2 at 195 K with a tilting angle 30° and a varied field. The dashed pink line region is the Fe_3GeTe_2 with WTe_2. With magnetic fields in z-direction (as defined in Fig. 3.15) are -450 Oe, 0 Oe and 480 Oe, magnetic domain widths are smaller in WTe_2/FGT region compared to that in FGT region. Magnetic skyrmions appear at a magnetic field of 660 Oe. We have zoomed in and indicated the skyrmions with purple dashed circles.

The detailed magnetic domain evolution for this structure is shown in Fig. 3.23 with smaller magnetic field steps of 15 Oe or 30 Oe in the range of 480 Oe and 630 Oe as shown in the Fig. 3.23. When the magnetic field is varied with a small step, the pristine FGT does not show any clear sign of skyrmions and it enters a uniform single domain directly with the magnetic field reaches saturated field. As a comparison, WTe_2/FGT region gradually develop and present skyrmions with the increasing magnetic field. Besides, the WTe_2/FGT regions always show smaller domain wall widths compared to the pristine FGT.

3.4.3 Néel-type nature of the skyrmions

With an enhanced DMI, Néel-type skyrmions are observed in WTe_2/FGT heterostructure. L-TEM imaging was performed at a defocus ranging from -2.00 mm to 2.50 mm, at 180 K, and a field of 510 Oe. A focus series taken at -2.00 mm, -1.50mm, -1.01 mm, 0.00 mm, 1.02 mm, 1.50 mm, 2.00 mm, 2.50 mm is shown in Fig. 3.24, respectively. The image contrast, identifiable to that of Néel skyrmions shown in Fig. 3.23, indicates the presence of Néel-type skyrmion lattice stable at 180 K. From under focus to over focus, the skyrmions transform from white on the top and dark in the bottom to the opposite contrasts. These are consistent with the Néel-type nature of the skyrmions. Besides, when it is in-focus, there is no observable contrast of skyrmions under L-TEM.

The dependence of the observed skyrmion contrast on the magnetic field also support its Néel-type nature, where the magnetic field is swept from -1000 Oe to 1000 Oe at 197 K with a tilt angle of 30°. The skyrmions appeared at -600 Oe and 630 Oe as shown in Fig. 3.25. At -600 Oe, inside

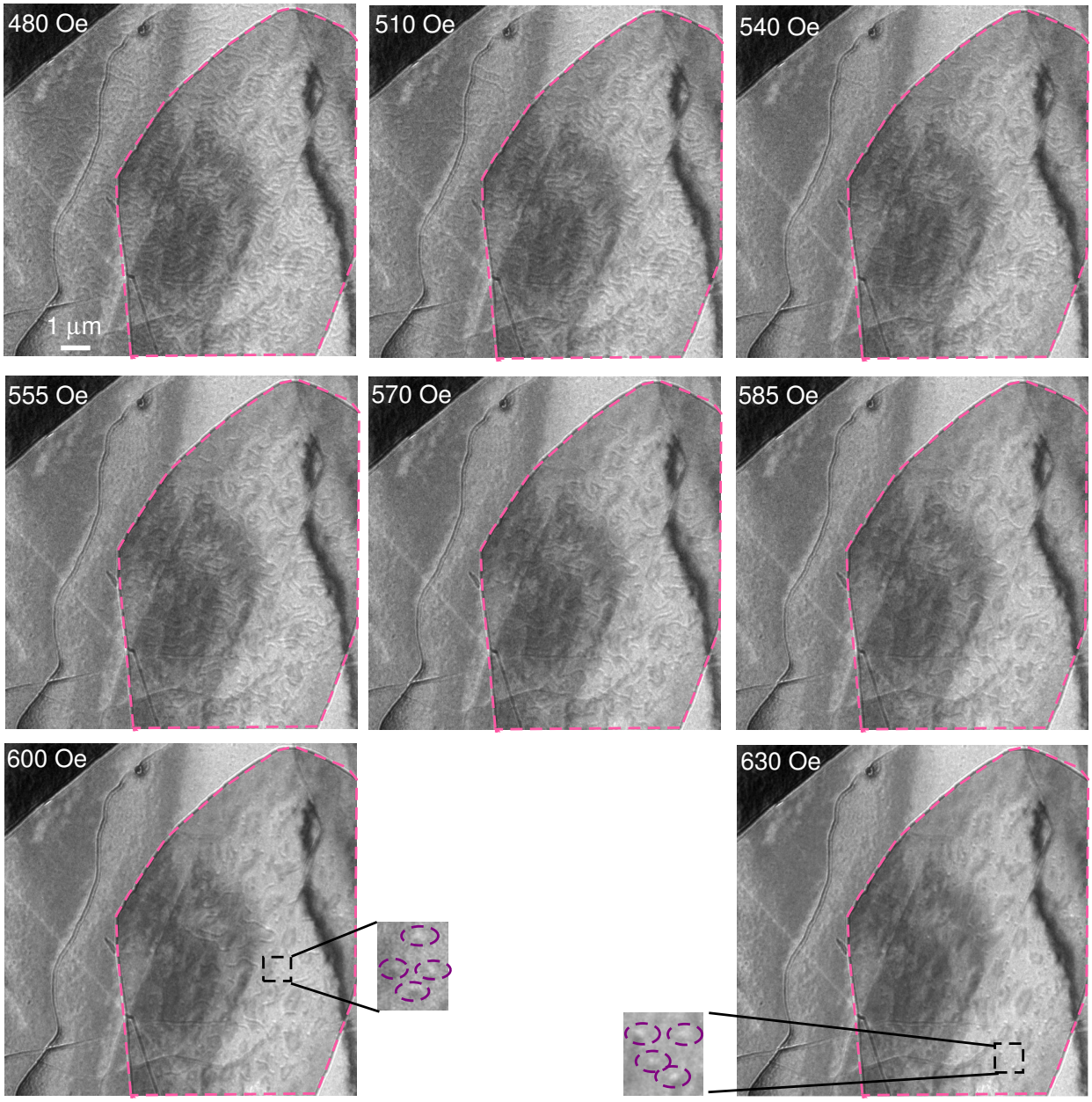


Figure 3.23. Magnetic domain difference for 35L Fe_3GeTe_2 with and without 8L WTe_2 at 195 K with a tilting angle 30° and the detailed field dependence between 480 Oe and 630 Oe. FGT region enters into the single uniform magnetic domain when the magnetic field is large enough ($\sim$ 660 Oe), while FGT with WTe_2 shows emerging skyrmions.

each skyrmion, the image appears dark on the top and bright in the bottom. After the field reversal, at 630 Oe, the dark and bright regions indeed swapped: dark in the bottom and bright on the top.

The field dependence of a single skyrmion in the WTe_2/30L FGT sample (similar to sample B

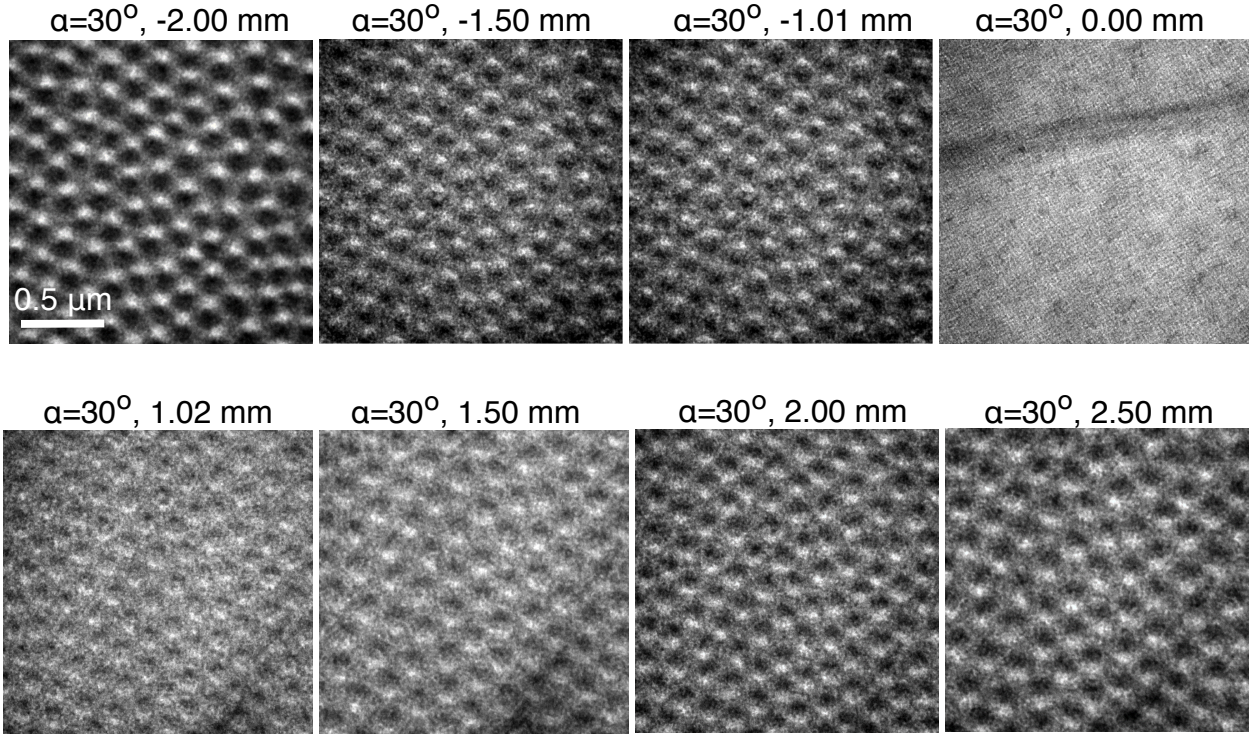


Figure 3.24. Defocus images of skyrmion lattice for WTe_2/40L FGT sample at a field of 510 Oe at 180 K. When the focus is changed from de-focus (-2.00 mm, -1.50 mm, -1.01 mm) to over-focus (1.02 mm, 1.50 mm, 2.00 mm, 2.50 mm), the skyrmion contrasts change from dark in the bottom and bright on the top to bright in the bottom and dark on the top.

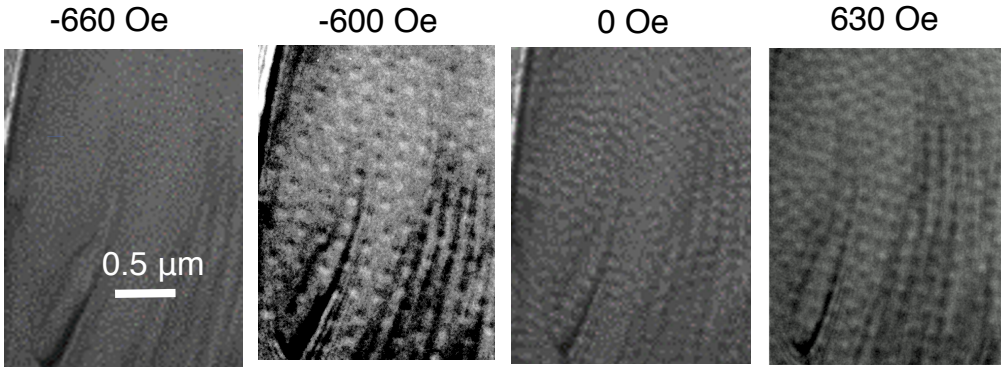


Figure 3.25. The dependence of the skyrmion contrast on the magnetic field at 197 K with a tilt angle of 30° for WTe_2/40L FGT sample. The skyrmions appear at -600 Oe and 630 Oe. The contrast is adjusted for clarity.

for the transport measurements) is shown in Fig. 3.26 with a field ranging from 540 Oe to 660 Oe at 94 K. The skyrmion is well developed at a field of 540 Oe and 600 Oe along the z direction, having a contrast of dark on the top side and bright in the bottom. The size is estimated to be $\sim$150

nm at 94 K from the intensity at each point of an image .

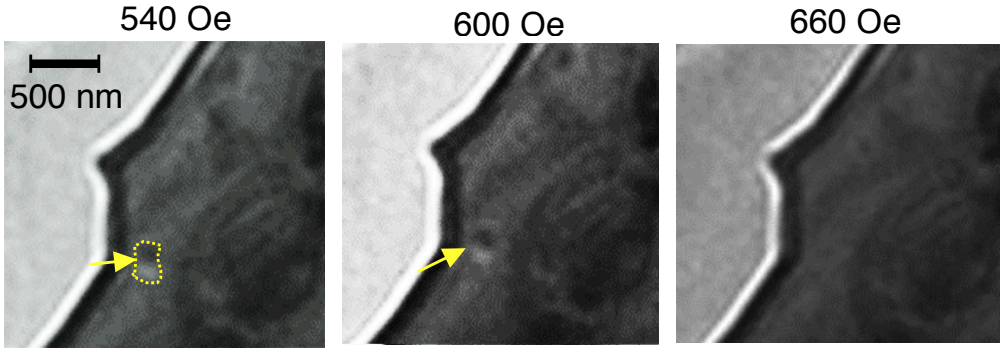


Figure 3.26. Lorentz transmission electron microscopy observation of a Néel-type skyrmion at T=94 K, α=21.86° and H=540 Oe, 600 Oe, where α is the angle between the sample plane and xy plane. The yellow arrow points to a skyrmion. The skyrmion size is estimated to be ∼150 nm.

As shown in Fig. 3.27, a line profile is used to analyze the contrast for a skyrmion from the point intensity in the image. The distance between the lowest and highest intensity points is the skyrmions size. Thus the skyrmion size is extracted as ∼150 nm at 94 K and ∼80 nm at 197 K for a 2L WTe_2/30L FGT samples.

However, any domain structure in WTe_2/FGT samples with the FGT thickness less than 30L was failed to dissolve, which may be due to the small sheet magnetization in the thinner films. For thinner FGT samples, a higher beam exposure is required for the small magnetization. But this would exceed the tolerance of the samples and unrecoverable damages would occur. Thus, there is no clear magnetic domain structure observed for samples similar to sample A (WTe_2/4L FGT) and samples with the FGT thickness less than 30L.

Another evidence for the Néel-type nature of the skyrmion is from the tilt angle dependence of the image contrast as shown in Fig. 3.28. A series tilt angles of 30°, 10°, 0°, 5°, 2.5° and 0° is shown at 180 K with a field of 510 Oe for WTe_2/40L FGT sample. The skyrmion lattice image gradually disappears when the tilt angle approaches to 0°. Without any tilting, there is no

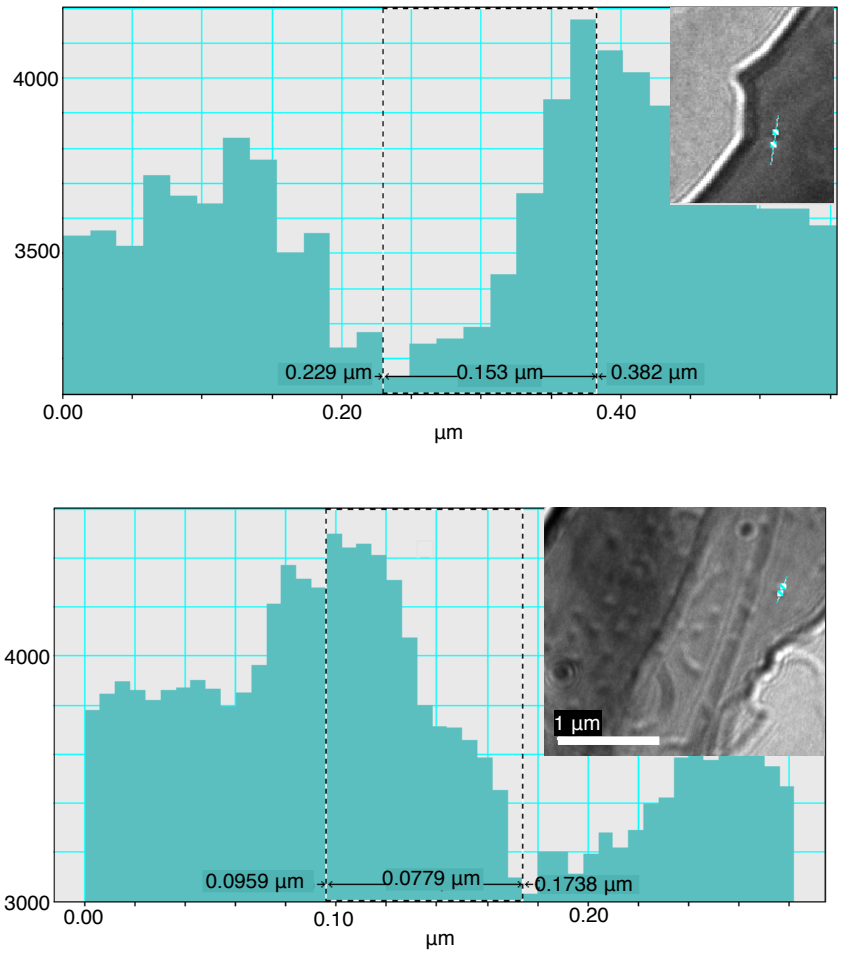


Figure 3.27. Line profile for the image of skyrmions observed in 2L WTe_2/30L FGT samples. The skyrmion size is determined from the point intensity along blue lines as shown in the insets. It is estimated to be ∼150 nm at 94 K with magnetic fields of 540 Oe and 600 Oe shown in the upper panel and ∼80 nm at 198 K with a magnetic field of 390 Oe shown in the bottom panel.

skyrmions or contrast observed.

3.4.4 Stability of the existence of skyrmions

In this section, the magnetic skyrmion position and its size dependence on time were examined to show its stability. First the magnetic field was swept from -3000 Oe to 3000 Oe for 5 times at 195 K with a tilt angle of 30° and took an image every time when the field is 780 Oe. The five images were captured at 780 Oe, showing the presence of skyrmions during each magnetic field

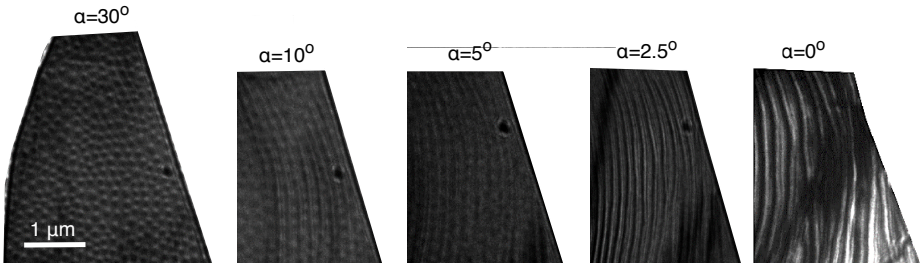


Figure 3.28. Skyrmion image dependence on the tilt angle at 180 K with a field of 510 Oe for WTe_2/40L FGT sample. When the tilt angle is close to 0° ($\alpha = 2.5°$ and $0°$), the magnetic skyrmions disappear, which is consistent with its Néel-type nature. The contrast becomes most pronounced at $\alpha = 30°$.

cycle. They did show up at random instead of fixed positions as shown in Fig. 3.29 but with the same skyrmion size all the time.

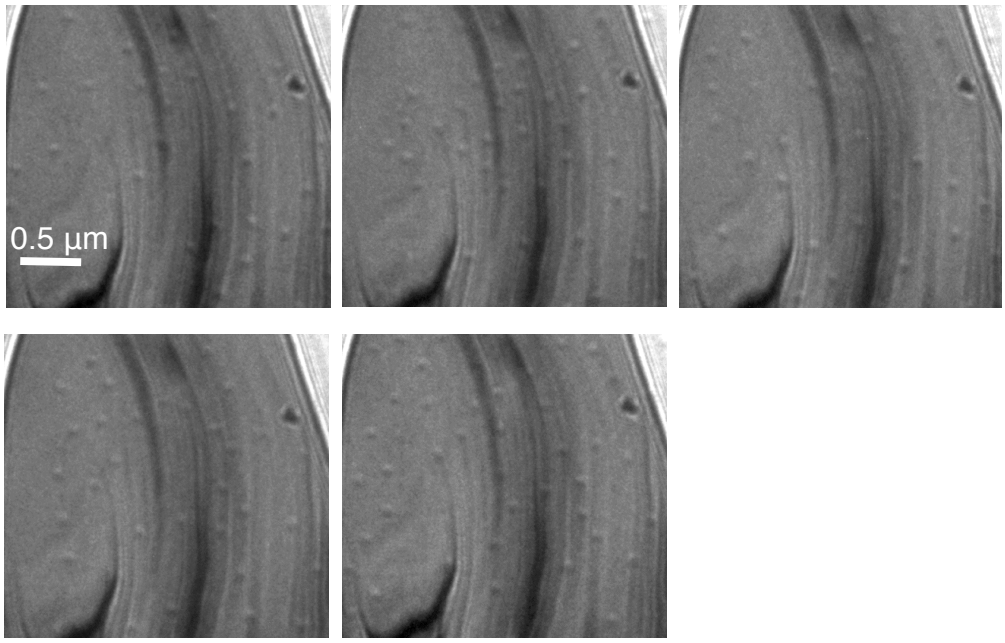


Figure 3.29. Skyrmions at different sample positions for the 2L WTe_2/40L FGT sample when the magnetic field is cycled through ,at 195 K with an angle of 30° and at the field of 780 Oe. The skyrmions show up at random instead of fixed positions.

To verify its thermal stability, a state with a high skyrmion density was initiated, then nine images were captured subsequently in two minutes. By comparing the distance between two nearby skyrmions as indicated by the purple and pink circles at 195 K with a field of 780 Oe, shown in

Fig. 3.30, a very small variation between the position of these two skyrmions are obtained. Thus the locations of the magnetic skyrmions will not change much in time.

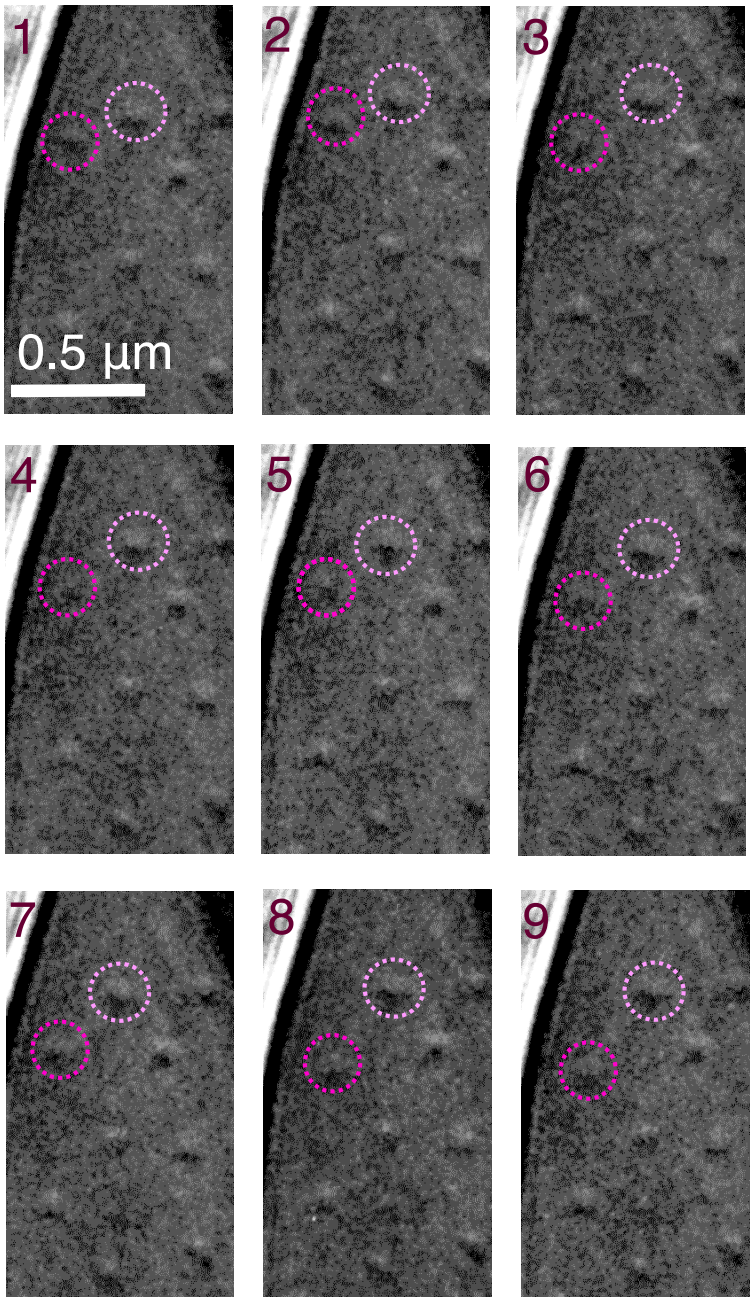


Figure 3.30. Skyrmions contrast measured at the same sample position for 9 times within totally 2 minutes at 195 K with a field of 780 Oe for WTe_2/40L FGT. The dashed circles mark two skyrmions with their relative positions changing through time. Contrast was adjusted by post processing. By comparing the distance between two nearby skyrmions as indicated by the purple and pink circles, a very small variation between the position of these two skyrmions are obtained.

3.4.5 Interface coupling in heterostructure with varied FGT thicknesses

An enhanced DMI at the interface is also supported by the smaller magnetic domain width in the WTe_2/FGT heterostructures with varied FGT thickness. As shown in Figs. 3.18 and 3.19 in Section 3.4.2, the magnetic domain width for 30L FGT with WTe_2 is much smaller than that of pristine 30L FGT. Thus a much larger DMI exists at the WTe_2/FGT interface. Similar to this case, when the FGT layer is thicker (35L), the stripe domain period is smaller compared to the regions without the WTe_2 capping, as shown in Fig. 3.31. However, when the FGT layer is 65L, no observable difference was captured. The conclusion is that, when the thickness of FGT is reduced, the interface plays a more important role, resulting in smaller stripe domain width in the WTe_2 capped regions. Thus a much larger DMI exists at the interface of a WTe_2 and a thinner FGT layer and this DMI only penetrates to a finite depth into FGT layers since in the heterostructure with 65L FGT, no observable magnetic domain difference is observed.

3.5 Micromagnetic simulation: a finite penetration depth

In addition, micromagnetic simulation has been performed for the WTe_2/FGT samples. The simulation is carried out on a 3D lattice model based on the Hamiltonian:

$$H = \sum_{<i,j>} [-J\mathbf{S}_i \cdot \mathbf{S}_j + \mathbf{D}_{i,j}(z) \cdot (\mathbf{S}_i \times \mathbf{S}_j)] - \mu_0 \sum_i \mathbf{S}_i \cdot \mathbf{H}_{\text{app}}, \tag{3.6}$$

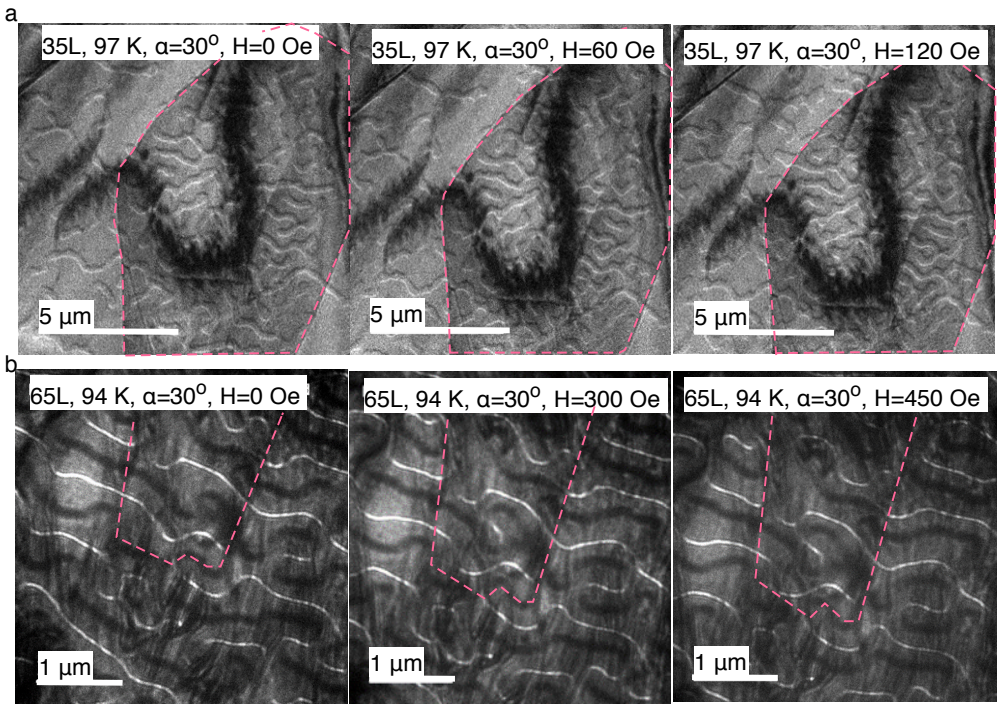


Figure 3.31. Difference of magnetic domains for the FGT and WTe_2/FGT samples. **a**, For 35L FGT, the region with WTe_2 shows narrower domain width. **b**, For 65L FGT, there is no difference of the magnetic domains. The region with dashed lines is for the FGT with WTe_2.

where J and H_{app} are the Heisenberg exchange coupling and applied magnetic field, respectively. The position-resolved DMI constant $\mathbf{D}_{i,j}(z)$ is given by:

$$\mathbf{D}_{i,j}(z) = (\mathbf{z} \times \mathbf{r}_{i,j})D(z). \tag{3.7}$$

Here DMI $D(z) = D_0 \exp(\frac{z-t}{l_0})$, and t, l_0 are the thickness of the film and a phenomenological penetration length, respectively. This DMI term is assumed to decay exponentially from the interface. The simulation results are shown in Fig. 3.32 based on a cubic lattice defined on a $25 \times 25 \times 20$ mesh. For simplicity, it is assumed that the side walls of the mesh have periodic boundaries. The top and bottom surfaces are open for mimicking the case of a thin film with $\mathbf{S}(r)$=0 for both $z > t$ and $z < 0$. The dynamical behaviors of the local spins $\mathbf{S}_i$ follow the Landau-Lifshitz-Gilbert

(LLG) equation[88]:

$$\dot{\mathbf{S}} = -\gamma \mathbf{S} \times \mathbf{H}_{\text{eff}} + \alpha \mathbf{S} \times \dot{\mathbf{S}}, \tag{3.8}$$

where $\gamma = \frac{g}{\hbar}$ and α are the gyromagnetic ration and damping factor, respectively. The effective field $\mathbf{H}_{\text{eff}}$ is given by $\mathbf{H}_{\text{eff}} = -\frac{\partial H}{\partial \mathbf{S}} + \mathbf{L}$, where H is the Hamiltonian given by Equation 3.6 and $\mathbf{L}$ is a random field provided by the thermal fluctuation at a finite temperature. The dissipation-fluctuation relation $\langle L_\mu(\mathbf{r}, t) L_v(\mathbf{r}', t') \rangle = \xi \delta_{\mu,v} \delta_{\mathbf{r},\mathbf{r}'} \delta_{tt'}$ is satisfied with $\xi = \frac{\alpha k_B T}{\gamma}$ determined by the damping factor and the explored temperature T[88]. The average $\langle \cdots \rangle$ is taken over the realizations of the fluctuation field. To mimic an adiabatic scan of the applied field in the experiment, the applied magnetic field sweeps as a triangle wave with the slopes much smaller than the characteristic time of the spins dynamics in the simulation. The parameters used in this simulation are $\frac{D_0}{J} = 1$, $k_B T = 0.1J$ and $l_0 = t \ln(\frac{D_0}{D_{\text{btm}}})$, with $D_{\text{btm}} = D(z)|_{z=0}$ phenomenologically chosen as $D_{\text{btm}} = 0.4 D_0$.

The simulation results in Fig. 3.32 show that for the FGT regions away from the interface, it enters the ferromagnetic phase in the vertical profile which is the yz plane. With a finite penetration of the DMI from the interface, the L-TEM is still can be used to capture the skyrmions at the interface since the FGT layers away from the interface enters into a uniform ferromagnetic phase, and contributes uniformly deflected electrons and thus no magnetic contrast.

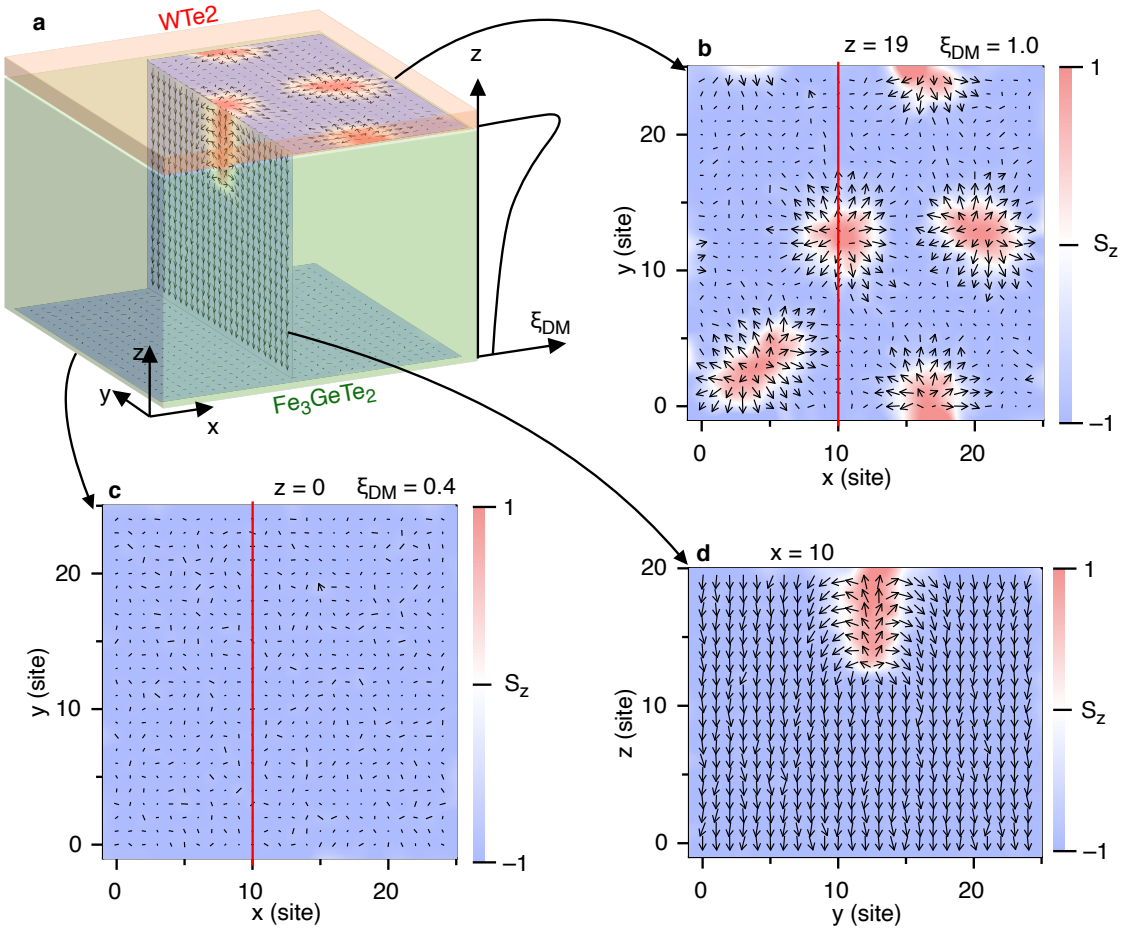


Figure 3.32. 3D view of the simulation of the skyrmions in WTe_2/FGT. **a**, DMI exists at the interface between the WTe_2 and FGT and decays when away from the interface. **b**, Spin polarization at the interface of WTe_2 and FGT. **c**, Spin polarizations for the side of FGT close to SiN substrate. **d**, Spin polarization at yz plane with a fixed x=10.

3.6 Comparison of skyrmion size between transport and Lorentz transmission electron microscopy measurements

In this discussion, transport measurements showed the THE in 1L WTe_2/4L FGT samples (Fig: 3.13), which is a signature for the presentce of skyrmions. However, there is no direction observation of the domain structure in heterostructures with L-TEM for FGT thickness less than 30L. To bridge the gap between THE and L-TEM results, THE was obtained for samples with FGT thickness from 3L to 5L and the skyrmion sizes ware estimated from the transport measurements.

Fig. 3.33 shows the THE for 1L WTe_2/3L FGT, 1L WTe_2/4L FGT and 2L WTe_2/5L FGT samples at 100 K. For samples with thicker FGTs, no THE signal obtained so far. A possible explanation is given as the fllowing. Assuming an exponential decay in the DMI profile, the simulation result suggests that the skyrmions are present near the WTe_2/FGT interface, with a large volume of the ferromagnetic phase away from the interface. When carriers pass through the ferromagnetic phase, they quickly lose the memory of the transport aquired from the THE because of the frequent scatterings, and the anomalous Hall effect becomes dominant. A quantitative analysis for the missing of THE in a thicker film can start by considering the carrier density. Due to the large carrier density in thicker FGT films, an extremely small topological Hall signal is expected. This analysis is done using the topological Hall resistivity $\rho_{xy}^{\text{THE}} = \frac{1}{ne}\frac{\Phi_0}{\frac{\sqrt{3}}{2}r^2}$, where r is the skyrmion size and is taken to be $\sim$100 nm, n is the carrier density, Φ_0 is the quantum flux and e is the electron charge. The topological Hall resistivity is estimated to be smaller than 0.01 Ω for the WTe_2/30L FGT samples. This topological Hall resistivity value is at least two orders of magnitude smaller than that of the anomalous Hall resistivity. This may help explain the missing THE humps in thicker films.

To estimate the skyrmion size from the topological Hall humps, the total Hall resistivity ρ_{xy} is decomposed into three parts: $\rho_{xy} = \rho_{xy}^{\text{N}} + \rho_{xy}^{\text{AHE}} + \rho_{xy}^{\text{THE}}$, where ρ_{xy}^{N} and ρ_{xy}^{AHE} are the normal Hall resistivity and anomalous Hall resistivity, respectively. With a linear ρ_{xy}^{N} as a background and a square loop of the anomalous Hall effect (ρ_{xy}^{AHE} equals the resistivity value at the saturation field $\rho_{xy}^{\text{AHE}} = \rho_{xy}^{\text{saturation}}$ without the linear background), $\rho_{xy}^{\text{THE}} + \rho_{xy}^{\text{N}} = \frac{1}{ne}(B_{\text{eff}} + B)$. The THE is attributed to an effective field B_{eff} as discussed before in Section 3.3. With a uniform hexagonal skyrmion lattice observed for our samples, it is reasonable to have $B_{\text{eff}} = \frac{\Phi_0}{\frac{\sqrt{3}}{2}r^2}$ since each flux quantum Φ_0 contributes to a magnetic skyrmion. With the Hall coefficient $\frac{1}{ne}$ obtained from the slope of

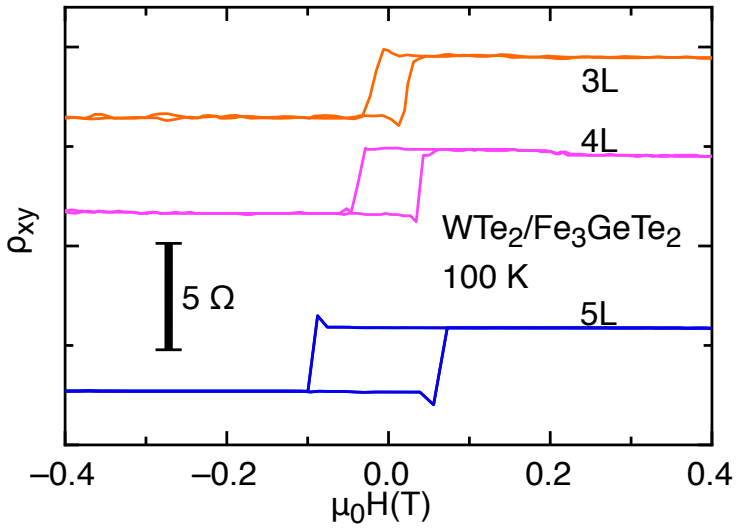


Figure 3.33. Topological Hall effect for 1L WTe_2/3L FGT, 1L WTe_2/4L FGT and 2L WTe_2/5L FGT samples. The dips and peaks near the magnetic phase transition have been observed for FGT thickness ranging from 3L to 5L.

ρ_{xy} after magnetic saturation, the skyrmion size is estimated as $r = \sqrt{\frac{\Phi_0}{\frac{\sqrt{3}}{2}\left[\left(\rho_{xy}-\rho_{xy}^{\text{saturated}}\right)ne-B\right]}}$. The skyrmion sizes estimated from the THE are shown in Fig. 3.34 for 1L WTe_2/3L FGT, 1L WTe_2/4L FGT and 2L WTe_2/5L FGT samples at 100 K with sizes within 100 nm as indicated by the magenta circles. For the skyrmion sizes obtained from the L-TEM, as shown with the magenta square and blue squares, they are in the order of 100 nm. Thus the skyrmion sizes from these two methods are a close match within the same order of magnitude.

In summary, the Néel-type skyrmion lattice from the L-TEM and the THE data from the transport measurement were compared for WTe_2/FGT heterostructures. A large interfacial DMI energy of $\sim$ 1.0 mJ/m^2 was extracted from the domain wall width, which might be a result of the broken inversion symmetry from the Rashba spin-orbit coupling. The skyrmion sizes are around 150 nm at 94 K and 80 nm at 198 K. Further studies may be carried out about the realization of 2D skyrmions at room temperature, which can be realized using electrical gating. This may open a new area in

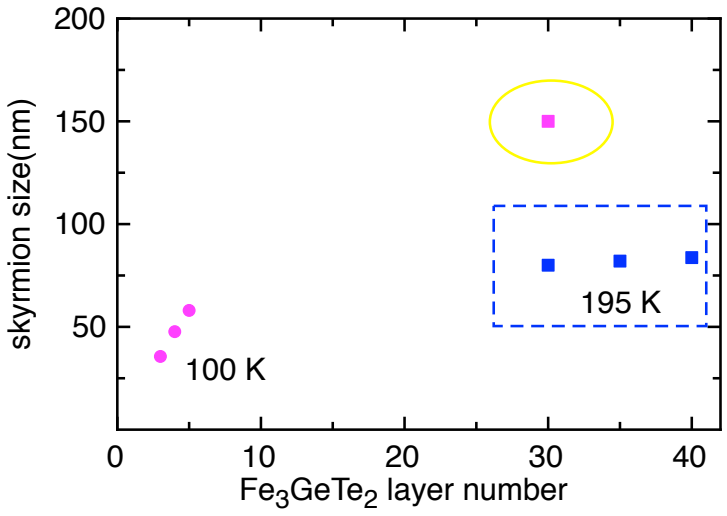


Figure 3.34. Extracted skyrmion size from transport and Lorentz transmission electron microscopy as a dependence on FGT thickness at 100 K and 195 K. The points in a circular shape are the skyrmion sizes from topological Hall effect and in a square shape are those from Lorentz transmission electron microscopy. Points in magenta color are taken at 100 K and points in blue color are taken at 195 K.

the field of ultra-compact next-generation spintronics.

Chapter 4

Summary and Outlook

4.1 Conclusion

In this dissertation, firstly, material assembly using the pick-up transfer stage is demonstrated. By using this technique, the interface coupling between the layered materials for different heterostructures can be formed and investigated. High spin and valley polarizations in 2D materials provide tantalizing opportunities for efficient spintronics and valleytronics. Various material systems with the proximity effect were used to spin- or valley-polarize 2D materials. We have shown a large exchange splitting in graphene proximitized by an antiferromagnet and an enhanced DMI in FGT from coupling to a few-layer transition metal dichalcogenides with large spin-orbit interaction.

Utilizing the high-quality monolayer graphene, we are able to realize the quantum Hall effect in the monolayer graphene. With a strong interfacial coupling between graphene and the antiferromagnet CrSe, the quantum oscillations and quantum Hall plateau can be shifted using the field coolings. This is a result of the strong exchange coupling between these two materials. The NiAs-type antiferromagnetic order in CrSe is supported by the X-ray diffraction and neutron diffraction data, which indicates a Néel temperature of $\sim$ 270 K for the film. This exchange splitting energy depends on the field cooling strength and directions, which is as large as 134 meV at zero

field coolings. The extraction of this large exchange splitting is from fitting the Landau level diagram using the machine learning. The fitting error is less than 2×10^{-5} with all the parameters converging to the same value. The proximity effect induced exchange splitting in graphene is also supported by the paramagnetism observed in graphene under magneto-optic Kerr effect measurement. This work makes graphene an ideal platform for both exploring the quantum interface physics and developing new graphene-based spintronic devices.

After the long-distance magnetic order has been discovered in 2D van der Waals materials recently, we came up an idea of manipulating the spin textures in FGT with an interfacial coupling through the large spin-orbit interaction. The layered material we have chosen with a large spin-orbit interaction is a few-layer WTe_2, which is terminated with the same Te atoms as those in the FGT. With monolayer or bilayer WTe_2 in the WTe_2/FGT heterostructure for the transport measurements, topological Hall effect is observed for WTe_2/a few-layer FGT heterostructures, which is a sign for topological magnetic skyrmions. To further prove the existence of the skyrmions, Lorentz transmission electron microscopy is adopted to obtain the magnetic domains. The domain width in the WTe_2/FGT heterostructure is much smaller than that in pristine FGT, indicating an enhanced DMI from the interfacial coupling. Using a phenomenological model, the domain wall energy can be estimated and thus a DMI as large as 1.0 mJ/m^2 is calculated, which is comparable to that in the heavy metal/ferromagnet case. The skyrmions and skyrmion lattice have also been captured in heterostructures with FGT thickness of no less than 30L. The skyrmion size is estimated to be $\sim$150 nm at 94 K and $\sim$80 nm at 197 K. The absence of topological Hall effect in heterostructure of a thick FGT and skyrmions under Lorentz transmission microscopy in the heterostructure with a thin FGT makes the two measurement results not directly related. To link these two results, we

extracted and estimated the skyrmion sizes from the topological Hall effect and they are on the same order of magnitude as those obtained with Lorentz transmission microscopy. Thus these two results are consistent. This study opens a new area in the field of ultra-compact next-generation spintronics.

4.2 Future work

Currently, the search for quantum anomalous Hall insulator among van der Waals magnetic materials attracts lots of attentions. Among all the materials, layered $Mn_1Bi_2Te_4$ is the first material found to be an intrinsic quantum anomalous Hall insulator and an axion insulator. In this material, the intralayer exchange coupling is ferromagnetic and the interlayer exchange coupling is antiferromagnetic. Thus monolayer and bulk $Mn_1Bi_2Te_4$ materials are a ferromagnet and 3D A-type antiferromagnet, respectively. Similar to $Mn_1Bi_2Te_4$, tetradymite-type ternary chalcogenides in a form of $M_1B_2T_4$, where M is transition-metal or rare-earth element, B is Bi or Sb atom and T is Te, Se, or S atom is all proposed to be possible magnetic topological quantum materials on the basis of first-principles density functional theory calculations[104]. These materials are promising for the search of high-temperature quantum anomalous Hall insulators.

Apart from these, the family of magnetic van der Waals heterostructures arises in the search of new structrues. With the interface between different materials, new physics and phenomena will emerge.

Material	ferromagnet or antiferromagnet	T_C or T_N (K)
$Mn_1Bi_4Te_7$	antiferromagnet ferromagnet	12[106] 13[105]
$Mn_1Bi_6Te_{10}$	antiferromagnet	11[107]
$Mn_1Bi_8Te_{13}$	ferromagnet	10.5[107]
LaCl	ferromagnet	22 [108]

Table 4.1. Possible van der Waals quantum anomalous Hall insulators, including $Mn_1Bi_{2+2n}Te_{4+3n}$ family and LaCl.

4.2.1 New intrinsic quantum anomalous Hall insulators

So far, $Mn_1Bi_2Te_4$ and $Mn_1Bi_4Te_7$[105] are reported experimentally to be intrinsic quantum anomalous Hall insulators. In our part, we are working on new potential magnetic topological quantum materials like $Mn_1Bi_{2+2n}Te_{4+3n}$, $Co_1Bi_{2+2n}Te_{4+3n}$ and $Cr_1Bi_{2+2n}Te_{4+3n}$ with n=0, 1, 2, 3, $\cdots$.

Tetradymite-type ternary chalcogenides in a form of $Mn_1Bi_{2+2n}Te_{4+3n}$ has a large family, including the recently discovered $Mn_1Bi_2Te_4$, $Mn_1Bi_4Te_7$, $Mn_1Bi_6Te_{10}$ and $Mn_1Bi_8Te_{13}$. With more layers of Bi_2Te_3 inserted between $Mn_1Bi_2Te_4$, the antiferromagnetic layer coupling becomes weaker and weaker. As a result, with three Bi_2Te_3 layers inserted, $Mn_1Bi_8Te_{13}$ turns into a ferromagnet[107]. However, there are some discrepancies in the literature. For example, $Mn_1Bi_4Te_7$ is reported to be an ferromagnet and an antiferromagnet by two different groups as indicated in the Table 4.1 due to their one different step of treatment during the growth. The only difference lies in whether the electron irradiation is adopted to tune the Fermi level after the sample growth at 20 K[105].

With bulk materials of $Mn_1Bi_4Te_7$ and $Mn_1Bi_8Te_{13}$, the electronic properties of them were investigated. As shown in Fig. 4.1, with one Bi_2Te_3 inserted between $Mn_1Bi_4Te_7$, it shows a

magnetic phase transition at $\sim$ 10 K. Some steps in Hall resistance are present when a magnetic field is applied.

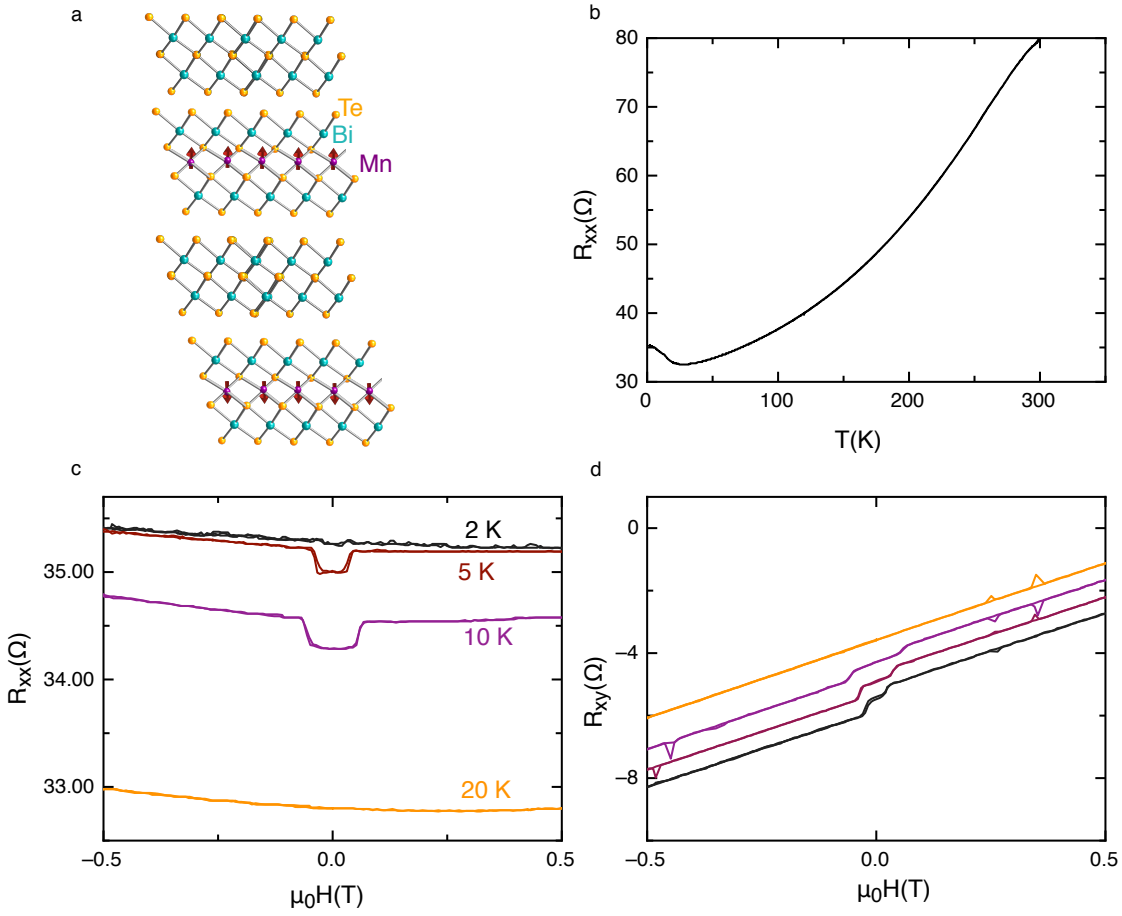


Figure 4.1. Transport properties of thick $Mn_1Bi_4Te_7$ close to bulk. **a**, Side view of crystal structure. **b**, Temperature dependence of longitudinal resistance indicating a magnetic phase transition around 10 K. Magnetoresistance **c** and Hall resistance **d** at temperatures of 2 K, 5 K, 10 K and 20 K.

For $Mn_1Bi_8Te_{13}$ with more Bi_2Te_3 layers inserted, it becomes a ferromagnet with a Curie temperature $\sim$ 10 K with Mn atoms layers coupled ferromagnetically. The hysteresis loop is very clear at temperatures of 2 K and 5 K as shown in Fig. 4.2.

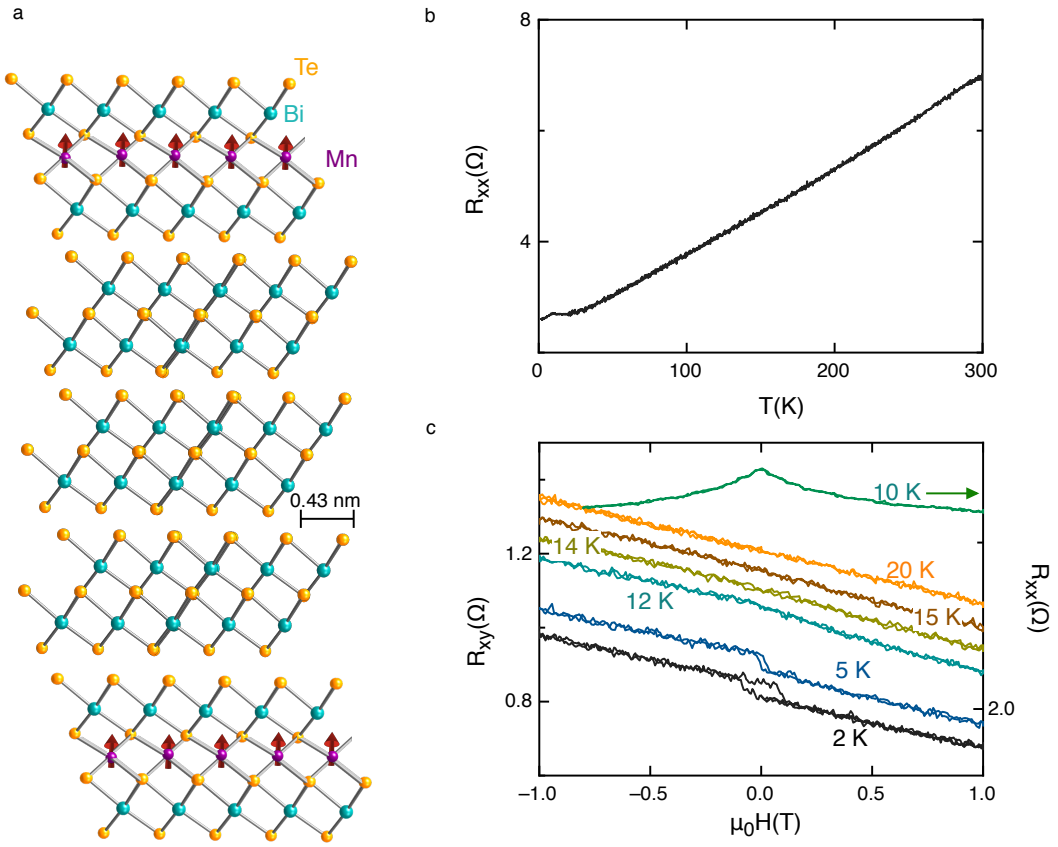


Figure 4.2. Transport properties of thick $Mn_1Bi_8Te_{13}$ close to bulk. **a**, Side view of crystal structure. **b**, Temperature dependence of longitudinal resistance indicating a magnetic phase transition around 10 K. **c**, Magnetoresistance at 10 K and Hall resistance at temperatures of 2 K, 5 K, 12 K 14 K, 15 K and 20 K.

4.2.2 Van der Waals heterostructure

Inserting different vdW materials into a heterostructure will provide much more opportunities and devices for future spintronic and electronic applications. Proximity effect between vdW materials with a magnetic material may turn the vdW material into a magnetic material[75] or quantum anomalous Hall insulator[109]; interface coupling between a magnetic vdW material and a vdW material may give rise to topological skyrmions[110]. New physics and phenomena have emerged in this field. Other than changing the materials in the heterostructure, the relative crystal orientation also plays a significant role in changing the band structrue of the heterostructures. For example,

angle orientation engineering between bilayer graphene gives rise to a superconductor[111] or a quantum anomalous Hall insulator[16].

More work on heterostructures like combining 2D magnetic materials and TMDs can be carried out with potential applications to new-generation ultra-compact devices.

REFERENCES

[1] Novoselov, K. S. *et al.* Room-temperature quantum Hall effect in graphene. *Science* **315**, 1379–1379 (2007).

[2] Neto, A. C., Guinea, F., Peres, N. M., Novoselov, K. S. & Geim, A. K. The electronic properties of graphene. *Reviews of Modern Physics* **81**, 109 (2009).

[3] Zhang, Y., Tan, Y.-W., Stormer, H. L. & Kim, P. Experimental observation of the quantum Hall effect and Berry's phase in graphene. *Nature* **438**, 201–204 (2005).

[4] Chen, X. *et al.* High-quality sandwiched black phosphorus heterostructure and its quantum oscillations. *Nature Communications* **6**, 1–6 (2015).

[5] Wu, Y. *et al.* Negative compressibility in graphene-terminated black phosphorus heterostructures. *Physical Review B* **93**, 035455 (2016).

[6] Yankowitz, M., Ma, Q., Jarillo-Herrero, P. & LeRoy, B. J. van der Waals heterostructures combining graphene and hexagonal boron nitride. *Nature Reviews Physics* **1**, 112–125 (2019).

[7] Manzeli, S., Ovchinnikov, D., Pasquier, D., Yazyev, O. V. & Kis, A. 2D transition metal dichalcogenides. *Nature Reviews Materials* **2**, 17033 (2017).

[8] Haldane, F. D. M. Model for a quantum Hall effect without Landau levels: Condensed-matter realization of the "parity anomaly". *Physical Review Letters* **61**, 2015 (1988).

[9] Sharpe, A. L. *et al.* Emergent ferromagnetism near three-quarters filling in twisted bilayer graphene. *Science* **365**, 605–608 (2019).

[10] Chen, G. *et al.* Tunable correlated Chern insulator and ferromagnetism in a moiré superlattice. *Nature* **579**, 56–61 (2020).

[11] Ugeda, M. M., Brihuega, I., Guinea, F. & Gómez-Rodríguez, J. M. Missing atom as a source of carbon magnetism. *Physical Review Letters* **104**, 096804 (2010).

[12] González-Herrero, H. *et al.* Atomic-scale control of graphene magnetism by using hydrogen atoms. *Science* **352**, 437–441 (2016).

[13] Červenka, J., Katsnelson, M. & Flipse, C. Room-temperature ferromagnetism in graphite driven by two-dimensional networks of point defects. *Nature Physics* **5**, 840–844 (2009).

[14] Nair, R. *et al.* Spin-half paramagnetism in graphene induced by point defects. *Nature Physics* **8**, 199–202 (2012).

[15] Sepioni, M. *et al.* Limits on intrinsic magnetism in graphene. *Physical Review Letters* **105**, 207205 (2010).

[16] Serlin, M. *et al.* Intrinsic quantized anomalous Hall effect in a moiré heterostructure. *Science* **367**, 900–903 (2020).

[17] Wang, Z., Tang, C., Sachs, R., Barlas, Y. & Shi, J. Proximity-induced ferromagnetism in graphene revealed by the anomalous Hall effect. *Physical Review Letters* **114**, 016603 (2015).

[18] Wei, P. *et al.* Strong interfacial exchange field in the graphene/EuS heterostructure. *Nature Materials* **15**, 711–716 (2016).

[19] Maryenko, D. *et al.* Observation of anomalous Hall effect in a non-magnetic two-dimensional electron system. *Nature Communications* **8**, 1–7 (2017).

[20] Soluyanov, A. A. *et al.* Type-II weyl semimetals. *Nature* **527**, 495–498 (2015).

[21] Li, P. *et al.* Evidence for topological type-II Weyl semimetal WTe_2. *Nature Communications* **8**, 1–8 (2017).

[22] Tang, S. *et al.* Quantum spin Hall state in monolayer 1T'-WTe_2. *Nature Physics* **13**, 683–687 (2017).

[23] Fatemi, V. *et al.* Electrically tunable low-density superconductivity in a monolayer topological insulator. *Science* **362**, 926–929 (2018).

[24] Kabashima, S. Electrical properties of tungsten-ditelluride WTe_2. *Journal of the Physical Society of Japan* **21**, 945–948 (1966).

[25] Augustin, J. *et al.* Electronic band structure of the layered compound Td- WTe_2. *Physical Review B* **62**, 10812 (2000).

[26] Haney, P. M. & Stiles, M. D. Current-induced torques in the presence of spin-orbit coupling. *Physical Review Letters* **105**, 126602 (2010).

[27] MacNeill, D. *et al.* Control of spin–orbit torques through crystal symmetry in WTe_2/ferromagnet bilayers. *Nature Physics* **13**, 300–305 (2017).

[28] Gong, C. *et al.* Discovery of intrinsic ferromagnetism in two-dimensional van der Waals crystals. *Nature* **546**, 265–269 (2017).

[29] Huang, B. *et al.* Layer-dependent ferromagnetism in a van der Waals crystal down to the monolayer limit. *Nature* **546**, 270–273 (2017).

[30] Bonilla, M. *et al.* Strong room-temperature ferromagnetism in VSe_2 monolayers on van der Waals substrates. *Nature Nanotechnology* **13**, 289–293 (2018).

[31] Deng, Y. *et al.* Quantum anomalous Hall effect in intrinsic magnetic topological insulator $MnBi_2Te_4$. *Science* **367**, 895–900 (2020).

[32] Liu, C. *et al.* Robust axion insulator and Chern insulator phases in a two-dimensional antiferromagnetic topological insulator. *Nature Materials* **19**, 522–527 (2020).

[33] Siberchicot, B., Jobic, S., Carteaux, V., Gressier, P. & Ouvrard, G. Band structure calculations of ferromagnetic chromium tellurides $CrSiTe_3$ and $CrGeTe_3$. *The Journal of Physical Chemistry* **100**, 5863–5867 (1996).

[34] Scagliotti, M., Jouanne, M., Balkanski, M., Ouvrard, G. & Benedek, G. Raman scattering in antiferromagnetic $FePS_3$ and $FePSe_3$ crystals. *Physical Review B* **35**, 7097 (1987).

[35] Scagliotti, M., Jouanne, M., Balkanski, M. & Ouvrard, G. Spin dependent phonon Raman scattering in antiferromagnetic $FePS_3$ layer-type compound. *Solid State Communications* **54**, 291–294 (1985).

[36] Lado, J. L. & Fernández-Rossier, J. On the origin of magnetic anisotropy in two dimensional CrI_3. *2D Materials* **4**, 035002 (2017).

[37] Saiz, C., McGuire, M. A., Hennadige, S., van Tol, J. & Singamaneni, S. R. Electron spin resonance properties of CrI_3 and $CrCl_3$ single crystals. *MRS Advances* **4** (2019).

[38] Deng, Y. *et al.* Gate-tunable room-temperature ferromagnetism in two-dimensional Fe_3GeTe_2. *Nature* **563**, 94–99 (2018).

[39] Mermin, N. D. & Wagner, H. Absence of ferromagnetism or antiferromagnetism in one-or two-dimensional isotropic Heisenberg models. *Physical Review Letters* **17**, 1133 (1966).

[40] Abrikosov, N. K., Bagaeva, L. & Dudkin, L. Phase equilibria in Fe-Ge-Te system. *Izv. Akad. Nauk SSSR, Neorg. Mater* **21**, 1680–1686 (1985).

[41] Nguyen, G. D. *et al.* Visualization and manipulation of magnetic domains in the quasi-two-dimensional material Fe_3GeTe_2. *Physical Review B* **97**, 014425 (2018).

[42] Fei, Z. *et al.* Two-dimensional itinerant ferromagnetism in atomically thin Fe_3GeTe_2. *Nature Materials* **17**, 778–782 (2018).

[43] Kim, K. *et al.* Large anomalous Hall current induced by topological nodal lines in a ferromagnetic van der Waals semimetal. *Nature Materials* **17**, 794–799 (2018).

[44] OHara, D. J. *et al.* Room temperature intrinsic ferromagnetism in epitaxial manganese selenide films in the monolayer limit. *Nano Letters* **18**, 3125–3131 (2018).

[45] Kargar, F. *et al.* Phonon and thermal properties of quasi-two-dimensional $FePS_3$ and $MnPS_3$ antiferromagnetic semiconductors. *ACS Nano* **14**, 2424–2435 (2020).

[46] Otrokov, M. M. *et al.* Prediction and observation of an antiferromagnetic topological insulator. *Nature* **576**, 416–422 (2019).

[47] Ge, J. *et al.* High-Chern-number and high-temperature quantum Hall effect without Landau levels. *National Science Review* **7**, 1280–1287 (2020).

[48] Peierls, R. On Ising's model of ferromagnetism. In *Mathematical Proceedings of the Cambridge Philosophical Society*, vol. 32, 477–481 (Cambridge University Press, 1936).

[49] Onsager, L. A two-dimensional model with an order-disorder transition (crystal statistics i). *Physical Review* **65**, 117–49 (1944).

[50] Berezinskii, V. Destruction of long-range order in one-dimensional and two-dimensional systems having a continuous symmetry group I. Classical systems. *Soviet Physics Journal of Experimental and Theoretical Physics* **32**, 493–500 (1971).

[51] Kosterlitz, J. M. & Thouless, D. J. Ordering, metastability and phase transitions in two-dimensional systems. *Journal of Physics C: Solid State Physics* **6**, 1181 (1973).

[52] Kerkmann, D., Wolf, J., Pescia, D., Woike, T. & Grünberg, P. Spin waves and two-dimensional magnetism in the Co-monolayer on Cu (100). *Solid State Communications* **72**, 963–966 (1989).

[53] de Jongh, L. J. *Magnetic properties of layered transition metal compounds*, vol. 9 (Springer Science & Business Media, 2012).

[54] Gibertini, M., Koperski, M., Morpurgo, A. & Novoselov, K. Magnetic 2D materials and heterostructures. *Nature Nanotechnology* **14**, 408–419 (2019).

[55] Thiel, L. *et al.* Probing magnetism in 2D materials at the nanoscale with single-spin microscopy. *Science* **364**, 973–976 (2019).

[56] Li, Q. *et al.* Patterning-induced ferromagnetism of Fe_3GeTe_2 van der Waals materials beyond room temperature. *Nano Letters* **18**, 5974–5980 (2018).

[57] Sun, Y.-J., Tan, Q.-H., Liu, X.-L., Gao, Y.-F. & Zhang, J. Probing the magnetic ordering of antiferromagnetic $MnPS_3$ by Raman spectroscopy. *The Journal of Physical Chemistry Letters* **10**, 3087–3093 (2019).

[58] Seyler, K. L. *et al.* Ligand-field helical luminescence in a 2D ferromagnetic insulator. *Nature Physics* **14**, 277–281 (2018).

[59] Huang, B. *et al.* Electrical control of 2D magnetism in bilayer CrI_3. *Nature Nanotechnology* **13**, 544–548 (2018).

[60] Xing, W. *et al.* Magnon transport in quasi-two-dimensional van der Waals antiferromagnets. *Physical Review X* **9**, 011026 (2019).

[61] Gong, C. & Zhang, X. Two-dimensional magnetic crystals and emergent heterostructure devices. *Science* **363** (2019).

[62] Zhong, D. *et al.* Van der Waals engineering of ferromagnetic semiconductor heterostructures for spin and valleytronics. *Science advances* **3**, e1603113 (2017).

[63] Wang, X. *et al.* Current-driven magnetization switching in a van der Waals ferromagnet Fe_3GeTe_2. *Science Advances* **5**, eaaw8904 (2019).

[64] Dietl, T. A ten-year perspective on dilute magnetic semiconductors and oxides. *Nature Materials* **9**, 965–974 (2010).

[65] Corliss, L., Elliott, N., Hastings, J. & Sass, R. Magnetic structure of chromium selenide. *Physical Review* **122**, 1402 (1961).

[66] Katsuyama, S., Ueda, Y. & Kosuge, K. Phase diagram and order-disorder transition of vacancies in the $Cr_{1b}Se$ and $Fe_{1b}Se$ systems. *Materials Research Bulletin* **25**, 913–922 (1990).

[67] Yan, J. *et al.* Anomalous Hall effect in two-dimensional non-collinear antiferromagnetic semiconductor $Cr_{0.68}Se$. *Applied Physics Letters* **111**, 022401 (2017).

[68] Hayashi, A. *et al.* Cation distribution in (M', $M)_3Se_4$: II.(V, $Ti)_3Se_4$ and (Cr, $V)_3Se_4$. *Journal of Solid State Chemistry* **71**, 237–243 (1987).

[69] Polesya, S., Mankovsky, S., Benea, D., Ebert, H. & Bensch, W. Finite-temperature magnetism of CrTe and CrSe. *Journal of Physics: Condensed Matter* **22**, 156002 (2010).

[70] Zhu, W., Seve, L., Sears, R., Sinkovic, B. & Parkin, S. Field cooling induced changes in the antiferromagnetic structure of NiO films. *Physical Review Letters* **86**, 5389 (2001).

[71] Ambrose, T. & Chien, C. Dependence of exchange field and coercivity on cooling field in NiFe/CoO bilayers. *Journal of Applied Physics* **83**, 7222–7224 (1998).

[72] Koon, N. Calculations of exchange bias in thin films with ferromagnetic/antiferromagnetic interfaces. *Physical Review Letters* **78**, 4865 (1997).

[73] Hoffmann, A. Symmetry driven irreversibilities at ferromagnetic-antiferromagnetic interfaces. *Physical Review Letters* **93**, 097203 (2004).

[74] Kriegner, D. *et al.* Multiple-stable anisotropic magnetoresistance memory in antiferromagnetic MnTe. *Nature Communications* **7**, 1–7 (2016).

[75] Wu, Y. *et al.* Large exchange splitting in monolayer graphene magnetized by an antiferromagnet. *Nature Electronics* 1–8 (2020).

[76] Gusynin, V. & Sharapov, S. Unconventional integer quantum Hall effect in graphene. *Physical Review Letters* **95**, 146801 (2005).

[77] Polak, E. & Ribiere, G. Note sur la convergence de méthodes de directions conjuguées. *ESAIM: Mathematical Modelling and Numerical Analysis-Modélisation Mathématique et Analyse Numérique* **3**, 35–43 (1969).

[78] Kiefer, J. Sequential minimax search for a maximum. *Proceedings of the American Mathematical Society* **4**, 502–506 (1953).

[79] Tan, Y.-W. *et al.* Measurement of scattering rate and minimum conductivity in graphene. *Physical Review Letters* **99**, 246803 (2007).

[80] Zhang, J. *et al.* Strong magnetization and Chern insulators in compressed graphene/CrI_3 van der Waals heterostructures. *Physical Review B* **97**, 085401 (2018).

[81] Wang, Z. *et al.* Origin and magnitude of 'designer' spin-orbit interaction in graphene on semiconducting transition metal dichalcogenides. *Physical Review X* **6**, 041020 (2016).

[82] McCann, E. & Fal'ko, V. I. z $\rightarrow$ -z symmetry of spin-orbit coupling and weak localization in graphene. *Physical Review Letters* **108**, 166606 (2012).

[83] Klein, D. R. *et al.* Probing magnetism in 2D van der Waals crystalline insulators via electron tunneling. *Science* **360**, 1218–1222 (2018).

[84] Song, T. *et al.* Giant tunneling magnetoresistance in spin-filter van der Waals heterostructures. *Science* **360**, 1214–1218 (2018).

[85] Huang, B. *et al.* Tuning inelastic light scattering via symmetry control in the two-dimensional magnet cri 3. *Nature Nanotechnology* **15**, 212–216 (2020).

[86] May, A. F., Calder, S., Cantoni, C., Cao, H. & McGuire, M. A. Magnetic structure and phase stability of the van der Waals bonded ferromagnet $Fe_{3-x}GeTe_2$. *Physical Review B* **93**, 014411 (2016).

[87] Ye, F. *et al.* Environmental instability and degradation of single-and few-layer WTe_2 nanosheets in ambient conditions. *Small* **12**, 5802–5808 (2016).

[88] Nagaosa, N. & Tokura, Y. Topological properties and dynamics of magnetic skyrmions. *Nature nanotechnology* **8**, 899–911 (2013).

[89] Fert, A., Reyren, N. & Cros, V. Magnetic skyrmions: advances in physics and potential applications. *Nature Reviews Materials* **2**, 1–15 (2017).

[90] Matsuno, J. *et al.* Interface-driven topological Hall effect in $SrRuO_3$-$SrIrO_3$ bilayer. *Science Advances* **2**, e1600304 (2016).

[91] Neubauer, A. *et al.* Topological Hall effect in the A phase of MnSi. *Physical Review Letters* **102**, 186602 (2009).

[92] Yasuda, K. *et al.* Geometric Hall effects in topological insulator heterostructures. *Nature Physics* **12**, 555–559 (2016).

[93] Kanazawa, N. *et al.* Discretized topological Hall effect emerging from skyrmions in constricted geometry. *Physical Review B* **91**, 041122 (2015).

[94] Beleggia, M., Schofield, M., Volkov, V. & Zhu, Y. On the transport of intensity technique for phase retrieval. *Ultramicroscopy* **102**, 37–49 (2004).

[95] Peng, L.-C. *et al.* Lorentz transmission electron microscopy studies on topological magnetic domains. *Chinese Physics B* **27**, 066802 (2018).

[96] Bodenberger, R. & Hubert, A. Zur bestimmung der blochwandenergie von einachsigen ferromagneten. *Physica Status Solidi (a)* **44**, K7–K11 (1977).

[97] Gao, Y., Zhu, J., Weng, Y. & Han, B. Domain structure in Fe-implanted $Nd_2Fe_{14}B$ magnets. *Applied Physics Letters* **74**, 1749–1751 (1999).

[98] Szmaja, W., Grobelny, J., Cichomski, M., Hirosawa, S. & Shigemoto, Y. Magnetic force microscopy investigation of the domain structure of nanocomposite $Nd_2Fe_{14}B/Fe_3B$ magnets. *Acta Materialia* **59**, 531–536 (2011).

[99] León-Brito, N., Bauer, E. D., Ronning, F., Thompson, J. D. & Movshovich, R. Magnetic microstructure and magnetic properties of uniaxial itinerant ferromagnet Fe_3GeTe_2. *Journal of Applied Physics* **120**, 083903 (2016).

[100] Kim, D. *et al.* Antiferromagnetic coupling of van der Waals ferromagnetic Fe_3GeTe_2. *Nanotechnology* **30**, 245701 (2019).

[101] Stoner, E. C. & Wohlfarth, E. A mechanism of magnetic hysteresis in heterogeneous alloys. *Philosophical Transactions of the Royal Society of London. Series A, Mathematical and Physical Sciences* **240**, 599–642 (1948).

[102] Woo, S. *et al.* Observation of room-temperature magnetic skyrmions and their current-driven dynamics in ultrathin metallic ferromagnets. *Nature Materials* **15**, 501–506 (2016).

[103] Thiaville, A., Rohart, S., Jué, É., Cros, V. & Fert, A. Dynamics of Dzyaloshinskii domain walls in ultrathin magnetic films. *Europhysics Letters* **100**, 57002 (2012).

[104] Li, J. *et al.* Intrinsic magnetic topological insulators in van der Waals layered $MnBi_2Te_4$-family materials. *Science Advances* **5**, eaaw5685 (2019).

[105] Deng, H. *et al.* Observation of high-temperature quantum anomalous Hall regime in intrinsic $MnBi_2Te_4/Bi_2Te_3$ superlattice. *Nature Physics* **10**, 1038 (2020).

[106] Hu, C. *et al.* A van der Waals antiferromagnetic topological insulator with weak interlayer magnetic coupling. *Nature Communications* **11**, 1–8 (2020).

[107] Hu, C. *et al.* Realization of an intrinsic ferromagnetic topological state in $MnBi_8Te_{13}$. *Science Advances* **6**, eaba4275 (2020).

[108] Liu, Z. *et al.* Intrinsic quantum anomalous Hall effect with in-plane magnetization: searching rule and material prediction. *Physical Review Letters* **121**, 246401 (2018).

[109] Qiao, Z. *et al.* Quantum anomalous Hall effect in graphene proximity coupled to an antiferromagnetic insulator. *Physical Review Letters* **112**, 116404 (2014).

[110] Wu, Y. *et al.* Néel-type skyrmion in WTe_2/Fe_3GeTe_2 van der Waals heterostructure. *Nature Communications* **11**, 1–6 (2020).

[111] Yankowitz, M. *et al.* Tuning superconductivity in twisted bilayer graphene. *Science* **363**, 1059–1064 (2019).